Ocean Modelling 145 (2020) 101503

Contents lists available at ScienceDirect

Ocean Modelling

journal homepage: www.elsevier.com/locate/ocemod

Virtual Special Issue - CORE-II

# An assessment of the Indian Ocean mean state and seasonal cycle in a suite of interannual CORE-II simulations

H. Rahaman [a,*], U. Srinivasu [a], S. Panickal [b], J.V. Durgadoo [c], S.M. Griffies [d], M. Ravichandran [e], A. Bozec [f], A. Cherchi [g,q], A. Voldoire [h], D . Sidorenko [i], E.P. Chassignet [f], G. Danabasoglu [j], H. Tsujino [k], K. Getzlaff [c], M. Ilicak [l], M. Bentsen [m], M.C. Long [j], P.G. Fogli [g], R. Farneti [n], S. Danilov [i], S.J. Marsland [o], S. Valcke [p], S.G. Yeager [j], Q. Wang [i]

[a] Indian National Centre for Ocean Information Services (INCOIS), Hyderabad, India
[b] Centre for Climate Change Research, Indian Institute of Tropical Meteorology (IITM), Pune, India
[c] GEOMAR Helmholtz Centre for Ocean Research Kiel, Kiel, Germany
[d] NOAA Geophysical Fluid Dynamics Laboratory(GFDL) and Princeton University Atmospheric and Oceanic Sciences Program, Princeton, USA
[e] National Centre for Polar and Ocean Research (NCPOR) Goa, India
[f] Center for Ocean-Atmospheric Prediction Studies (COAPS), Florida State University, Tallahassee, FL, USA
[g] Fondazione Centro Euro-Mediterraneo sui Cambiamenti Climatici, Bologna, Italy
[h] Centre National de Recherches Météorologiques (CNRM-GAME), Toulouse, France
[i] Alfred Wegener Institute (AWI) Helmholtz Centre for Polar and Marine Research, Bremerhaven, Germany
[j] National Center for Atmospheric Research, Boulder, USA
[k] Meteorological Research Institute (MRI), Japan Meteorological Agency, Tsukuba, Japan
[l] Eurasia Institute of Earth Sciences, Istanbul Technical University, Istanbul, Turkey
[m] NORCE Norwegian Research Centre, Bjerknes Centre for Climate Research, Bergen, Norway
[n] International Centre for Theoretical Physics (ICTP), Trieste, Italy
[o] CSIRO Climate Science Centre, Aspendale, Australia
[p] Centre Européen de Recherche et de Formation Avancéen Calcul Scientifique (CERFACS), URA 1875, CNRS/INSU, Toulouse, France
[q] Istituto Nazionale di Geofisica e Vulcanologia, Bologna, Italy

## ABSTRACT

We present an analysis of annual and seasonal mean characteristics of the Indian Ocean circulation and water masses from 16 global ocean–sea-ice model simulations that follow the Coordinated Ocean-ice Reference Experiments (CORE) interannual protocol (CORE-II). All simulations show a similar large-scale tropical current system, but with differences in the Equatorial Undercurrent. Most CORE-II models simulate the structure of the Cross Equatorial Cell (CEC) in the Indian Ocean. We uncover a previously unidentified secondary pathway of northward cross-equatorial transport along 75 °E, thus complementing the pathway near the Somali Coast. This secondary pathway is most prominent in the models which represent topography realistically, thus suggesting a need for realistic bathymetry in climate models. When probing the water mass structure in the upper ocean, we find that the salinity profiles are closer to observations in geopotential (level) models than in isopycnal models. More generally, we find that biases are model dependent, thus suggesting a grouping into model lineage, formulation of the surface boundary, vertical coordinate and surface salinity restoring. Refinement in model horizontal resolution (one degree versus $\frac{1}{4}$ degree) does not significantly improve simulations, though there are some marginal improvements in the salinity and barrier layer results. The results in turn suggest that a focus on improving physical parameterizations (e.g. boundary layer processes) may offer more near-term advances in Indian Ocean simulations than refined grid resolution.

## 1. Introduction

The tropical Indian Ocean covers the largest part of the warm pool in the global ocean apart from the west Pacific. It is a key ingredient in the Asian monsoons, which are a lifeline for billions of people in the rim countries (Webster et al., 1998). The Indian Ocean has unique features compared to the Pacific and Atlantic Oceans. Most notably, it is bounded to the north by the Asian continent, thus preventing the northward export of heat into the extratropical region (between 30 and 60°N). This geographical constraint leads to a basin-wide meridional overturning circulation (MOC) (a full list of abbreviations is presented in the Appendix) and a corresponding transport of heat and mass that play a distinctive role in variability of the global climate system (Chirokova and Webster, 2006). Schott and McCreary (2001) and then Schott et al. (2009) provided systematic reviews of Indian Ocean circulation. In particular, Schott et al. (2009) noted that much of the literature pertaining to simulations of the Indian Ocean is focused

* Corresponding author.
*E-mail addresses:* rahman@incois.gov.in, nhrahman@gmail.com (H. Rahaman).

https://doi.org/10.1016/j.ocemod.2019.101503
Received 2 April 2019; Received in revised form 11 October 2019; Accepted 14 October 2019
Available online 21 October 2019

on specific aspects rather than unifying across the range of features. They also pointed out that one hindrance to progress is that existing models are deficient in a number of ways, such as the existence of spurious convective overturning, enhanced numerical mixing, and unrealistic horizontal diffusion. If subsurface mixing is not adequately parameterized, the simulated thermocline becomes too diffuse. This error affects the temperature of the water that upwells and hence the sea surface temperature (SST).

During recent years, increases in observational data have been available under the Indian Ocean observing system IndOOS program (http://www.clivar.org/clivar-panels/indian/IndOOS). This is a sustained observing system operated and supported by various national agencies and coordinated internationally through the Climate Variability and Predictability (CLIVAR)/Intergovernmental Oceanographic Commission (IOC)-Global Ocean Observing System (GOOS) Indian Ocean Regional Panel. Unlike for the observations, a comprehensive analysis of the basin-scale oceanographic features from a suite of ocean models for the Indian Ocean has not been documented. The historical simulations using a suite of 16 global ocean-ice models forced by the Coordinated Ocean Reference Experiments (CORE-II) provide an opportunity to study the dynamics of Indian Ocean under a coordinated modeling framework. This manuscript endeavors to describe and evaluate the mean state and seasonal variations of important oceanographic features such as the SST, Sea Surface Salinity (SSS), currents, thermocline and barrier layer (BL). We do so with a suite of 16 state-of-the-art global ocean/sea-ice model simulations with bulk formula based boundary forcing generated from the same atmospheric state. There are examples of a number of successful inter-comparison activities for the Pacific, Atlantic, Arctic, and Southern Oceans (Tseng et al., 2017; Danabasoglu et al., 2014, 2016; Farneti et al., 2015; Ilicak et al., 2016). However, such coordinated modeling efforts have generally been lacking for the Indian Ocean. We therefore aim here at assessing the simulations from forced global ocean models for the Indian Ocean.

SST is one of the most important parameters for the evolution and prediction of the Indian Summer Monsoon Rainfall (ISMR) as it represents the integrated ocean response to the atmosphere in terms of various feedbacks (Sahai et al., 2007; Rajeevan et al., 2007, 2012; Yang et al., 2007). Accurate simulations of Indian Ocean SST are challenging given the wide variety of intraseasonal, seasonal and interannual variability (Schott and McCreary, 2001; Schott et al., 2009). In addition to variability intrinsic to the Indian Ocean, there are impacts from *El Niño* Southern Oscillation (ENSO) that connect from the Pacific Ocean (Annamalai et al., 2005). In the North Indian Ocean (NIO hereafter), ENSO affects SST variability through an atmospheric bridge that changes cloud cover and thus modifies surface heat fluxes (e.g., Klein et al., 1999; Murtugudde and Busalacchi, 1999). Over the southwestern Indian Ocean, ENSO forced SST variability arises from oceanic Rossby waves generated by anomalous easterly winds that propagate from the east (e.g. Xie et al., 2002; Huang and Kinter III, 2002). Errors in simulated Indian Ocean SST adversely affect the ability of coupled prediction models to accurately forecast ISMR (Chowdary et al., 2015, 2016; Chaudhari et al., 2013; Levine and Turner, 2012). The CORE-II simulations do not use explicit relaxation to observed SST. However, since air temperature is specified as part of the CORE-II atmospheric state, there is an effective restoring flux (Haney, 1971; Murtugudde and Busalacchi, 1999; Griffies et al., 2009). Hence, the CORE-II simulations are more constrained than coupled climate models. Our analysis of CORE-II SST biases thus offers a means to determine that portion of the coupled climate model errors that can be attributed to ocean components.

SSS and subsurface salinities strongly affect the surface buoyancy and hence the surface and subsurface water mass structures (Weller and Anderson, 1996; Murtugudde et al., 1998). Salinity can thus have a strong influence on the thermodynamic structure of the mixed layer, thermocline and their interactions (Mignot et al., 2007). Apart from rainfall, salinity distributions in the Indian Ocean are driven by river inflows, especially in the Bay of Bengal (BoB) which receives nearly as much riverine input as rainfall (e.g., Shetye et al., 1996; Howden and Murtugudde, 2001; Vinayachandran et al., 2002; Sengupta et al., 2006). The influx of freshwater (FW) through the Indonesian through flow (ITF), and the influx of saltier water from the Persian Gulf and Red Sea also imprint clear signatures on the dynamics and thermodynamics of the Indian Ocean (Murtugudde et al., 1998; Gordon et al., 2010; Gordon and Fine, 1996; McCreary et al., 2001, 1993; Bray et al., 1997). Many Indian Ocean modeling studies use regional configurations with closed (sponge) boundaries at the east and south (Kurian and Vinayachandran, 2007; Han et al., 2001; Han and McCreary, 2001), often leading to unrealistic salinity properties. Similarly, better representation of BoB freshwater influx is essential for studying the salinity distribution (Sitz et al., 2017). The near surface salinity distribution study by Zhang and Marotzke (1999) using a model configured with open boundaries showed an unrealistic local minimum of salinity in the north-western BoB due to the lack of inclusion of runoff from Ganges and Brahmaputra. The freshwater forcing affects mixed layer depths and surface currents which can advect the freshwater input away from the rivers (Howden and Murtugudde, 2001; Sengupta et al., 2006; Han et al., 2001). Rahaman et al. (2014) showed an improvement in SSS simulations with a nested regional model with salinity bias less than 1 psu in the northern BoB. However, coupled models still show large biases (~1.5 psu) over the BoB as well as the NIO (Vinayachandran and Nanjundiah, 2009; Fathrio et al., 2017b). In general, the subsurface salinity bias in models is not documented for the Indian Ocean from a suite of global model simulations. In this study apart from surface salinity we also evaluated the subsurface salinity from the suite of 16 model simulations.

The Indian Ocean circulation is dominated by the dramatic seasonally reversing monsoon winds (e.g. Webster et al., 1998). The low-latitude landmass of the Indian subcontinent drives the strong monsoon, thus causing ocean currents and winds to seasonally reverse in the NIO (Gadgil et al., 2005; Gadgil, 2003; Schott et al., 2009). Seasonally reversing monsoon winds (southwesterly during summer and northeasterly during winter) give rise to seasonally reversing current systems in the NIO. The semi-annual cycle in the Indian Ocean is also related to the seasonally reversing monsoonal winds. Fig. 1a provides a schematic of the horizontal circulation patterns in the Indian Ocean, including the circulations forced by the Asian monsoon. The major NIO current systems exhibiting a reversal in direction with the monsoons (see Fig. 1a) include the Somali current (SC), Southwest and Northeast Monsoon Currents (SMC and NMC), West India Coastal current (WICC), and East India Coastal current (EICC). Though the Indian Ocean does not possess an equatorial upwelling system similar to the Pacific or Atlantic, major upwelling regions do occur off the coast of Somalia and Sumatra in the north and southeastern equatorial Indian Ocean, respectively (green shaded portions of Fig. 1a). Another unique feature is the open ocean upwelling dome or Seychelles Dome in the southwest of the Indian Ocean. Satellite color images clearly reveal the existence of an open ocean upwelling zone between 5°S to 12°S over the southwest Indian Ocean (Xie et al., 2002). The north and south current systems are separated around 10–12°S by a nearly zonal annually prevailing South Equatorial Current (SEC). The zonal structure of the SEC is maintained by the zero-wind stress curl around 10°S, which is a consequence of the annually prevailing southeasterly winds to the south of 10°S and the seasonally reversing monsoon winds to the north. This SEC plays a fundamental role in transporting warm and fresh western Pacific waters westward across the Indian Ocean through ITF. The SEC after reaching the northern tip of Madagascar bifurcates into the Northeast and Southeast Madagascar Current (SEMC and NEMC) (e.g. Chen et al., 2014; Yamagami and Tozuka, 2015). The SEMC feeds into the Agulhas Current (AC), which is part of the anticyclonic subtropical gyre similar to those in other ocean basins. However, unlike other basins, this western boundary current overshoots

the southern extent of the African continent, with a portion extending westward into the South Atlantic Ocean (a.k.a. Agulhas leakage), and a portion retroflecting and flowing eastward along the equatorward edge of the Antarctic Circumpolar Current (Lutjeharms, 2006). The Leeuwin Current (Waite et al., 2007) is an eastern boundary current along the west coast of Australia. Interestingly, its southward flow is counter to what is expected from the predominant winds. Along the eastern boundary at low latitudes, the Indian Ocean receives additional heat and mass from the Pacific Ocean through the ITF (Godfrey, 1996; Gordon and Fine, 1996; Murtugudde et al., 1998). The ITF allows the water from the Pacific Ocean to reach the Indian Ocean. These waters are then transported westward across the Indian Ocean by the westward-flowing SEC. In the southern tip of Madagascar, the SEMC breaks into a series of dipole eddies that propagate downstream into the Agulhas Current system and enters the Atlantic Ocean south of South Africa (Han et al., 2014; Durgadoo et al., 2017; Nauw et al., 2008; Palastanga et al., 2006; Ponsoni et al., 2016; Ridderinkhof et al., 2013). Some part of this water then retroflects eastward back into the Southern Indian Ocean (SIO) to feed the South Indian Ocean Counter Current (SICC) (Palastanga et al., 2007; Siedler et al., 2009). In this study, we show how the CORE-II models are able to simulate these circulation features with respect to observations.

In addition to the annual monsoonal cycle, the circulation varies semiannually along the equator with a strong surface eastward current named Wyrtki jet (WJ; Wyrtki, 1973). WJ appears as a narrow band trapped within 2° –3° of the equator during the two transition periods of monsoons (April–May and October– November) driven by the equatorial westerly winds. This WJ plays an important role in the large-scale heat and freshwater transports in the tropical Indian Ocean (Wyrtki, 1973; Reverdin, 1985; Schott and McCreary, 2001; Schott et al., 2009). The subsurface currents also show seasonal variations in the equatorial Indian Ocean. Observations show the presence of subsurface Equatorial Under Current (EUC), which is reported in various studies (e.g., Knox, 1976, 1981; Reppin et al., 1999; Schott and McCreary, 2001; Iskandar et al., 2009). In the Pacific and Atlantic Oceans, the EUC is a quasi-permanent feature because of the prevailing easterly trade winds (Philander, 1973; Philander and Pacanowski, 1980; McPhaden, 1986; Seidel and Giese, 1999). In the equatorial Indian Ocean, however, it is transient and depends on winds and pressure gradient variations associated with the distinct seasonal cycle due to the Asian monsoon. It is most pronounced in Northern Hemisphere winter (Iskandar et al., 2009), with its presence and absence mainly determined by the weaker and stronger easterlies in late winter and early spring (Cane, 1980; Reppin et al., 1999). The EUC is also present during the southwest monsoon (Reppin et al., 1999). It is associated with equatorial waves driven by the strong seasonally varying surface winds (Schott and McCreary, 2001). The core of this eastward undercurrent is located in the thermocline region above 300 m, beneath which a weak westward counter-flow exists and can last for at least a month during winter and spring. Observations show that the magnitude of the eastward undercurrent can exceed 1.2 m/s during March–June and is comparable to the Pacific Ocean undercurrent magnitude (Swallow, 1964, 1967). Previous studies show that forced model simulations are able to capture the undercurrent reasonably well (Iskandar et al., 2009; Chen et al., 2015). A comprehensive evaluation of how WJ and EUC are represented in global models is still lacking. In this study, we also assessed in detail about how the CORE-II models perform in simulating them.

Apart from the surface circulations and equatorial currents discussed in the previous paragraphs, two cells are active in the Indian Ocean: the cross-equatorial cell (CEC) and the southern subtropical cell (SSTC) (Lee, 2004; Schott et al., 2004). The CEC is a shallow (~500 m) meridional overturning circulation, consisting of the northward flow of southern-hemisphere thermocline water, upwelling in the northern hemisphere, and a return flow of surface water (Miyama et al., 2003). A schematic of the meridional circulation of the Indian Ocean in the upper ocean (0–500 m) is given in Fig. 1b (from Lee, 2004). The upper Indian Ocean heat balance is achieved by CEC and SSTC (Miyama et al., 2003; Schott et al., 2004). The CEC connects upwelling zones in the NIO to subduction zones in the southeastern Indian Ocean via a southward, cross-equatorial branch concentrated in the upper 50 m and a northward bulk-flow of cooler thermocline water. Miyama et al. (2003) have shown that the sources of water for the subsurface branch of the cross equatorial cell are the subduction zones in the southeastern Indian Ocean, the ITF, and flow into the basin across the southern boundary. This subduction seems to occur predominantly in the southern subtropical Indian Ocean as shown in Fig. 1a (blue shading). A small subduction site also exists in the AS. However, the exact location of this northward thermocline flow is not yet known. Both poor sampling of deeper layers and relatively coarse resolution models used to study the dynamics of Indian Ocean have contributed to poor understanding of the subsurface thermocline northward flow in the Indian Ocean. The suite of global ocean circulation models including relatively fine resolution models that participated in the CORE-II simulations (Danabasoglu et al., 2014) used in this paper made it possible to document simulated pathways of the thermocline water into the NIO. The CEC variability accounts for a significant portion of Indian Ocean cross-equatorial heat transport, which is hypothesized to be associated with the Asian monsoon (Chirokova and Webster, 2006; Swapna et al., 2017).

The Indian Ocean circulation is mainly driven by the seasonal reversal of the monsoon wind. Thus, the mean and variability of wind forcing has a large impact on Indian Ocean simulations (Parekh et al., 2011). More generally, the heat, water, and momentum balances are affected by uncertainties in turbulent and radiative heat fluxes. These uncertainties in the forcing fields can have a major role in the fidelity of OGCM simulations on intra-seasonal, seasonal, inter-annual and longer time-scales (McWilliams, 1996). Hence, accurate near-surface atmospheric fields are essential for realistic simulations in a forced ocean model. Here, we offer a brief overview of how the CORE-II atmospheric state compares to observational based measures. However, a full assessment of these impacts requires comparisons to simulations run with other atmospheric products such as Japanese 55-year atmospheric reanalysis (JRA-55) based surface dataset for driving ocean–sea-ice models (JRA55-do: Tsujino et al., 2018) and DRAKKAR (Brodeau et al., 2010) forcing. The analysis presented in this paper provides a necessary starting point for that assessment.

Our study is motivated by the important role of the Indian Ocean in regional and global climate variability, especially in the tropics. This role in turn prompts the need for improved understanding of Indian Ocean circulation dynamics, including its mean state and variability, in support of improved simulations of regional and global climate (e.g., Swapna et al., 2014). We are motivated to perform systematic assessments of Indian Ocean features found in global climate model simulations. Increased awareness of the role of the Indian Ocean for regional and global climate, including its importance for the billions of humans living along its coasts and nearby regions, prompts the need to systematically articulate the problems and prospects with global model simulations for this region.

The paper is organized as follows. Section 2 describes the CORE-II simulations and the main goal of the study. Section 3 describes models and observational datasets. Section 4 contains main results and discussions organized as: (i) the evaluation of CORE-II wind speed with in-situ observation (Section 4.1); (ii) the time mean features of SST and its seasonal cycle over the key regions of the Indian Ocean, including the AS, BoB, Eastern Equatorial Indian Ocean (EEIO) and Thermocline Ridge (TR) region (Section 4.2); (iii) surface salinity and BL (Section 4.3); (iv) subsurface features of temperature and salinity over AS, south eastern AS (SEAS), BoB, EEIO ( Section 4.4); (v) surface and subsurface equatorial currents in CORE-II models and observations (Section 4.5); (vi) Indian Ocean meridional overturning circulation (Section 4.6). The impact of increased model resolutions is described in Section 5. Major findings from our analysis and its future implications are finally summarized in Section 6.

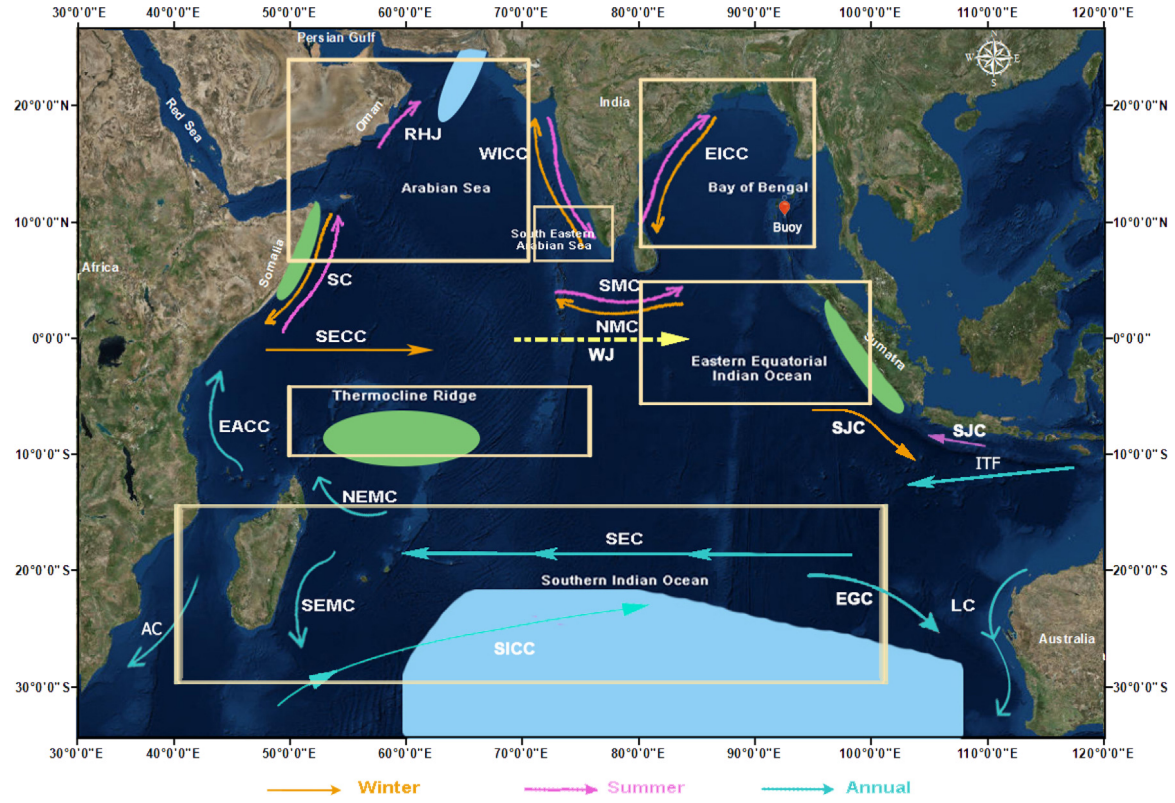


**Fig. 1a.** Schematic representation of identified current branches over north Indian Ocean during summer (JJA:pink), winter (DJF:orange) and as annual mean (cyan). Current branches are the South Equatorial Current (SEC), South Equatorial Counter Current (SECC), Northeast and Southeast Madagascar Current (NEMC and SEMC), East African Coastal Current (EACC), Somali Current (SC), Ras-al-Hadd Jet (RHJ), East India Coastal Current (EICC), West India Coastal Current (WICC), Southwest and Northeast Monsoon Currents (SMC and NMC), the Wyrtki Jet (WJ), Leeuwin Current (LC), Agulhas Current (AC), South Indian Ocean Counter Current (SICC), Eastern Gyral Current (EGC), South Java Current (SJC) and Indonesian Through Flow (ITF). Upwelling and subduction zones are shown in green and blue shades, respectively. The buoy location at 94°E and 10.5°N is shown as a red dot in the Bay of Bengal. The different sub-regions used for the time series comparison are evidenced as light-yellow color boxes, and they correspond to Arabian Sea (AS), Bay of Bengal (BoB), South Eastern Arabian Sea (SEAS), Eastern Equatorial Indian Ocean (EEIO), Thermocline Ridge (TR) and Southern Indian Ocean (SIO).

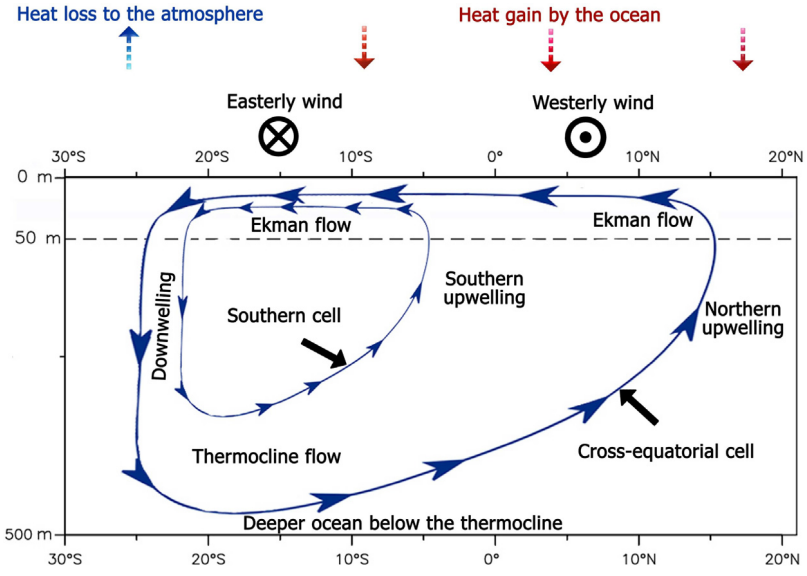


**Fig. 1b.** Conceptual illustration of the time-mean meridional overturning circulation of the upper Indian Ocean (first 500 m) consisting of a southern and a cross-equatorial cell (Based on Lee, 2004).

## 2. CORE-II simulations and the goals of this paper

The first phase of the Coordinated Ocean-ice Reference Experiments (CORE) project (CORE-I) made use of a synthetically constructed normal year forcing (NYF; Large and Yeager, 2004) with seven modeling groups participated in the study of Griffies et al. (2009). An underlying question pursued with CORE is whether models using the same atmospheric state (atmospheric state is prescribed over a fixed annual cycle) will produce broadly similar simulation features. However, analyses showed many differences in the simulated results. For example, models

are unable to simulate the realistic MOC; also models are unable to reach an equilibrium state after a transient phase that in turn prompted further model development and improvement (see more details in Griffies et al., 2009). The second phase (CORE-II) makes use of the interannually varying atmospheric forcing (IAF) of Large and Yeager (2009) over the 60-year period from 1948 to 2007. Details of the CORE-II protocol are given by Danabasoglu et al. (2014). The CORE-II project is the largest coordinated effort to assess the scientific integrity of global ocean/sea-ice simulations. It is now included as Phase-I of the Ocean Model Inter-comparison Project (OMIP), a part of the World Climate Research Programme Coupled Model Inter-comparison Project-phase 6 (CMIP6; Eyring et al., 2016), as documented by Griffies et al. (2016).

CORE-II simulations are readily comparable to historical observations given their historical forcing. Hence, CORE-II experiments facilitate the assessment of global ocean/sea-ice simulations and allow one to probe ocean processes active on sub-seasonal to decadal time scales (e.g., Danabasoglu et al., 2014, 2016; Griffies et al., 2014). At present, there are nine CORE-II assessment papers published in the journal Ocean Modeling that provide detailed analyses over the Pacific, Atlantic, Southern and Arctic Oceans. We here focus on the Indian Ocean. Since the ISMR prediction is dependent on the mean oceanic and atmospheric conditions, the central question addressed in this paper is: how well do global ocean/sea-ice models capture the mean state and seasonal cycle of the Indian Ocean? Most models employ one to two degrees horizontal grid spacing, though there are two that use finer spacing (~0.25 degree), thus admitting mesoscale eddies in the low latitudes and correspondingly fine scale currents.

## 3. Model and observational data used in this study

### 3.1. Models

We provide a summary of 16 global ocean/sea-ice model configurations in Table 1, with further details provided in the CORE-II papers of Danabasoglu et al. (2014) and Farneti et al. (2015). We focus on the 5th CORE-II forcing cycle and use model years corresponding to years of available observations for 1982–2007. The surface fluxes of heat, freshwater/salt, and momentum are determined using the CORE-II inter-annual forcing (IAF) atmospheric datasets, the model's prognostic SST and surface currents, and the bulk formulae described in Large and Yeager (2004, 2009). There is no restoring term applied to SST. SSS restoring is used to prevent unbounded salinity trends in all the model simulations used for this study. The NEMO-based models convert SSS restoring to a freshwater flux. All the other models apply SSS restoring as a salt flux. The restoring time scales vary considerably by days to years between the groups. Weak restoring with time scales of about 4 years were used in FSU, KIEL and NCAR, moderate restoring with time scales of 9–12 months were used in AWI, BERGEN, CERFACS, CMCC, CNRM, GFDL-MOM, ICTP and MRI, strong restoring with time scales of 50–150 days were used in ACCESS and GFDL-GOLD (see Appendix C in Danabasoglu et al. (2014) for more details on SSS restoring technique). The vertical mixing scheme used in different models is detailed in Appendix A of Danabasoglu et al. (2014).

For SST, we also make use of nine corresponding climate models (Table 2) from the Coupled Model Inter-comparison Project Phase 5(CMIP5; Taylor et al., 2012), utilizing historical runs forced with natural and anthropogenic radiative gases to simulate climate over years 1850–2005. We use CMIP5 simulations from January 1982 to December 2005 for generating a monthly climatology. There are many studies which show that ISMR variability is mainly governed by the mean state SST in the Indian Ocean (Lee et al., 2010; Li et al., 2001). Most of the coupled models show large cold biases in SST in the Indian Ocean, especially in the AS. The cold bias will have large impacts on the coupled feedbacks and thus the monsoon. Sujith et al. (2019) showed that improvements in mean state of SST in coupled model (CFSv2) have led to realistic simulation of oceanic modes of variability over Indian Ocean (IO), Pacific (i.e. ENSO, Indian Ocean Dipole (IOD)) and that lead to improve simulation of ISMR. The very purpose of CORE-II experiments is to see how the ocean models perform with a prescribed atmospheric state. In the coupled models the exact cause of the SST bias is not yet known hence we used SST simulations from both the forced and coupled model with same ocean configuration to delineate the probable source of the SST bias. The comparison between CORE-II and CMIP5 SST patterns offers a means to expose the role of atmosphere-ocean coupling with a dynamical atmospheric model on SST patterns. A more complete comparison of CORE-II and CMIP5 simulations is beyond our scope.

### 3.2. Observations and reanalysis data used for the model evaluation

We make use of the following observational and reanalysis data to evaluate the CORE-II simulations.

- Monthly one degree gridded optimum interpolation (OI) SST product (Reynolds et al., 2002) for 1982–2007 is taken from the National Oceanic and Atmospheric Administration (NOAA).
- The subsurface temperature and salinity are taken from the World Ocean Atlas (WOA09) climatology (Locarnini et al., 2010; Antonov et al., 2010; Boyer et al., 2009). We also use WOA09 for the SSS. In WOA09, data until 2006 were used to compute the climatology. However, more Argo profile data started in 2007 in the Indian Ocean. Including those years of data in the climatology may represent different mean state as compared to mean state based on data until 2006. Since the CORE-II simulations ran until 2007, hence we used WOA09 for this study.
- Surface currents are taken from the Ocean Surface Current Analysis (OSCAR, Bonjean and Lagerloef, 2002). The OSCAR product is available at 0.33° spatial resolution and 5 day averaged. For this study, we computed monthly climatologies from the 5-day averaged data for the period 1993–2007. We also use ship drift climatology from Cutler and Swallow (1984) as well as the near-surface current (0–15 m) climatology (version 2.07) from satellite-tracked drogued drifter velocities gridded at 0.5 × 0.5° resolution (Lumpkin and Johnson, 2013). All these data were re-gridded to 1° × 1° conforms to the MOM grid for comparison.
- We employ monthly-mean 1° × 1° zonal and meridional subsurface currents from the Operational ocean (ORAS4) (Balmaseda et al., 2013) reanalysis product for 1982–2007. The long-term mean is calculated for this period. Inter-comparison studies of different reanalysis products over Indian Ocean show ORAS4 is performing best among most of the widely used products (Karmakar et al., 2017).
- Observed long-term monthly mean net heat flux (NHF) was used from National Oceanography Centre Southampton (NOCS; Berry and Kent, 2009) available at 1° × 1° resolution. We also used monthly-mean TropFlux (Praveen Kumar et al., 2013) NHF for 1982–2007 and computed monthly climatologies for the comparison.

We note that different observation based products differ among each other and this can adversely affect the assessment of model performance based on single observation. Thereby, by comparing the model simulations with multiple observational products, we may achieve robust results.

### 3.3. Datasets used for the wind speed evaluation

We used buoy observed wind speed data at 3 m height provided by National Institute of Ocean Technology (NIOT) under National Data Buoy Programme (NDBP) of the Ministry of Earth Sciences, Government of India (Premkumar et al., 2000), to compare the most widely used forcing fields from CORE-II, JRA55-do (Tsujino et al., 2018)

**Table 1**
List of models and their configurations used for the CORE-II inter-annual simulations following Danabasoglu et al. (2014). Note that z* represents the stretched geopotential vertical coordinate that absorbs motion of the free surface (see Adcroft and Campin, 2004 and Griffies (2009) for details).

| Group | Configuration | Ocean Model | Sea-ice model | Vertical | Orientation | Horizontal | Resolutionnominal |
|---|---|---|---|---|---|---|---|
| ACCESS | ACCESS-OM | MOMp1 | CICE4 | z* (50) | tripolar | 360 × 300 | 1° |
| AWI | FESOM-COREII | FESOM | FESIM | z (46) | displaced | 126 000 | 1° |
| BERGEN | NorESM | MICOM | CICE4 | sigma2 (51 + 2) | tripolar | 360 × 384 | 1° |
| CERFACS | ORCA1 | NEMO3.2 | LIM 2 | z (42) | tripolar | 360 × 290 | 1° |
| CMCC | ORCA1 | NEMO3.3 | CICE 4 | z (46) | tripolar | 360 × 290 | 1° |
| CNRM | ORCA1 | NEMO3.2 | Gelato 5 | z (42) | tripolar | 360 × 290 | 1° |
| FSU | | HYCOM 2.2 | CSIM 5 | hybrid (32) | tripolar | 320 × 384 | 1° |
| FSU-2 | | HYCOM 2.2 | CICE4 | hybrid (32) | tripolar | 500 × 382 | 1° |
| GFDL-MOM | ESM2M-ocean-ice | MOM 4p1 | SIS | z* (50) | tripolar | 360 × 200 | 1° |
| GFDL-MOM025 | CM2.5-ocean-ice | MOM5 | SIS | z* (50) | tripolar | 1440 × 1070 | 0.25° |
| GFDL-GOLD | ESM2G-ocean-ice | GOLD | SIS | sigma2 (59 + 4) | tripolar | 360 × 210 | 1° |
| ICTP | | MOM 4p1 | SIS | z* (30) | tripolar | 180 × 96 | 2° |
| MRI-F | | MRI.COM 3 | MK89; CICE | z (50) | tripolar | 360 × 364 | 1° × 0.5° |
| KIEL | ORCA05 | NEMO 3.1.1 | LIM 2 | z (46) | tripolar | 722 × 511 | 0.5° |
| KIEL025 | ORCA025 | | | | | 1442 × 1021 | 0.25° |
| NCAR | | POP 2 | CICE4 | z (60) | displaced | 320 × 384 | 1° |

**Table 2**
List of coupled climate models and their configurations used from CMIP5.

| | Atmosphere | Ocean | Modeling centre | Ocean resolution |
|---|---|---|---|---|
| ACCESS1–0 | 1.25° × 1.875° L38 | ACCESS-OM (MOM4p1) | Commonwealth Scientific and Industrial Research Organization (CSIRO) and Bureau of Meteorology (BOM), Australia | nominal 1° |
| CCSM4 | 0.94° × 1.25° L26 | POP2 | National Center for Atmospheric Research,USA | nominal 1° |
| CMCC-CM | T159L31 | OPA8.2 | Centro Euro-Mediterraneo per I Cambiamenti Climatici, Italy | nominal 1° |
| CNRM-CM5 | T127L31 (256 × 128) | NEMO | Centre National de Recherches Meteorologiques/Centre Europeen de Recherche et Formation Avancees en Calcul Scientifique, France | nominal 1° |
| GFDL-CM3 | 2° × 2.5° L48 | MOM4p1 | Geophysical Fluid Dynamics Laboratory, USA | nominal 1° |
| GFDL-ESM2M | 2° × 2.5° L24 | | | nominal 1° |
| GFDL-ESM2G | 2° × 2.5° L24 | GOLD | | nominal 1° |
| MRI-CGCM3 | T159L48 | MRI.COM3 | Meteorological Research Institute, Japan | nominal 1° |
| NorESM1-M | 1.875° × 2.5° L26 | NorESM-Ocean | Norwegian Climate Center, Norway | nominal 1° |

and DRAKKAR (Brodeau et al., 2010). The buoy location is at 94°E, 10.5°N in the BoB and shown in Fig. 1a as red dot. Daily wind speed from buoy is used for the comparison. The 3-hourly 55-km horizontal resolution JRA55-do, and the 6-hourly 75-km resolution DRAKKAR wind speed were used for the comparison. However, daily averages were computed from these 3-hourly and 6-hourly data to compare with daily buoy wind speed. These datasets have been corrected relative to reanalysis product ERA-Interim (Dee et al., 2011) for DRAKKAR and Japanese 55-year Reanalysis (Kobayashi et al., 2015) for JRA55-do products, analogous to how CORE-II has been corrected. We also used Cross-Calibrated Multi-Platform (CCMP; available at http://rda.ucar.edu/datasets/ds745.1/#!access) Surface Wind Vector Analyses (Atlas et al., 2009) for the spatial wind speed comparison. Here we provide a comparison of CORE-II with DRAKKAR and JRA55-do to understand the reliability of these products for the Indian Ocean simulation. There are notable differences in spatial resolution (CORE-II: 2° and JRA55-do: 0.5°) as well as differences in temporal resolutions (CORE-II and DRAKKAR : 6-hourly and JRA55-do: 3-hourly). Yet for the comparison we only considered daily averaged datasets from all products. The corrected CORE-II, JRA55-do and DRAKKAR data are available at 10 m height. For comparison, we interpolate the CORE-II, JRA55-do and DRAKKAR 10 m winds to 3 m using the logarithmic scale given by Stull (2011).

### 3.4. Assessment in sub-regions of the Indian Ocean

The Indian Ocean variability is very inhomogeneous (e.g. Schott et al., 2009). Hence, we find it useful to examine the simulations within sub-regions as shown in Fig. 1a. These regions include the Arabian Sea (AS): 50 – 70 °E and 6 – 25 °N, the Bay of Bengal (BoB): 79.5 – 95.5 °E and 7.5 – 23.5 °N, the South Eastern Arabian Sea (SEAS): 71 – 77 °E and 7 – 13 °N, the Eastern Equatorial Indian Ocean (EEIO): 80 – 100 °E and 5 °S – 5 °N, the Thermocline Ridge (TR): 50 – 75 °E and 5 °S – 10 °S and the Southern Indian ocean (SIO): 40 – 100 °E and 15 °S – 30 °S.

## 4. Results and discussions

### 4.1. Evaluation of CORE-II forcing fields

#### 4.1.1. Assessment of the winds and latent heat fluxes

Latent Heat Flux (LHF) is mainly determined by wind speed apart from near-surface air temperature and humidity. Thus, any error in

**Table 3**
Wind speed comparison statistics over Bay of Bengal (Buoy location 94°E, 10.5°N).

| | AN3 2006 ( no of points 365) | | | | |
|---|---|---|---|---|---|
| | Mean (m/s) | Standard Deviation (SD) (m/s) | Bias (m/s) | Correlation Coefficient (CC) | RMSD (m/s) |
| Buoy | 5.38 | 2.09 | – | – | – |
| CORE-II | 6.16 | 2.64 | 0.78 | 0.80 | 1.75 |
| JRA55-do | 4.98 | 2.17 | −0.4 | 0.84 | 1.26 |
| DRAKKAR | 5.03 | 2.20 | −0.35 | 0.86 | 1.20 |

**Table 4**
LHF Comparison statistics over Bay of Bengal (Buoy location 94°E, 10.5°N).

| | AN3 2006 (no of points 365) | | | | |
|---|---|---|---|---|---|
| | Mean ($W/m^2$) | Standard Deviation (SD) ($W/m^2$) | Bias ($W/m^2$) | Correlation Coefficient (CC) | RMSD ($W/m^2$) |
| Buoy | 144 | 44 | – | – | – |
| CORE-II | 166 | 62 | 22 | 0.70 | 50 |
| JRA55-do | 133 | 46 | −11 | 0.72 | 36 |
| DRAKKAR | 134 | 47 | −10 | 0.75 | 34 |

the computation of LHF due to inconsistencies in any of these components would reflect in the NHF. Rahaman and Ravichandran (2013) have documented the evaluation of CORE-II near surface humidity and air temperature. The findings of Rahaman and Ravichandran (2013) are briefly mentioned in Section 4.1.2. In what follows, we therefore restrict our comparison to the wind speed.

Fig. 2 shows the time series comparison of daily wind speed from corrected CORE-II, JRA55-do and DRAKKAR in 2006 over southern BoB. CORE-II wind speed reproduce the observed seasonal and intra-seasonal variability. However, for most of the year, it overestimates the buoy wind speed (Fig. 2). In contrast, JRA55-do and DRAKKAR winds more accurately capture the buoy-observed daily wind speed with slight under estimations. The statistics of wind speed comparison is given in Table 3. The CORE-II mean wind speed bias is 0.8 m/s with a root-mean-square deviation (RMSD) value of 1.75 m/s and a correlation coefficient of 0.8. The underestimation of JRA55-do and DRAKKAR wind speed with respect to buoy observation is reflected with mean bias of −0.40 m/s and −0.35 m/s respectively (Table 3). However, the RMSD values in JRA55-do and DRAKKAR are much lower when compared to CORE-II. CORE-II wind speed have larger variability as compared to buoy observation with standard deviations of 2.1 m/s in the buoy and 2.6 m/s in CORE-II. JRA55-do and DRAKKAR standard deviation (SD) values are very close to the observed buoy value (Table 3).

Fig. 3a shows the 1993–2007 mean spatial distribution of wind speed from CORE-II, CCMP, JRA55-do and DRAKKAR. The basin-average mean wind speed is given within each panel (top right). The values are roughly similar except for CORE-II, which is slightly higher than the other products, which is also seen in the buoy comparison (Fig. 2). The mean wind speed structure over the Indian Ocean is dominated by the summer monsoon wind. The summer monsoon wind speed over AS is high as compared to BoB and it reflects in the annual mean structure. CORE-II wind speed is higher by ∼0.5 m/s over the west coast of Australia as compared to the other products. This region also shows the highest wind speed over the entire Indian Ocean. CORE-II wind is corrected by QuikScat wind (Large and Yeager, 2009), but still it shows higher values as compared to buoy and other wind products. Yu et al. (2007) have reported large LHF over this region in NCEP2 product as compared to other products, and attributed this bias to the strong wind. Sanchez-Franks et al. (2018) also noted LHF biases in this region and linked them to dry biases in humidity. The spatial distribution of monthly SD is shown in Fig. 3b. All wind products show that the variability is highest over the Somalia coast and it is ∼4–5 m/s in CORE-II, DRAKKAR and JRA55-do, but slightly lower values (∼3–4 m/s) are seen in satellite-based product, CCMP. The variability is lowest over equatorial Indian Ocean and in a zonal band over the south Indian Ocean (20–25°S) in all products. The SD values over these regions are similar in DRAKKAR, CCMP and JRA-do, but slightly larger values are seen in CORE-II.

To understand the wind impact on LHF, we computed latent heat fluxes using bulk formula (see details in Rahaman and Ravichandran, 2013) by using buoy observed atmospheric fields but replacing buoy wind speed with CORE-II, JRA55-do and DRAKKAR wind speed fields. The daily LHF comparison is shown in Fig. 4. The wind impact on LHF shows RMSD values of ∼50 $W/m^2$ and a mean bias of ∼22 $W/m^2$ in CORE-II. The underestimation of wind speed in JRA55-do and DRAKKAR is reflected as mean LHF bias of −11 $W/m^2$ and −10 $W/m^2$ respectively. Sanchez-Franks et al. (2018) found that JRA-55 underestimates buoy wind speed in the BoB in agreement with results here. Biases in turbulent heat fluxes of the order reported in their work can have large implications for a product/model to correctly represent monsoon-related processes. The RMSD values of 36 $W/m^2$ and 34 $W/m^2$ are much lower in JRA55-do and DRAKKAR as compared to CORE-II. These results also corroborate the finding of Swain et al. (2009). They showed that over the SEAS during monsoon season, 1 m/s RMSD in wind speed can cause 45 $W/m^2$ RMSD in LHF. As expected the variability in CORE-II is also large with SD value 62 $W/m^2$ as compared to buoy SD value of 44 $W/m^2$. The SD in JRA55-do and DRAKKAR is also very close to the SD derived from buoy observations (Table 4).

#### 4.1.2. Specific humidity, air temperature, and radiative fluxes

Rahaman and Ravichandran (2013) evaluated CORE-II specific humidity (Qa) and air temperature (Ta) with independent *in situ* observations over the tropical Indian Ocean. They reported that the RMSD value of Ta is ∼0.5 °C, but a large drop in Ta observed during intense rainfall events are not well captured by CORE-II products. They also reported a change in 1 g/kg Qa can cause about 11–15 $W/m^2$ errors in latent heat flux. Qiu et al. (2004) showed that over the western North Pacific, the synoptic-scale heat fluxes have a large impact on SST and have typical amplitude of ±1 °C. The downwelling fluxes of shortwave and longwave radiation from the CORE-II product have been evaluated with the tropical moored buoy observations (Venugopal and Rahaman, 2019). They found the mean bias in CORE-II over the Atlantic Ocean is about zero and a RMSD of 43 $W/m^2$ and 12 $W/m^2$ for downwelling shortwave and longwave radiation, respectively. For the Indian Ocean with respect to Research Moored Array for African–Asian–Australian Monsoon Analysis & Prediction (RAMA) buoy the mean bias is roughly -3 $W/m^2$ and −8 $W/m^2$ but with large RMSD values of 50 $W/m^2$ and 14 $W/m^2$ for downwelling short and longwave radiation, respectively. The variability is also underestimated with standard deviations of 70 $W/m^2$ in RAMA for shortwave whereas in CORE-II it is 48 $W/m^2$. In the case of longwave, variability is larger in CORE-II (23 $W/m^2$) as compared to buoy values of 18 $W/m^2$. CORE-II forcing fields compare reasonably well to observational-based measures as well as other reanalysis products.

### 4.2. Sea surface temperature

In this section, we offer a particularly extensive analysis of the SST given its importance for Indian Ocean climate variability and due to its relatively precise observational measures. For the analysis purpose, we regrided all models and observed SST and NHF dataset uniformly on a 1° x 1° grid.

#### 4.2.1. Spatial patterns

*4.2.1.1. SST patterns from CORE-II simulations.* Fig. 5 shows the annual mean SST bias for each model together with the model ensemble mean bias. The observed and model ensemble mean SST is also shown in the upper left corner of each panels. The annual mean is computed over the period 1982 to 2007 for both observations and models. The OI-SST

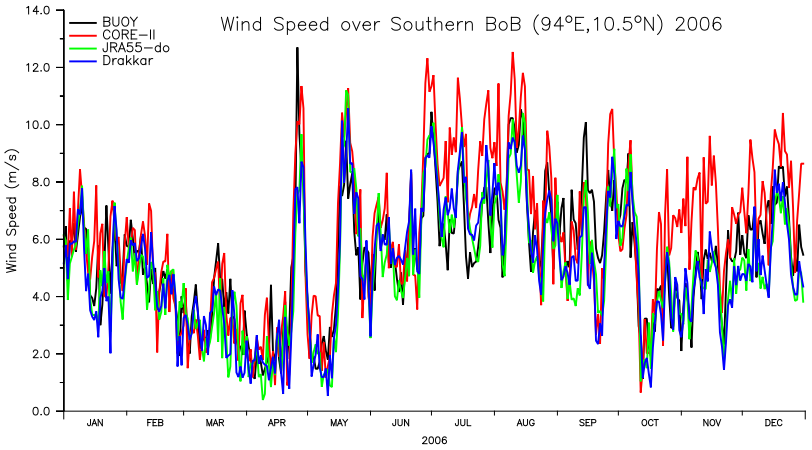


**Fig. 2.** Daily wind speed comparison of CORE-II, JRA55-do and DRAKKAR with buoy data over the southern Bay of Bengal at 3 m height for 2006.

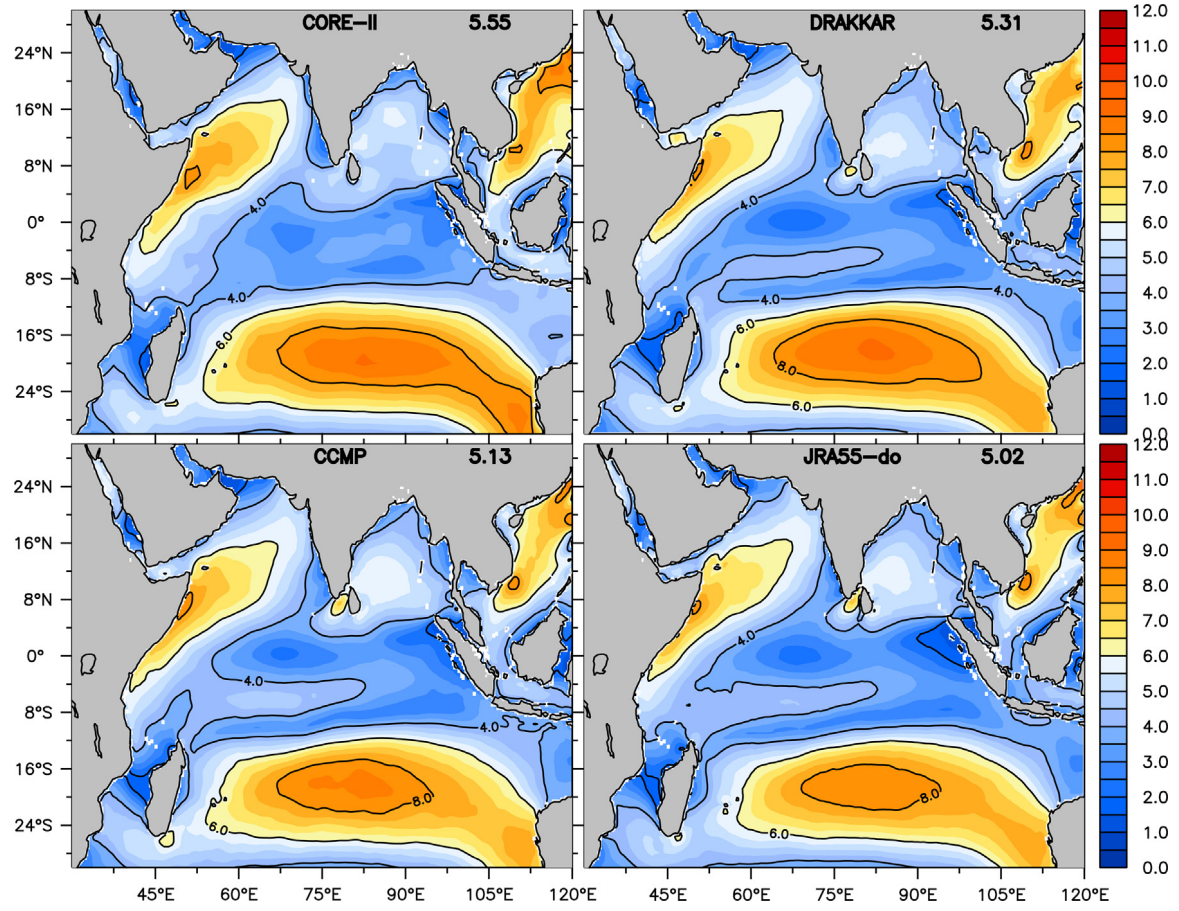


**Fig. 3a.** Mean wind speed (m/s) at 10 m height from CORE-II, DRAKKAR, CCMP and JRA55-do. Average over 1993–2007 is taken. The basin-average mean values are given in the upper right corner of each panel.

data is based on advance very high resolution radiometer (AVHRR) satellite data (Reynolds et al., 2002) which is available from April 1981, hence we used 1982–2007 to compute monthly climatology. Observations (Fig. 5a) show SST cooler in the west and warmer in the east (Murtugudde and Busalacchi, 1999; Schott et al., 2009) and a tongue of relatively warm SST (>29 °C) in the equatorial Indian Ocean, forming the Indian Ocean warm pool (Fasullo and Webster, 1999; Rao et al., 2015; Rao and Ramakrishna, 2017). The CORE-II ensemble mean (Fig. 5b) reproduces this warm pool structure both in terms of the magnitude and spatial extent. Looking at singular model annual means (Fig. 5d-s, contours) almost all of them reproduce the observed patterns. Two exceptions are AWI and ACCESS, where the maximum SST does not exceed 28 °C, and show a basin-wide cold bias (shaded values) including the warm pool region. Zonal variation of the SST pattern is well reproduced in all the CORE-II simulations. The ensemble mean SST pattern nearly replicates the observed mean SST spatial pattern. Individual models show biases of +/− 1 °C with a warm bias over the southwest Indian Ocean and cold bias over the AS and BoB. No significant improvement is seen in the two eddy-permitting models GFDL-MOM025 and KIEL025 as compared to their coarser resolution companion configurations. Therefore, biases may be arising more from improper representation of physical parameterizations (e.g., boundary

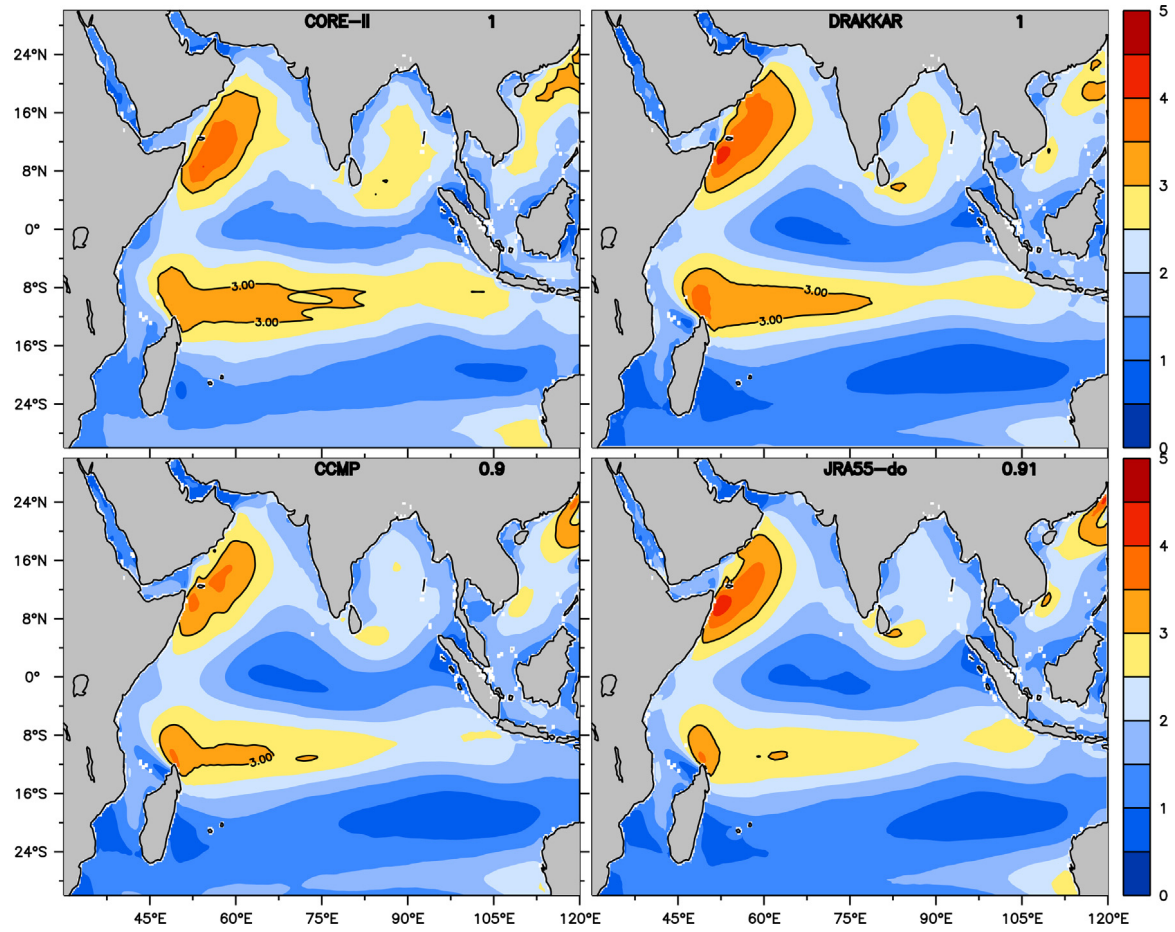


**Fig. 3b.** Monthly standard deviation (1993–2007) of wind speed (m/s) at 10 m height from CORE-II, DRAKKAR, CCMP and JRA55-do. The basin averaged mean values are given in the upper right corner of each panel.

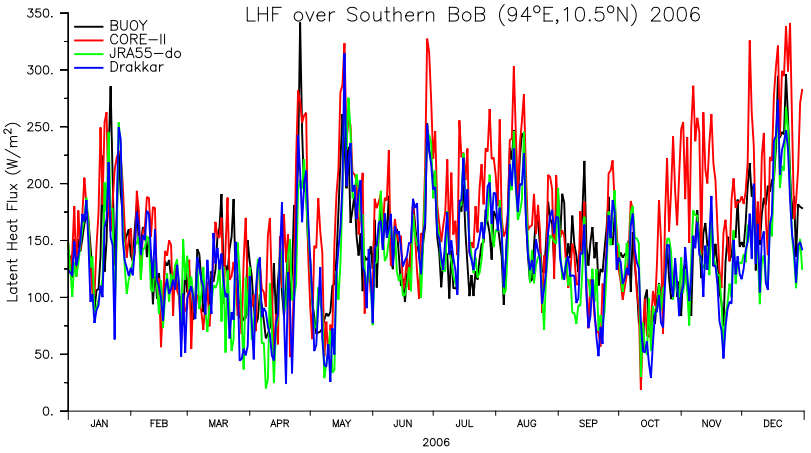


**Fig. 4.** Latent Heat Flux (LHF) computed from buoy observations (black) and replaced buoy wind speed with CORE-II (red curve), JRA55-do (green curve) and DRAKKAR (blue curve) wind speed fields. In the calculation of LHF only wind fields are changed, while all other fields are from observations. This comparison reveals the impact of wind speed on LHF.

layer processes) than coarse grid resolution or it may be also due to surface forcing bias.

Previous studies have shown that the NHF accounts for most of the tropical Indian Ocean (TIO) SST variability (Murtugudde and Busalacchi, 1999; Klein et al., 1999). Over the AS, apart from the NHF, oceanic processes also play a major role in the SST variability (Shenoi et al., 2002). However, SST over BoB is more air–sea flux driven due to the Bay's BL (Vialard et al., 2012). In the tropical southwest Indian Ocean (SWIO), ocean dynamics plays an important role at all timescales due to local and remotely-forced ocean dynamics (Lau and Nath, 2004). Murtugudde and Busalacchi (1999) and Xie et al. (2002, 2009) have shown that SST variability over this region is forced by thermocline variability and mixed layer-thermocline interactions. The warm SST bias over this region is coincident with the warmer thermocline temperature bias over the same region (see Fig. 19). The NHF bias computed from model SSTs is uniform throughout the basin (~10 W/m$^2$) in all these models (not

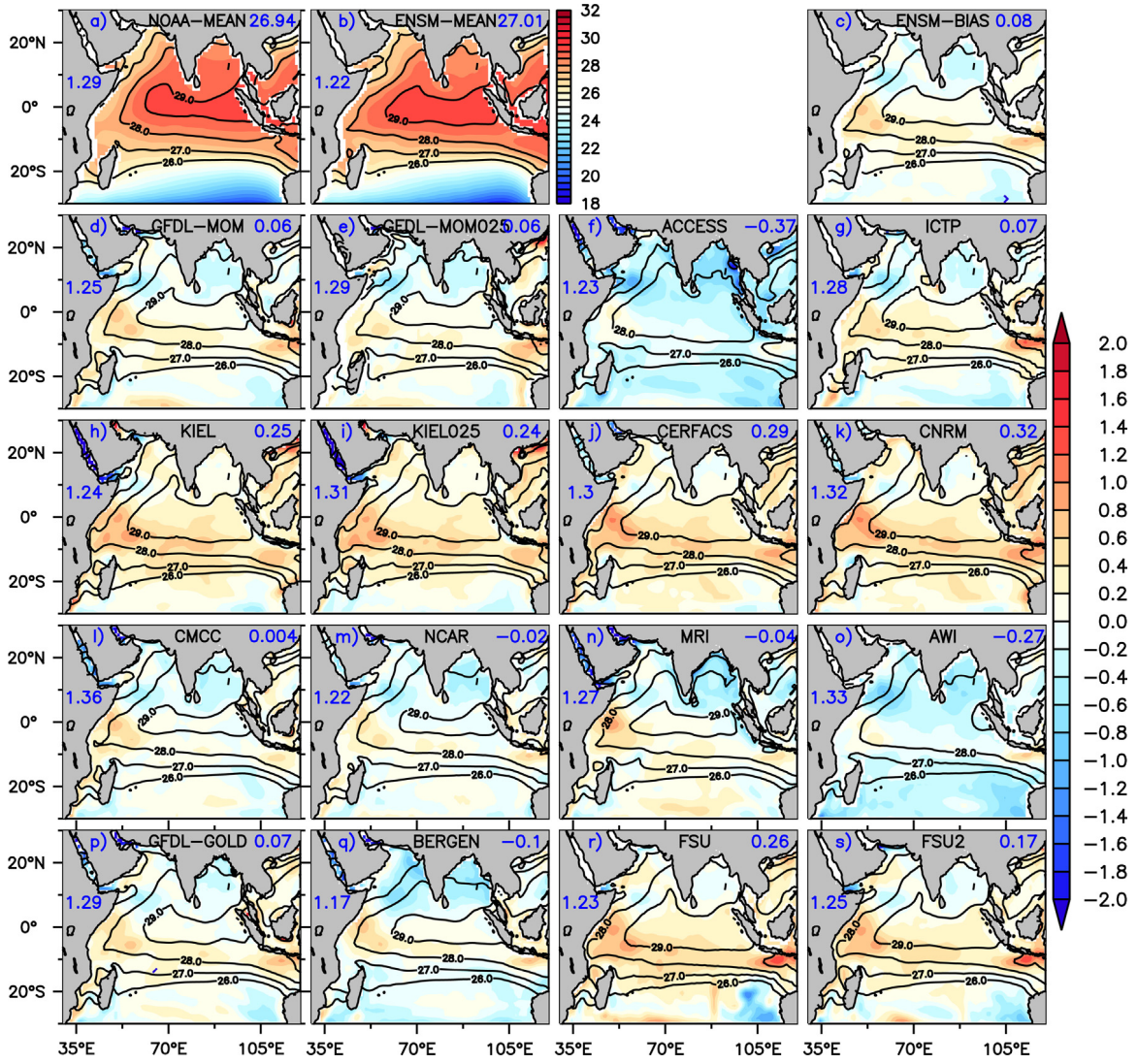


**Fig. 5.** Annual mean SST bias (model minus observation) from all model simulations are shown in color (panels d-s). The contours show the annual mean SST (1982–2007) of the 5th CORE-II cycle. The model ensemble mean bias is shown in the upper right panel (c). Observed annual mean SST from observation is shown in upper left panel from NOAA-OI (Reynolds et al., 2002) (a). The ensemble mean from CORE-II models is shown in the upper middle panel (b). Contour levels for the NOAA-OI observation and all models are the same. Units are in degrees Celsius. The basin averaged mean (upper right corner) and its standard deviations (left) are also given in each panel in blue colors.

shown), which further confirms this finding. The NEMO-based models (CERFACS, CNRM, CMCC and KIEL) show slightly larger warm bias to the south of the equator as compared to other models.

In the AS and the BoB, almost all simulations show a cold SST bias. The annual mean cold bias over these regions mainly arises from a large cold bias during March (Fig. 6). Chowdary et al. (2015, 2016) have shown that the seasonal SST over the BoB is governed by the seasonal NHF. But the observational study of Thangaprakash et al. (2015) show that vertical processes and horizontal advection also play a significant role in the seasonal SST tendency over the BoB. The NHF in CORE-II simulated models does not differ much with the TropFlux observations (see Fig. 11b and Section 4.2.2.2). Hence, the different magnitudes for the SST bias in CORE-II simulated models over the BoB could be due to the vertical processes and horizontal advection, thus supporting the finding of Thangaprakash et al. (2015).

In the AS, the Great Whirl and the southern eddy are two dominant anti-cyclonic eddies present near the Somalia coast. The Great Whirl has been observed to form during late May and early June between 5°N and 10°N. A large branch of the East African Coastal Current (EACC) turns offshore after crossing the equator at about 2°N to 3°N and forms the Southern Gyre (SG). The SG is a large anticyclonic retroflection cell with a well-marked wedge of cold upwelled water attached to its northern flank (the southern cold wedge). A third anticyclonic eddy named the Socotra Eddy (SE) is frequently present in the northeast of the Island of Socotra (Beal and Donohue, 2013; Beal et al., 2013). The very prominent small circular patch of cold SST bias seen over these regions, found in most of the CORE-II models, represents the presence of these anti-cyclonic eddies in July and October (Figure not shown). Most of the models show a cold bias with ACCESS showing the largest (~1.5 °C). GFDL-MOM group of models also shows a fairly large cold bias, whereas this bias is relatively small in the NEMO group of models. Annual mean bias over the BoB in the NEMO models and FSU are least among all the model simulations.

The region of the equatorial Indian Ocean and latitudes to its south show a positive bias (~0.6 °C) in all simulations except AWI and ACCESS, whose simulations show a small cold bias (~0.4 °C). All biases are within observational errors (Bhat et al., 2004; Senan et al., 2001). Furthermore, the flux errors are larger than the corrective fluxes needed to correct these SST biases which make it difficult to assign any errors in the models (see Murtugudde et al., 1996). However, the high mean SSTs are close to atmospheric convective thresholds and thus even small errors can lead to large errors in a coupled climate model. The CORE-II models realistically simulate the spatial distribution and zonal variation of SST in the Indian Ocean. The basin-wide bias is


**Fig. 6.** Mean SST bias (model minus observation) in March from all model simulations are shown in shade (panels d-s) from the 5th CORE-II cycle. The overlaid contour levels are for the mean SST in March. The ensemble mean from CORE-II models is shown in the upper middle panel (b). Ensemble mean bias for all models is shown in upper right panel (c). Observed mean SST in March from observations is shown in the upper left panel (NOAA-OI) (a). Contour levels for NOAA-OI observation and all models are same. The basin averaged mean (upper right corner) and its standard deviations (left) are also given in each panel in blue colors. Units are degrees Celsius.

within +/− 1 °C seen in almost all the models, which may arise from problems representing ocean physics as well as atmospheric forcing. We conjecture that the most important physical process is related to vertical mixing, given the importance of upper ocean boundary layer processes for setting the SST. These results suggest that a focus on improved physical parameterizations may, in the near term, offer more advances in Indian Ocean simulations than refinement of the grid resolution. This conclusion is supported by Benshila et al. (2014).

*4.2.1.2. Comparing SST from CORE-II and CMIP5 simulations.* We here compare SST from CMIP5 coupled models using the same ocean component as the CORE-II models. In particular, we analyze SSTs from CMIP5 historical simulations from the nine models that employ the same ocean configuration used in our CORE-II study (Table 2). Compared to forced CORE-II model simulations, coupled CMIP5 simulations show SST biases that are not uniformly distributed across different seasons. They also show a similar pattern to that of the forced simulations described in Section 4.2.1.1, but with larger amplitude. The larger biases suggest the amplification of SST errors that arise from coupling with an interactive atmospheric model.

Previous studies have identified a cold SST bias in the Indian Ocean in coupled climate models (Pokhrel et al., 2012a,b; Chowdary et al., 2015, 2016; Prasanna, 2015). Fathrio et al. (2017a) examined the western Indian Ocean SST biases among CMIP5 models and found that about half of the models show positive SST biases, while others show negative bias. The models with cold SST biases exhibit a colder bias in the entire tropical Indian Ocean throughout the year. The positive bias was attributed to relatively weak southwest monsoonal winds over the AS and an equatorial southeasterly wind bias. The warm SST biases persisted until boreal fall, and then disappeared in winter (Li et al., 2015). All CMIP5 models show cold SST biases over the northern AS during the pre-monsoon season (Marathayil et al., 2013; Sandeep and Ajayamohan, 2014; Levine et al., 2013; Li et al., 2015; Fathrio et al., 2017a). Studies show that anomalous advection of cold surface air from the south Asian landmass during boreal winter contributes to the cold SST biases over the north AS (Marathayil et al., 2013; Sandeep and Ajayamohan, 2014).

We show the annual mean SST (contour) and bias (color) from the CMIP5 simulations in Fig. 7. Except for CESM and CMCC, none of the CMIP5 models reproduce the observed warm pool over the equatorial Indian Ocean (Rao et al., 2015). The majority of the CMIP5 models show a basin-wide cold bias with highest bias in the northern AS up to 4 °C. The north AS cold bias is more than 3 °C in MRI whereas CESM shows the smaller cold bias of ~0.6 °C. CESM, CMCC and MRI

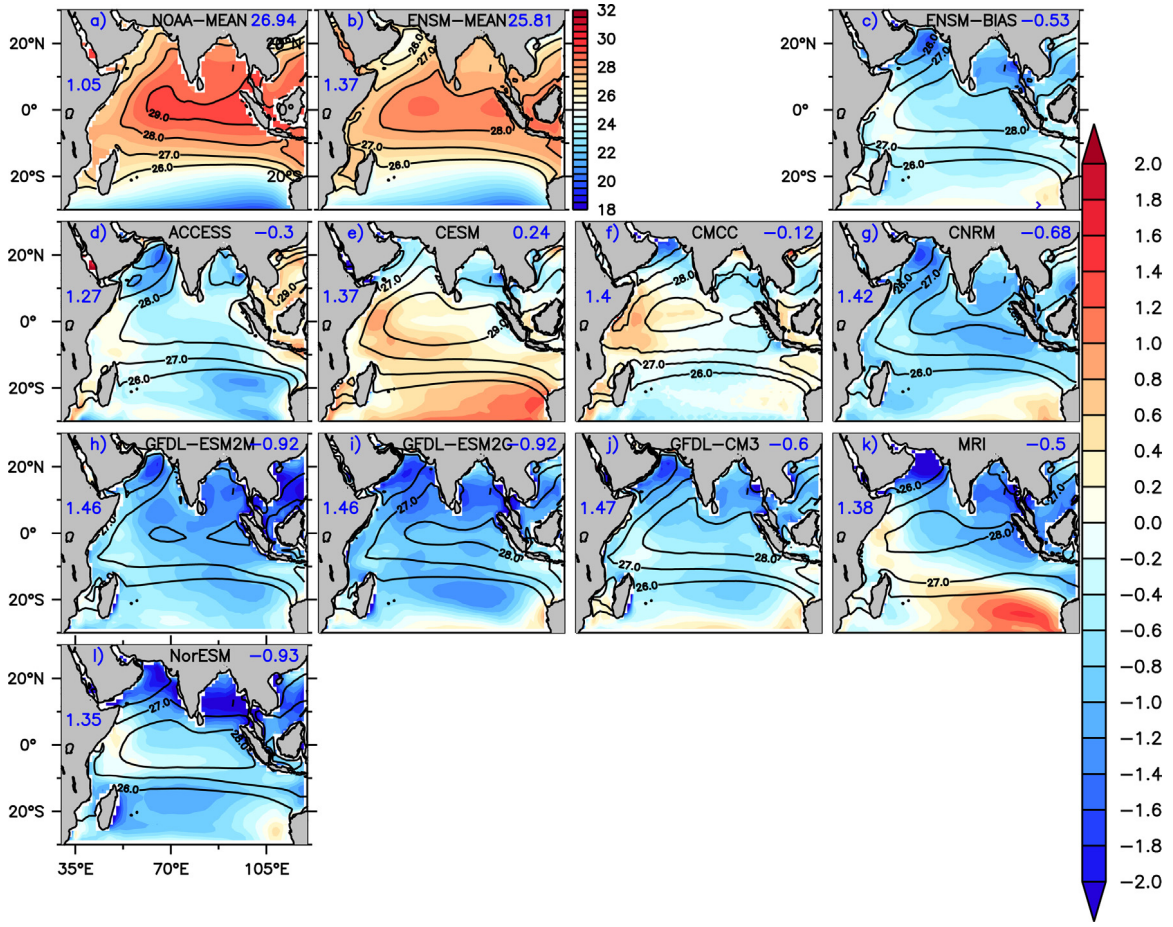


**Fig. 7.** Annual mean SST bias (model minus observation) from CMIP5 simulations (shade), with contours for the mean SST. The ensemble mean from the CMIP5 models is shown in the upper middle panel (b). The CMIP5 model ensemble mean bias is shown in the upper right panel (c). Observed annual mean SST is shown in upper left panel from NOAA-OI (a). Contour levels for the NOAA-OI observation and all models are the same. The basin averaged mean (upper right corner) and its standard deviations (left) are also given in each panel in blue colors. Units are degrees Celsius.

show a warm positive bias (of up to 1.6 °C) over the western equatorial Indian Ocean and southeast Indian Ocean off the Australian Coast. The overall basin wide cold bias is weakest in CMCC (−0.12 °C) and largest in NorESM(−0.93 °C). The largest basin averaged cold bias in CORE-II ocean only simulations is −0.37 °C in ACCESS. Biases in the NCAR CORE-II model are only ∼0.1–0.2 °C to the south of the equator. However, when coupled as part of CESM, this model shows roughly five to ten times larger biases up to ∼1 °C.

The large cold bias in the CMIP5 models over the northern AS in the annual mean mostly arises from the cold bias during February–April, which peaks in March (Fig. 8). The SST cold bias is larger than 3 °C in GFDL-ESM2M, GFDL-ESM2G, GFDL-CM3, NorESM and MRI during March. Sandeep and Ajayamohan (2014) show a similar cold bias, but with larger amplitude over the north AS in all CMIP5 models. They attributed this bias to an equatorward bias in the subtropical jet stream during boreal spring, thus causing excessive cooling of the northern AS and adjoining land regions. This cold bias in coupled models was also attributed to the northeasterly cold air temperature (Marathayil et al., 2013).

The cold bias in forced CORE-II simulations is much weaker when compared to coupled models that use the same ocean component (Figs. 5 and 7). The cold biases in the CORE-II simulations are ∼1 °C over the northern AS whereas they are ∼3 °C in the CMIP5 models, with even larger biases in the MRI and NorESM. These results suggest that the large northern AS SST biases in coupled models may arise from coupled dynamical feedbacks that amplify ocean errors. This hypothesis is supported by Fig. 9a, which shows the seasonal cycle of the mixed layer depth (MLD) in CORE-II models and WOA observations over the northern AS. The CORE-II MLDs are generally deeper than WOA during February–March. Fig. 9b shows the MLD vs SST bias over the northern AS. It can be seen that larger SST cold biases are associated with deeper MLDs as compared to observations. The correlation coefficient between MLDs and SST bias is 0.64, which is significant at the 99% confidence level. In Fig. 9b, the BERGEN simulation appears like an outlier. Without this simulation the correlation coefficient value reduces from 0.64 to 0.50 but it is still significant at the 95% confidence level. Tozuka et al. (2017) showed in the upstream Kuroshio Extension region in the North West Pacific that the deeper MLD is less sensitive to cooling by surface heat fluxes. However, Roxy et al. (2012) showed a shallow (deep) MLD enhances (suppress) the SST anomaly, thereby amplifying (lessening) the intra-seasonal variability of the monsoon in a coupled model (CFSv2) and argued that a prime focus should be on improving the mixed layer scheme of the ocean component in that model. This confirms the need of improvement of MLD in ocean models for a better simulation of SST over the northern AS.

These results suggest that the origin of SST bias during spring (February–April) mainly arise from the coupled feedbacks as well as MLD biases. The spatial distribution and magnitude of SST bias in CORE-II forced simulations are weaker than those in coupled simulations since the errors are amplified by coupled feedbacks. We conjecture that the basin-wide cold bias in CORE-II simulations arises from deficiencies in ocean vertical mixing, with biases enhanced due to coupled feedbacks in the coupled model simulations.

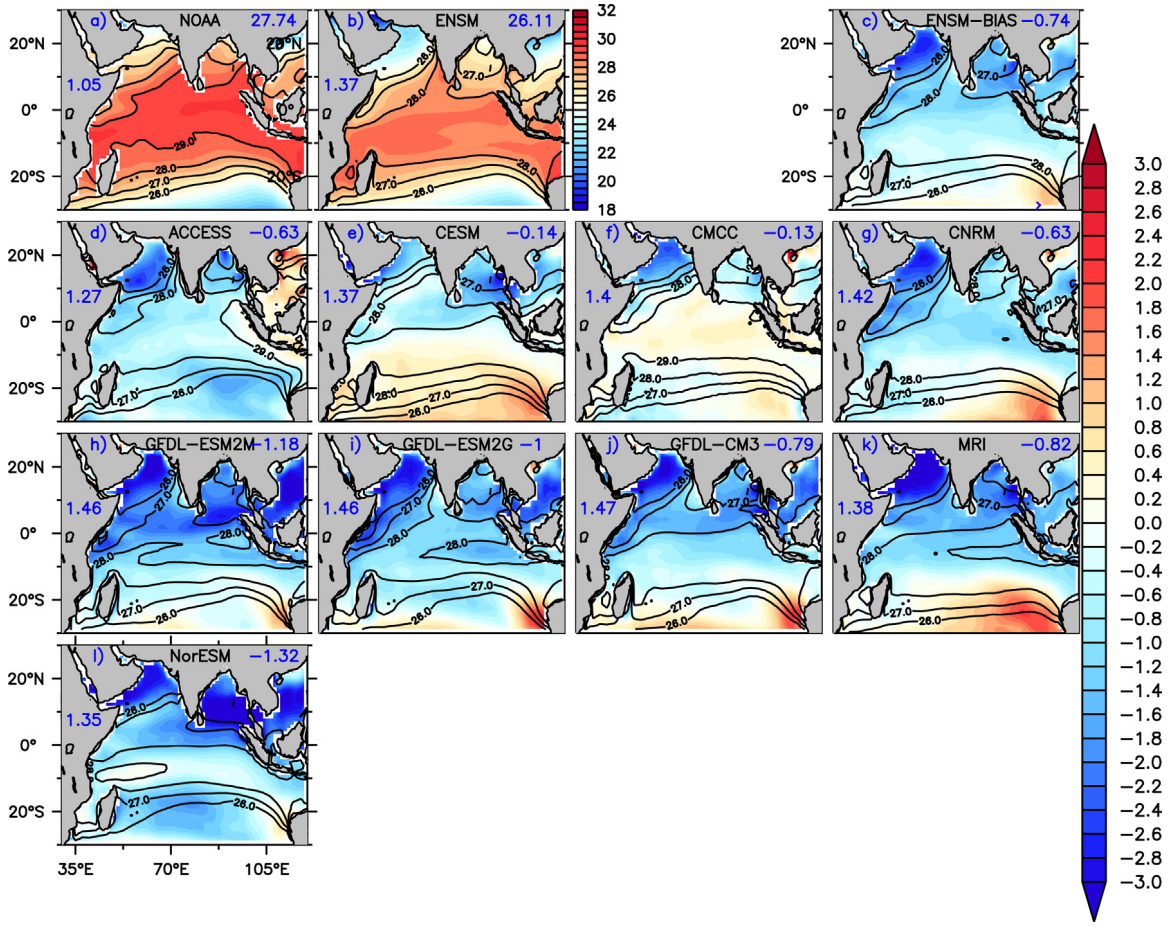


**Fig. 8.** March mean SST bias (model minus observation) from CMIP5 simulations are shown in shade. The ensemble mean from the CMIP5 models is shown in the upper middle panel (b). Ensemble mean bias for all models is shown in the upper right panel(c). Observed mean March SST is shown in the upper right panel (NOAA-OI) (a). The basin averaged mean (upper right corner) and its standard deviations (left) are also given in each panel in blue colors.

*4.2.2. Seasonal cycle of SST and net surface heat flux*

The Indian Ocean circulation and tracer property distributions exhibit great spatial inhomogeneity. Correspondingly, so is the spatial distribution of the SST bias. Hence, we here consider the area averaged seasonal cycle over the different sub-regions shown in Fig. 1 and described in Section 3.4. The ability of model simulations to correctly capture the seasonal SST variation is a difficult task, particularly over the north Indian Ocean.

*4.2.2.1. Arabian Sea (AS).* Fig. 10a shows the seasonal evaluation of SST over the AS from CORE-II simulations and its ensemble mean along with observation. The observed annual cycle over the AS shows a bimodal SST seasonality with the primary maximum during April–May and the secondary maximum in October (Murtugudde and Busalacchi, 1999; Vinayachandran and Shetye, 1991; Fathrio et al., 2017a). During April–May, prior to the onset of the Indian summer monsoon, the AS evolves to one of the warmest areas in the tropical oceans (Joseph, 1990; Joseph et al., 2006). All CORE-II simulations show bi-modal SST seasonality, but there exists inter-model spread that is largest during summer.

Observations show that SST reduces after the onset of the summer monsoon in June. It reaches a minimum during the peak summer monsoon (July–August) over the AS due to upwelling off the Somali Coast and Arabian Peninsula as well as due to latent heat loss caused by strong southwesterly monsoon winds (Shenoi et al., 2002). Another mechanism through which SST reduces over the AS is the export of heat through meridional overturning. Few models show lower SST during July–August with respect to NOAA-OI observation, while others show slightly higher. This behavior could be due to the different cross-equatorial heat transport among different models (Swapna et al., 2017).

The CMIP5 coupled model simulations show similar variations to those forced by CORE-II, but CMIP results show far more inter-model spread (Fig. 10c). The cold biases during winter and spring in the coupled models are larger (~2 °C) than the CORE-II models (~0.5 °C) (Fig. 10a,c). Coupled Model Inter-comparison Project Phase 3 (CMIP3) and other CMIP5 coupled models (not considered here) also show similar cold biases over the AS (Marathayil et al., 2013; Levine et al., 2013). Levine and Turner (2012) showed that coupled model SST biases over the northern AS are substantially larger than the observed interannual variability of AS SST, and in turn these biases affect the Indian summer monsoon simulations and forecasts (Narapusetty et al., 2015).

The AS seasonal cycle of NHF from the CORE-II models matches that of the TropFlux observation (Fig. 10b) during October–March, while the magnitude is about 20%–30% less than the observation. Despite this reasonably good match in surface heat flux forcing, the cold SST bias in CORE-II simulations indicates the role of oceanic process in seasonal SST evolution, which is also evident from the deeper MLD in all models (Fig. 9a). Recent studies by Parampil et al. (2016) have shown that TropFlux derived NHF over the NIO is more realistic when compared with OAFLUX and satellite derived products. All the CORE-II models underestimate the NHF as compared to observations (Fig. 10b) during March–October. Most models show a cold SST bias during spring but the majority shows warm bias during summer (July–August) (Fig. 10a). The wind speed is strong over AS in CORE-II during spring but it is weaker during peak summer (August) as compared to other wind speed

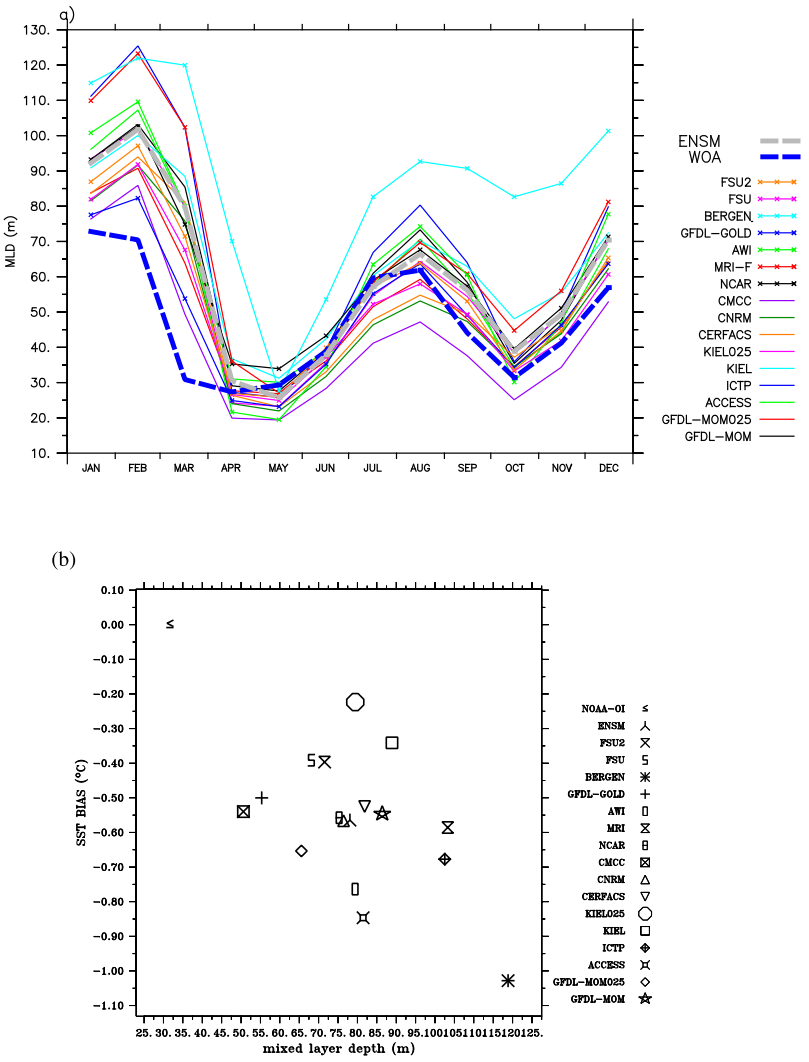


**Fig. 9.** (a) Seasonal cycle of MLD from all CORE-II model simulations and WOA observation averaged over northern AS (10–25°N, 55–70°E) (b) scatter plot of MLD vs SST bias over northern AS for the individual models in March. For the observations (NOAA-OI) the SST bias is just zero while the MLD (32 m) is the reference for that month. The correlation coefficient between model MLD and SST bias is 0.639, which is significant at 99% confidence level.

products (figure not shown). This leads to an over estimation of the LHF in model. The overestimation of the LHF due to CORE-II wind speed is also shown in Fig. 4 and Table 4. As previously noted, wind speed is not the sole factor determining the LHF (Rahaman and Ravichandran, 2013). They showed that the LHF overestimation is mainly due to the positive biases of CORE-II near-surface air temperature and specific humidity.

Fig. 10d shows the seasonal evolution of ensemble mean SST and NHF from observations, CORE-II and CMIP5 simulations. The NHF reaches its maximum in April whereas SST attains its maximum in May. Studies have shown that the seasonal evolution of SST tendency matches well with the NHF seasonal cycle (Chowdary et al., 2015; Sayantani et al., 2016; Kurian and Vinayachandran, 2007).

In summary, the bimodal semiannual cycle of SST in the AS is well captured by the CORE-II forced simulations, revealing weaker biases than the coupled CMIP5 models. We conjecture that the cold SST bias and under-estimation of SST maximum in the pre-summer monsoon season reflects a problem with simulated oceanic processes since the CORE-II ensemble NHF is reasonably well matched with both observational products. Additionally, the inability to reach the minimum SST during the summer monsoon season may arise from biases in the wind forcing (see Section 4.1.1) as well as simulated oceanic processes.

*4.2.2.2. Bay of Bengal (BoB).* Fig. 11a shows the SST seasonal cycle over the BoB from CORE-II simulated models and observation. As for the AS, the semiannual cycle is very prominent in the BoB, with peak SSTs in May and October. Although the SST reduces rapidly over the AS following the monsoon onset, SST in the BoB remains higher than 28 °C, making the BoB favorable for deep atmospheric convection (Gadgil et al., 1984; Graham and Barnett, 1987). The magnitude of SST reduction in the BoB is smaller (~1 °C) than in the AS (2–3 °C). This difference arises from the BL present in the BoB, with this layer suppressing ocean vertical mixing and thus maintaining a higher SST throughout the year (Thadathil et al., 2007; Shenoi et al., 2002; deBoyer Montégutet et al., 2007; Sprintall and Tomczak, 1992). The models are able to simulate the observed seasonal cycle but mostly underestimate the observed SST, with KIEL and KIEL025 as exceptions. This underestimation of SST could be due to the models' inability to simulate properly the (observed) BL thickness (Thadathil et al., 2007). Several studies point to the impact of BL on BoB's SST variation (e.g. deBoyer Montégutet et al., 2007; Saji and Yamagata, 2003; Saji et al., 2006; Girishkumar et al., 2011). The model study of Rahaman et al. (2014) suggested the importance of relatively fine vertical grid spacing (~2 m) to properly represent the BL features. Note that most of the CORE-II models have vertical grid spacing no finer than ~5 m in the upper ocean.

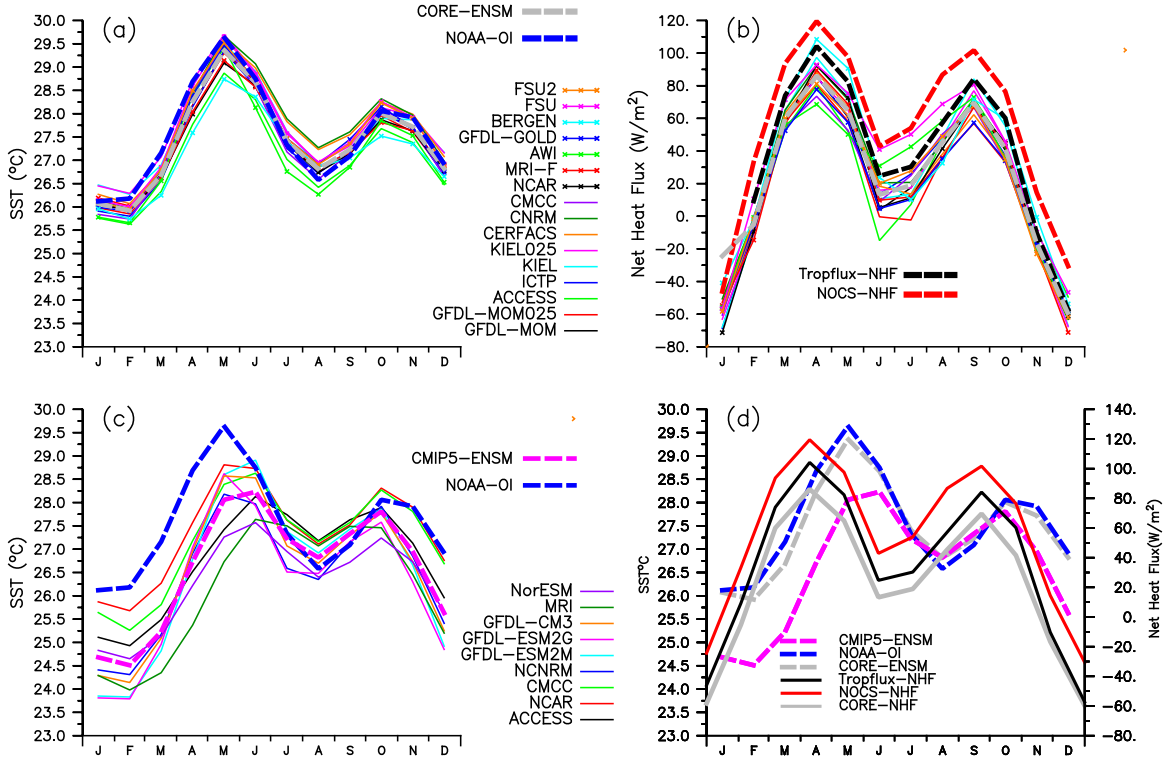


**Fig. 10.** Seasonal cycle of SST over the Arabian Sea (AS) from (a) CORE-II simulations (c) CMIP5 simulations. The model ensemble mean and observed SST are also shown as dashed thick gray and blue lines, respectively. (b) Seasonal cycle of net heat flux from all the CORE-II simulations as well as two observations (NOCS and TropFlux in dashed thick red and black lines, respectively). (d) Seasonal cycle of CORE-II and CMIP5 ensemble mean and NOAA-OI SST (left axis) and net heat flux (NHF) from CORE-II ensemble simulation and observations (NOCS and TropFlux; right axis). The legend for individual models is the same in panels a and b.

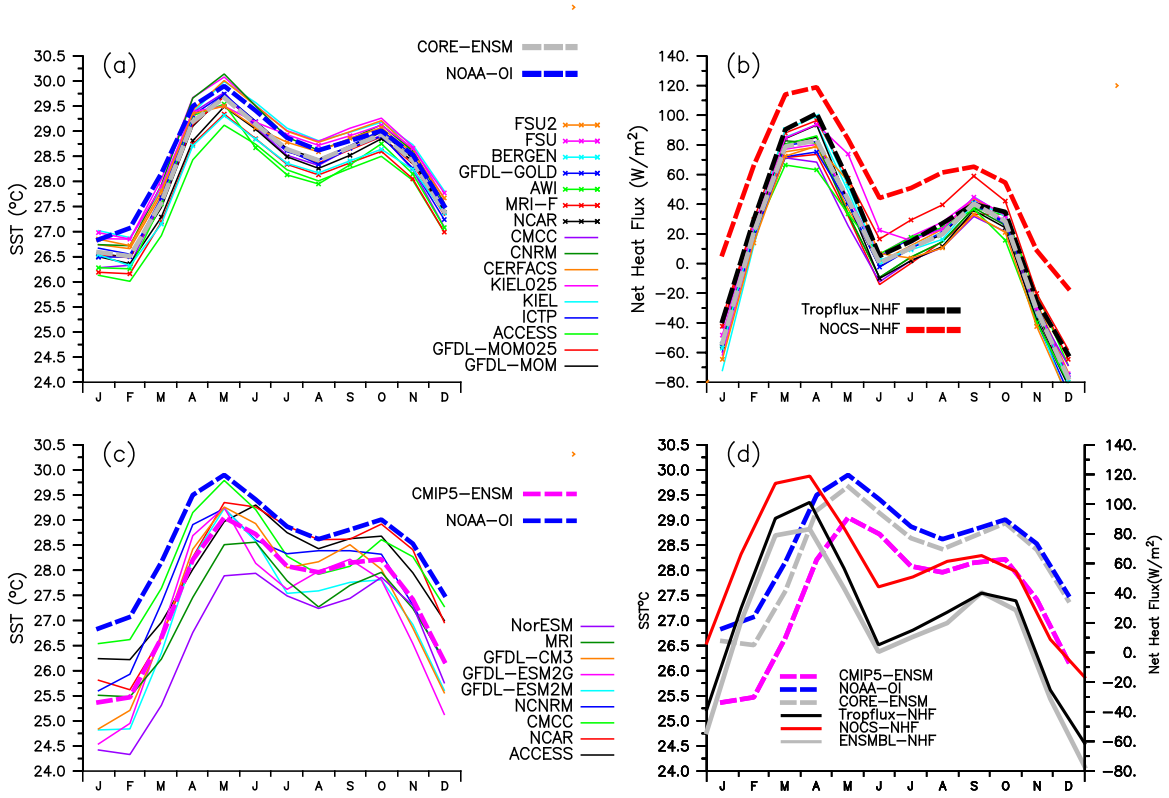


**Fig. 11.** Same as Fig. 10 but for the Bay of Bengal (BoB).

Further evidence for the oceanic role in establishing the SST biases can be seen in Fig. 11b, which shows that the CORE-II ensemble mean surface heat fluxes closely follow the TropFlux observations with little spread across the models. As pointed out by Parampil et al. (2016), data from NOCS overestimates the NHF compared to other observational products. This bias is also reflected in Fig. 11b where the NOCS NHF is larger than TropFlux throughout the year.

In contrast to the CORE-II forced simulations, the coupled CMIP5 simulations show larger SST bias ranging up to −2 °C almost throughout the year with maximum during February–May (Fig. 11c). The inter-model spread is large in coupled models compared to the CORE-II forced simulations. Fig. 11d shows the seasonal variation of the ensemble mean SST and the NHF from both CORE-II and CMIP5 along with observations, with CORE-II models better representing the seasonal variation of SST in the BoB than CMIP5 models, showing a rather uniform offset of 1 °C over the year compared to observations.

*4.2.2.3. Eastern Equatorial Indian Ocean (EEIO).* SST over the Indian Ocean generally shows large-scale seasonal variability, but SST variation in the EEIO remains within about ±0.5 °C (Fig. 12a). The mean SST is above 28 °C throughout the year, thus favoring deep atmospheric convection (Gadgil et al., 1984) and rainfall throughout the year. Fig. 12a shows the EEIO SST seasonal cycle from CORE-II forced models and observation. The observation shows that SST exceeds 29 °C throughout the year and peaks in April. All models are able to capture the observed seasonal cycle with comparatively small biases (~0.25 °C), except ACCESS and AWI, both of which show a systematic year-round cold bias of ~0.5 °C. Similar to the AS and the BoB, the NHF over the EEIO is also underestimated by all models compared to both observational products. The CORE-II ensemble mean value shows good agreement with the observations, but a large inter-model spread exists throughout the year, with all models showing systematically warm or cold biases. KIEL and FSU show positive SST biases during April–May despite a NHF that underestimates the observed values. This result suggests that the NHF may not be a major factor determining the evolution of SST during April–May, but that instead the ocean dynamics likely dominate. Over the EEIO, particularly off Java and further east, horizontal advection through the ITF and vertical entrainment by upwelling are the most important processes balancing the annual mean heat budget, and these processes in turn control the SST variation (Qu et al., 1994; Du et al., 2005). In the EEIO, the horizontal advection by the WJ is also expected to contribute to the SST (e.g. Halkides and Lee, 2009).

Coupled CMIP simulations show large cold biases throughout the year and inter-model spread is much larger than their CORE-II counter parts (Fig. 12c). The systematic inter-model spread is ~2 °C and the systematic bias is much larger (~1–1.5 °C) in coupled simulations compared to 0.25–0.5 °C in CORE-II simulations. The zonal wind stress over this region is westerly from March to October and largest during northern hemisphere spring and autumn, driving the bi-annually observed equatorial jets in spring and autumn (Wyrtki, 1973). These equatorial jets deepen the thermocline in the east, thus contributing to SST increase in the EEIO.

Fig. 12d shows the ensemble mean SST seasonal cycle from the CORE-II and the CMIP5 simulations along with observations. The ensemble mean NHF from the CORE-II simulations and observations (TropFlux and NOCS) are additionally overlaid. The CORE-II ensemble mean closely matches the observed SST seasonal cycle, whereas the CMIP5 simulations show a systematic cold bias throughout the year with a maximum bias of about 1.2 °C during December–January. Additionally, the peak SST in CMIP5 models is reached in May, which is one month after the observed peak in April. The NHF from the CORE-II ensemble is underestimated throughout the year except in autumn. As for the AS and the BoB, the EEIO NHF peaks one month earlier than the SST, so that the tropical Indian Ocean SST responds to NHF changes after roughly one month.

*4.2.2.4. Thermocline ridge (tr).* SST in the TR (also called the Seychelles Dome) region shows a dominant annual cycle, rather than a semiannual cycle as in the AS, the BoB and the EEIO (Levitus, 1987; Rao and Sivakumar, 1999; Vialard et al., 2009). SST in the TR region has a large impact on the Indian summer monsoon (Annamalai et al., 2005) and the tropical cyclone activity (Xie et al., 2002). Therefore, it is important for coupled prediction models to simulate the observed SST variability over TR. In particular, resolving its seasonal cycle provides a useful benchmark test for model performance. Fig. 13a shows the seasonal variation of SST from observation and the CORE-II simulations. Observational estimates show an increase in SST from August to April followed by decrease from May to July as the cross-equatorial wind starts evolving (Fig. 13a). Most of the model capture this seasonal variation, but they generally overestimate the observed SST throughout the year with a maximum during July–August (up to 1 °C). AWI and ACCESS capture the observed July–August cooling over the TR region. However, both models have a consistently cold bias over other sub-regions. The NHF is underestimated (Fig. 13b) systematically by all CORE-II simulations with an ensemble bias (−60 $W/m^2$) during July–August (Fig. 13b). Horizontal advection tends to warm the SST in austral winter owing to the southward Ekman heat transport associated with the Indian summer monsoon (Yokoi et al., 2012). Despite a large negative NHF in the CORE-II simulations, many models show a warm bias during August, thus suggesting the role of excess heat transport from north of the Equator by the wind driven Ekman transport. Yokoi et al. (2012) also showed that cooling by vertical turbulent diffusion in the ocean becomes most effective in the austral summer, owing to the shallow mixed layer and correspondingly shallow thermocline during that season. Positive SST biases may have arisen due to the reduced vertical cooling since the thermocline is deeper (85–140 m) than found in the observations (75–80 m) (not shown). Similarly, the CMIP5 simulations also capture the observed seasonal cycle of SST, but exhibit a larger inter-model spread than the CORE-II simulations. Analysis indicates that almost half of the CMIP5 models shows a warm bias and the rest show a cold bias, thus leading to an ensemble mean CMIP5 SST that is close to the observation. Nagura et al. (2013) analyzed 35 coupled general circulation models (CGCM) including some CMIP5 models for the simulations of the longitudinal biases in the Seychelles Dome. They showed that the CMIP5 models are unable to simulate the longitude of the upwelling dome and the magnitudes of the annual and semiannual cycles of thermocline depth variability in the dome region. These biases could help to explain why some of the CMIP5 models generally have problems reproducing the observed seasonal cycle of SST over this region. GFDL-ESM2G shows a systematic cold bias throughout the year (Fig. 13c). This region also shows that the NHF leads SST by about one month (Fig. 13d).

*4.2.3. Zonal SST variation along the equator*

Murtugudde and Busalacchi (1999) first reported that the mixed layer-thermocline interactions in the EEIO potentially imply a coupled feedback. Furthermore Saji et al. (1999) and Webster et al. (1999) showed that coupled feedbacks in the equatorial Indian Ocean are critical for variability in the tropical Indian Ocean. This variability mode is known as the IOD. Many studies have since shown that IOD is intrinsic to the Indian Ocean with a potential kick from the massive western Pacific convection center (Annamalai et al., 2003; Annamalai and Murtugudde, 2004; Saji et al., 2006; Wang et al., 2016; Wang and Wang, 2014).

Fig. 14a shows the east–west SST gradients from CORE-II simulations and results from CMIP5 simulations are shown in Fig. 14b. Observational estimates for mean SST in the eastern and western regions are 29.6 °C and 27.2 °C respectively (Fig. 14a). All models show a warm bias of up to 0.9 °C in the western equatorial Indian Ocean (45–60°E) (Fig. 14a). This sort of bias concentrated on the western equatorial IO would have implications for the modes of interannual variability. The observation shows a sharp gradient at 65°E and nearly

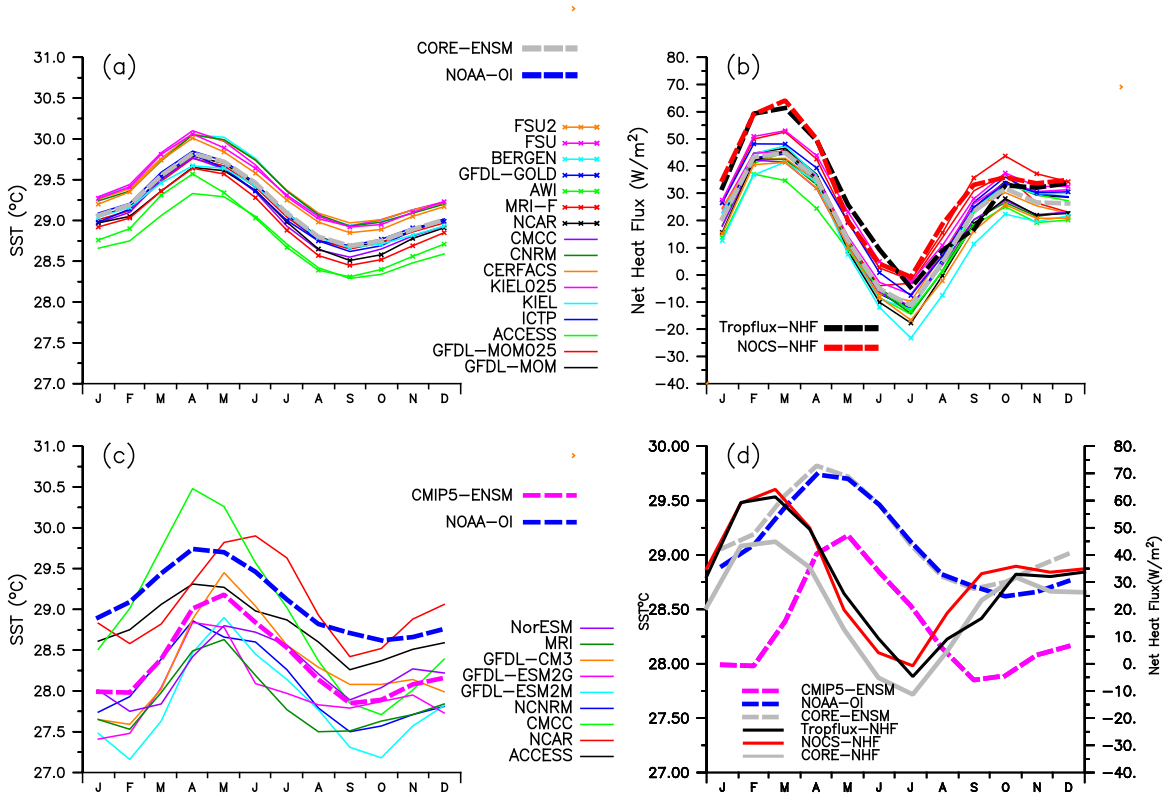


**Fig. 12.** Same as Fig. 10 but for the Eastern Equatorial Indian Ocean (EEIO).

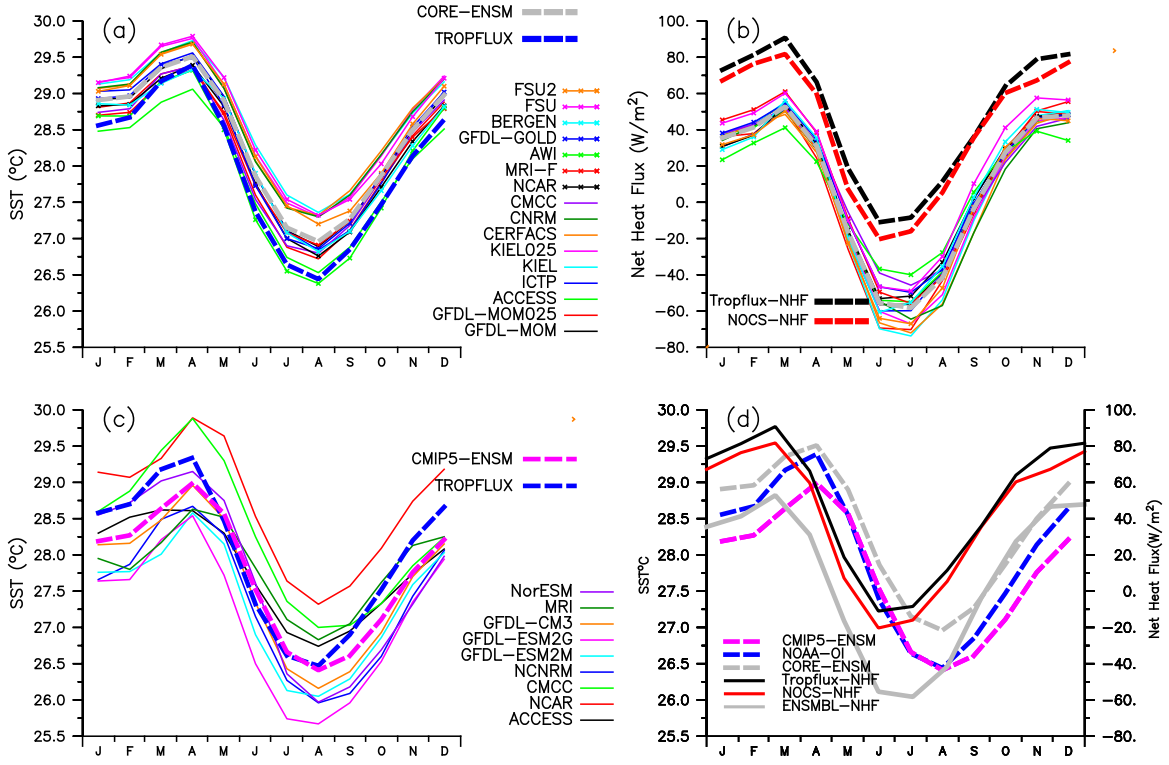


**Fig. 13.** Same as Fig. 10 but for the Thermocline Ridge (TR) region.

constant values of 29.3 °C in between 65–95 °E with a dip of 29.1 °C at 80 °E. All models show nearly constant SST between 65–95 °E with a spread of +/− 0.5 °C compared to observations. The KIEL group of models as well as FSU and FSU2 represent the upper estimates of SST along the equator, while AWI and ACCESS show a cold bias between 65–95°E providing the lower SST estimate of the ensemble. The CORE-II ensemble mean shows a general warm bias stronger evolved west of 65 °E. In contrast to the CORE-II forced simulations, most CMIP5

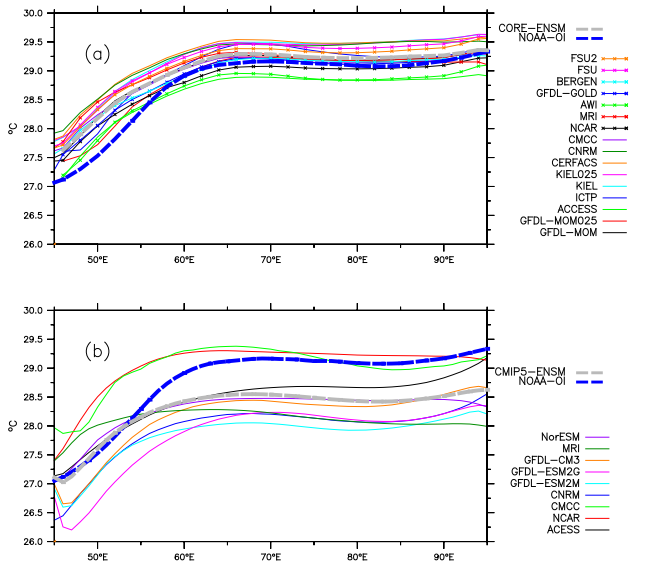


**Fig. 14.** Annual mean SST along the equator from (a) CORE-II models (b) CMIP5 models, their ensemble mean and NOAA-OI observations are also shown in thick gray and blue colors.

simulations show colder SST throughout the basin as well as a large model spread (Fig. 14b). Overall, CORE-II models show a higher skill in simulating zonal SST distribution along the equator than the CMIP5 models.

We summarize this analysis by noting that the seasonal variation of SST in different sub-regions in the Indian Ocean is well captured by the CORE-II models compared to the coupled CMIP5 simulations. In particular, the bi-modal SST variability over the AS, the BoB and the EEIO are well reproduced in CORE-II models, while the absolute climatological values differ regionally and seasonally by up to 1.8 °C, with a broad range of variations shown by the models. However, both CORE-II and CMIP5 models exhibit deficiencies in capturing the equatorial Indian Ocean dynamics, as evident from the flat zonal SST gradient and the warm bias over the open ocean upwelling dome south of the equator. The seasonal prediction skill for the tropical SST anomalies is a major predictability source for monsoon precipitation in the coupled models and is closely linked to the ability to simulate the SST mean state (Lee et al., 2010). We conjecture that the relatively poor skill of the coupled models at simulating the mean SST in the Indian Ocean versus the higher skill in the CORE-II simulations indicates the role for coupled feedbacks that amplify ocean biases. These results offer a useful benchmark for use in developing methods to reduce biases in coupled prediction models.

### 4.3. Surface salinity and barrier layer

In this section, we study the behavior of the surface salinity and associated BL within the Indian Ocean. Much of this behavior is affected by precipitation and river runoff forcing, with CORE-II simulations using interannually varying monthly mean precipitation derived from satellite corrected rainfall and interannually varying monthly mean river runoff (Dai et al., 2009; Danabasoglu et al., 2014). Additionally, as detailed in Griffies et al. (2009) and Danabasoglu et al. (2014), CORE-II simulations are integrated with surface salinity restoring in order to reduce long-term drifts in the thermohaline properties of the models. Details are given in Section 3.1. The monthly climatology is computed over the period 1982 to 2007 for all models.

#### 4.3.1. Surface salinity

Fig. 15 shows the annual mean SSS from the CORE-II models and their biases with respect to observation. Fig. 15a shows the SSS from WOA observation, Fig. 15b shows the ensemble mean from all models and Fig. 15c shows the ensemble bias. Asymmetry in the SSS distribution with higher salinity in the AS and lower salinity in the BoB is seen in the observation and is reproduced by all simulations. However, all models show a basin wide positive salinity bias with large values over the northern BoB and the SEAS. Interestingly, the biases are much smaller along the observed salinity fronts aligned towards Madagascar Island from Sumatra. Some models, such as CNRM, CMCC, AWI and BERGEN, even show lower salinity along this path. Due to this opposite sign of the bias, the basin averaged salinity bias is much weaker in these models. Both FSU models show a basin wide bias of 0.44 and 0.48 psu, which is much larger than the ensemble mean bias (0.16 psu) as well as the bias in other models. The annual mean basin averaged salinity from WOA observation is 34.77 psu and over the northern BoB it reaches down to 32.12 psu due to the strong influence of river runoff.

In the northern BoB, the mean SSS bias in the individual models ranges between 0.3 and 0.5 psu with higher values in FSU and FSU2 (2.1 and 1.8 psu, respectively). The slight improvement in FSU2 may be due to an improvement in model physics. The low-salinity water flowing out of the BoB along its eastern boundary (Shetye et al., 1996; Han and McCreary, 2001; Jensen, 2001; Sengupta et al., 2006) crosses the basin with the SEC and reaches the western Indian Ocean to Madagascar. The observed low salinity band south of the equator between 5°S and 20°S is well reproduced in all models. This low salinity region also corresponds to the region of Inter Tropical Convergence Zone (ITCZ) associated with locally large precipitation (Yu, 2011; Perigaud et al., 2003). The annual SSS bias is only 0.11 psu over the entire basin in GFDL-GOLD (Fig. 15p). KIEL shows a large positive bias over the BoB. ACCESS, GFDL-MOM and NCAR show a large positive bias over the eastern AS. A positive bias over the SEAS can be attributed to the inability of these models to transport low salinity water by the EICC. This behavior can be seen in the depth versus time plots of salinity over this region as well (see Fig. 22a and Section 4.4.2). SSS simulations improve significantly upon refining the model's horizontal resolution (KIEL025, GFDL-MOM025) as compared to their coarser counterpart. Han et al. (2001) reported that advection of salinity by a coastal current plays an essential role in the salinity balance. This may be the reason for better salinity simulation in a higher resolution model. This result contrasts the SST results (Fig. 5), which revealed only minor sensitivity to the changes in horizontal grid resolution.

Unlike SST, spatial structure of annual mean SSS and its bias are roughly symmetric across all seasons. However, different regions differ in seasonal SSS variations (Fig. 16). The minimum surface salinity over the NIO is seen in October over the north BoB (Fig. 16b; Rao and Sivakumar, 2003; Sengupta et al., 2006). FSU and FSU2 seasonal cycles are outliers with a systematic positive bias of ~1 psu in the BoB (Fig. 16b) and in the other regions as well with slight reduction in bias. As in the case of SST, SSS also shows large inter-model spread. In the BoB, only CMCC is able to capture the seasonal cycle with lowest observed salinity in October (Fig. 16b). Peak river runoff and the integrated summer rainfall lead to a SSS minimum in October. EEIO shows two salinity lows during the inter-monsoon months of March–April and October–November in the seasonal SSS variations (Fig. 16c). These lows are associated with precipitation due to ITCZ seasonality over this region. The models are able to capture this semi-annual signal, but with varying biases and large inter-model spread. SSS does not change significantly over the SIO on seasonal time scales (Fig. 16e). It is almost constant in WOA at 35 psu and the models are able to capture this near constant SSS throughout the year. Almost all models show a positive salinity bias in the AS, the BoB and the SEAS (Fig. 16a, b, f), but in FSU and FSU2 this bias is seen in all the sub-regions.

In summary, the CORE-II SSS shows good representation of the asymmetric salinity pattern in the Indian Ocean, with high salinity

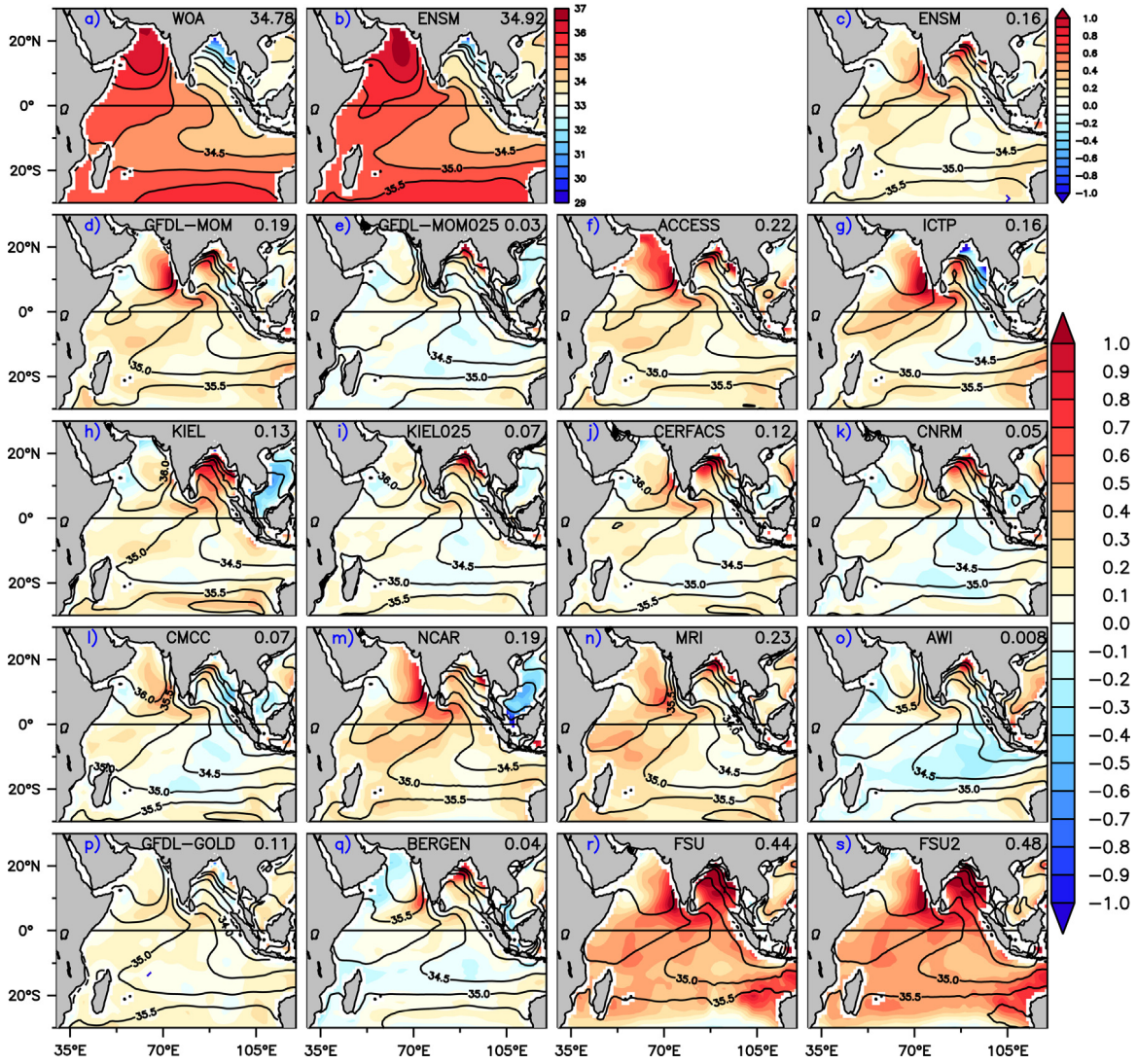


**Fig. 15.** Annual mean SSS bias (model minus observation) from CORE-II simulations (color shade) with contours for the annual mean (d-s). The model ensemble mean bias is shown in the upper right panel (c). Observed annual mean SSS from WOA is shown in the upper left panel (a). Ensemble mean from all CORE-II models is shown in the upper middle panel (b). Contour levels for WOA and all models are same. Units are in practical salinity. Basin averaged SSS values from WOA observation, ensemble mean as well as basin averaged bias of individual models are shown in upper right corner of each panel.

water in the AS and low salinity water in the BoB. Most of the models underestimate the freshening in the northern BoB, with improvement seen in high resolution eddy permitting models.

### 4.3.2. Barrier layer and its impact on SST bias

The time varying depth of the mixed layer is a crucial parameter for the mixed layer heat budget and hence for the SST (Chen et al., 1994; Qiu et al., 2004). Challenges of ocean models is to simulate this time varying MLD over global and regional oceans. In the Indian Ocean, the upper ocean stratification in temperature and salinity does not necessarily coincide. Depending upon the freshwater input, it differs particularly over the BoB, the EEIO and the SEAS (Thadathil et al., 2007; Sprintall and Tomczak, 1992). Owing to its unique geographical location, the BoB receives large amount of freshwater both from local precipitation and river discharge, estimated at about 4700 and 3000 $km^3$/yr, respectively (Sengupta et al., 2006). Annual freshwater input exceeds evaporation and hence it makes the BoB relatively fresh compared to the rest of the basin. This low saline water is confined within a thin layer near the surface and makes the top of the halocline shallower than the top of the thermocline. This unique structure makes the mixed layer limited by the top of halocline and an isothermal layer depth (ILD) limited by top of the thermocline. The difference of these two layers is called a BL (Thadathil et al., 2007; Sprintall and Tomczak, 1992). BL also forms over the SEAS and the EEIO. This layer inhibits vertical mixing and hence restricts entrainment cooling from the thermocline and affects the mixed layer heat budget and SST variations. Observational studies show that on a seasonal scale this layer thickness is ~10–60 m (deBoyer Montégutet et al., 2007; Thadathil et al., 2007). It has been shown in these studies that BL formation potentially plays a significant role in mixed layer heating. In this section, we assess the BL from all the simulations and its effect on SST. The ILD and MLD are computed based on Kara et al. (2000) corresponding to temperature change of 1 °C at the surface.

The annual mean BL from all model simulations and WOA is shown in Fig. 17. Sprintall and Tomczak (1992) show that three regions (EEIO, north BoB and SEAS) consistently display a significant BL of 10–50 m thickness throughout the year. There is a BL in the north BoB (Vinayachandran et al., 2002; Thadathil et al., 2007; deBoyer Montégutet et al., 2007) due to inflow of freshwater from adjoining rivers and local precipitation during the Indian summer monsoon, thus making the mixed layer very thin (~10–20 m) and in turn thickens the BL (Fig. 17). The observed annual mean BL over the northeastern BoB is ~40–44 m (Fig. 17). The northwestern BoB shows slightly thinner BL, mainly since the western BoB experiences a regime of excess

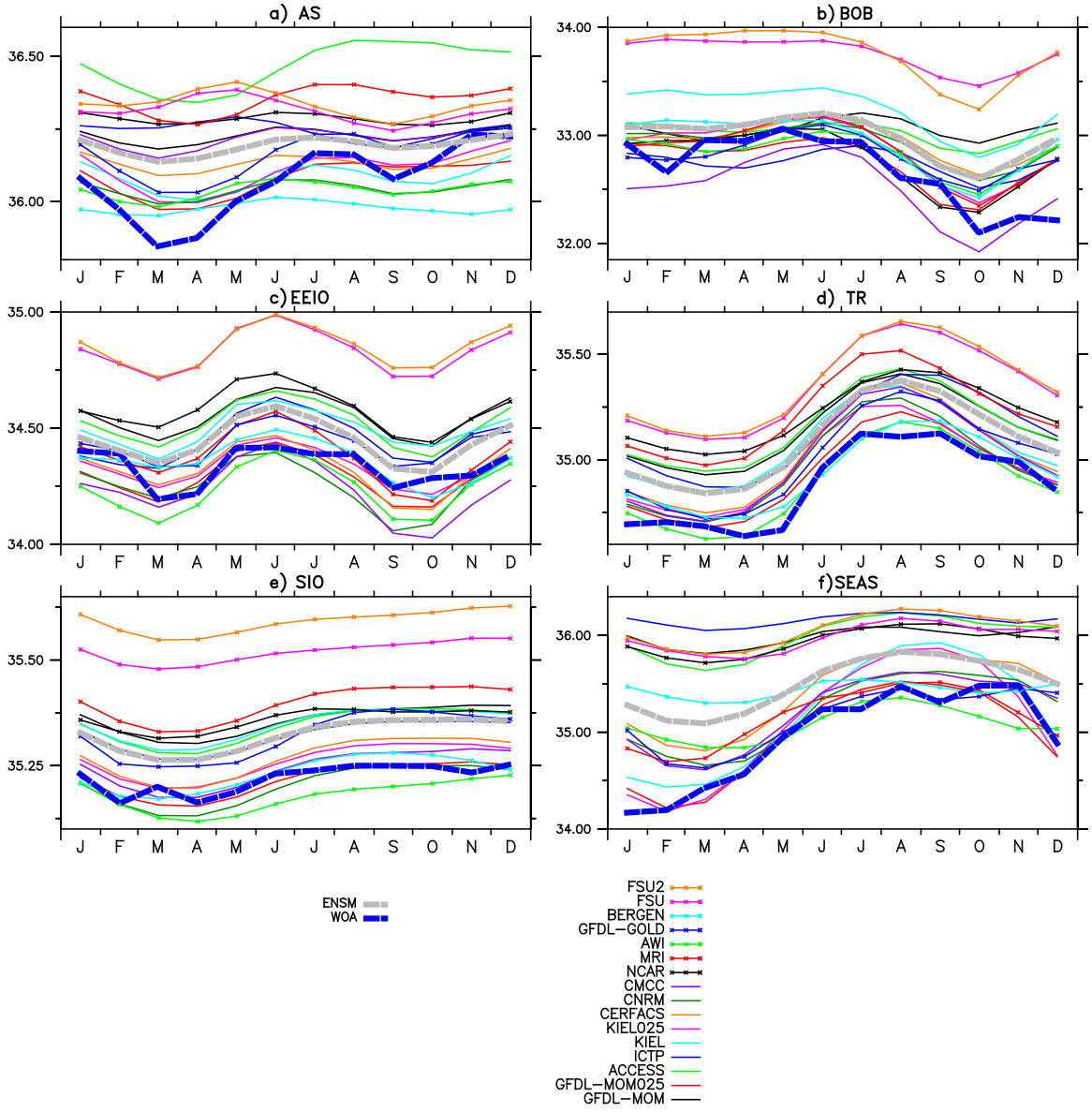


**Fig. 16.** Seasonal cycle of sea surface salinity from all CORE-II models and WOA observation over different sub-regions of the Indian Ocean (see Section 3.4 for sub-regional specifications).

evaporation as compared to the eastern BoB (Sprintall and Tomczak, 1992; Pokhrel et al., 2012b). The BL in the western BoB is maintained by the river runoff received during summer monsoon (Vinayachandran et al., 2002; Sengupta et al., 2006). The east–west difference in BL over BoB is most prominently simulated by KIEL and KIEL025. Other models are unable to capture this east–west gradient.

To see how the models simulate the seasonal variation of the BL, we show the time series of the BL averaged over the BoB, the SEAS and the EEIO in Fig. 18. Observation shows that the seasonality in the BL becomes most prominent over the BoB during December–January when it becomes ~40 m thick (Fig. 18a) and is mainly driven by substantial river runoff into the north BoB. Most of the models are unable to capture this winter time thick BL in the northern BoB, though the NEMO group of models (KIEL at both resolutions, CERFACS, CNRM and CMCC) do a reasonable job with KIEL025 and CERFACS have BL slightly thicker than observed value. MOM and HYCOM class of models are unable to capture this BL. Notably, horizontal refinement of grid resolution (e.g., MOM025) improves the BL simulations (Fig. 30b). We conjecture that the inability of the MOM class of models to simulate the observed BL, in contrast to the NEMO class, arises from differences in boundary layer parameterizations.

The second region with a prominent BL occurs over the EEIO west of Sumatra. Observation shows an annual mean BL thickness of ~20–25 m with seasonality and peaks during November–December with a BL thickness of 30 m. KIEL025 and CERFACS capture the observed mean and seasonality (Fig. 18b). The remaining NEMO models also capture this annual mean and seasonality with reasonable accuracy. The remaining models underestimate the BL. FSU and FSU2 models underestimate the BL by ~10 m, and during the peak season (November–December) it is doubled (20 m). The presence of a BL throughout the year is due to the local maximum in P-E present throughout the year (Oberhuber, 1988).

The SEAS is the third region where BL is prominent. Observation shows a thick BL (~30 m) over the SEAS (Fig. 18c). Once again, the NEMO class of models performs better than the other models. The other class of z-coordinate models based on MOM (MOM, MOM025, ICTP, and ACCESS) and NCAR as well as the isopycnal model BERGEN provide a reasonable simulation of the location and amplitude of the BL. In the hybrid vertical coordinate model FSU and FSU2, BL amplitude is

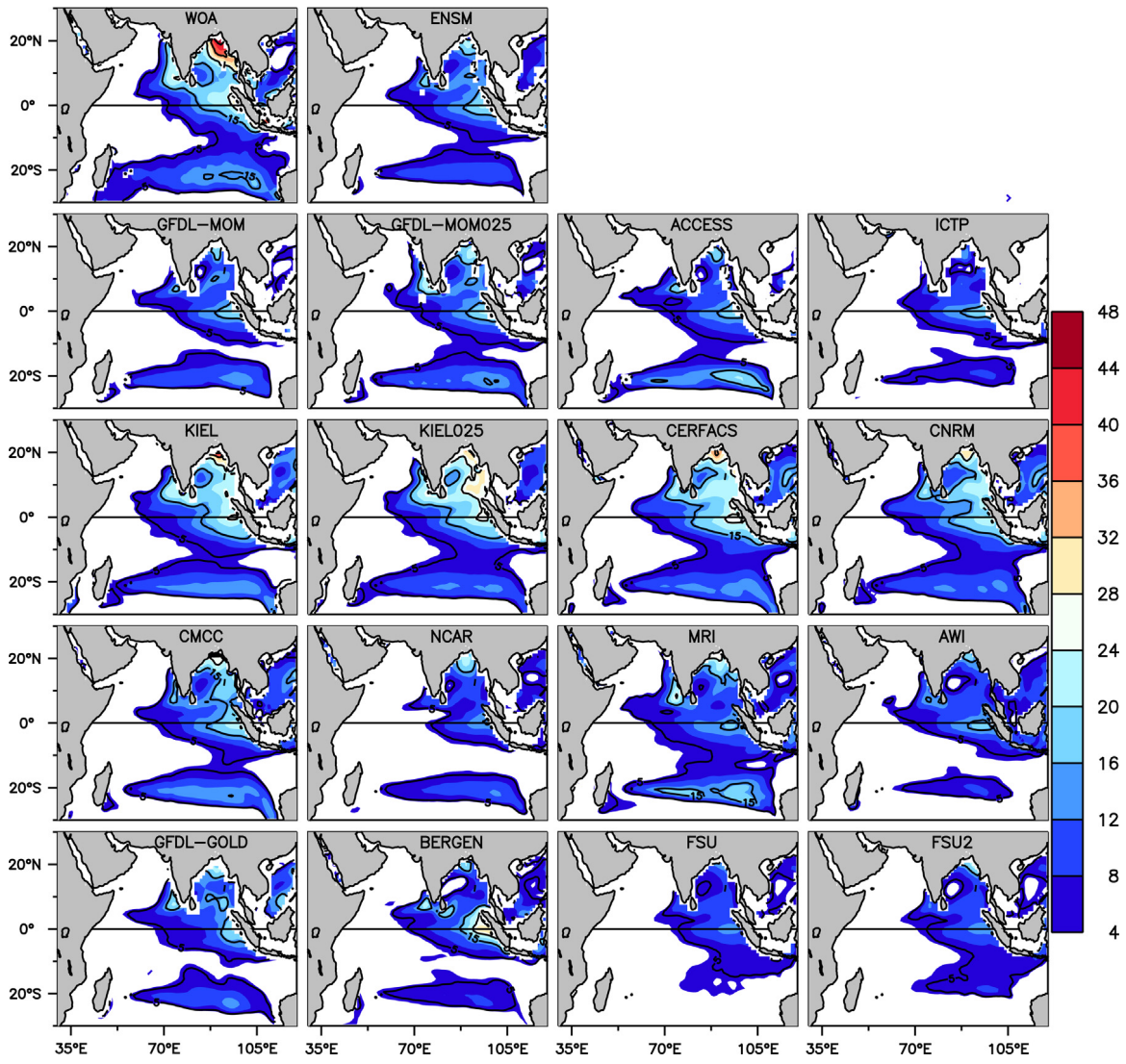


**Fig. 17.** Annual mean barrier layer thicknesses (BL) in meters from CORE-II simulations and WOA observation. The observed annual mean BL from WOA is shown in upper left panel. The ensemble means BL from all simulations is shown in the upper middle panel. The individual model performances are shown in other panels.

largely underestimated as compared to WOA observation. The seasonal cycle of the BL shows that the BL is maximum in January–February (~50 m) and then gradually decreases and is almost annihilated in April (Shenoi et al., 2004) (Fig. 18c). Large spread (10–55 m) is seen among the models in simulating the peak BL during January–February. The superiority of the NEMO model class in reproducing the seasonal cycle of BL can be seen with KIEL025, which is able to capture the peak magnitudes with slight overestimation. Although the MOM simulations are unable to reach the highest value for the BL thickness, the increased resolution clearly improves the peak magnitude. FSU and FSU2 are notably poor in reproducing the seasonal cycle. The inability of reproducing the BL is mainly due to the inability to bring the low salinity water from the north BoB by the EICC during November–January (Shankar et al., 2002; Rao and Sivakumar, 2003), as explained in Section 4.3.1.

### 4.4. Subsurface features

#### 4.4.1. Subsurface temperature

The spatial distribution of subsurface temperatures in the tropical Indian Ocean has distinct regional characteristics (Colborn, 1975). It is well documented that all climate models tend to render a diffuse thermocline with mostly deeper than observed thermocline (Cai and Cowan, 2013; Tao et al., 2015; Flato et al., 2013). The models' ability to simulate the temporal and spatial variability, particularly on a seasonal timescale, determines how well the model performs in terms of monsoon strength and variability. It has been reported in IPCC-AR5 (Stocker et al., 2013) that the thermocline biases in CMIP5 have not improved much despite the increase in resolution compared to CMIP3 (IPCC AR4) (Cai and Cowan, 2013; Tao et al., 2015; Flato et al., 2013). It is important in this context to investigate how the CORE-II simulations, perform in simulating subsurface dynamics and thermodynamics.

The average thermocline depth in the NIO is about 100 m (Rao and Sivakumar, 2000; Yokoi et al., 2008, 2009). We thus take 100 m as a reference depth, with Fig. 19 showing the 100 m temperature bias from models relative to WOA. The WOA shows three distinct warm regions over the AS, the EEIO, and along 25 °S–10 °S in the south Indian Ocean. The relatively cooler region over the thermocline ridge corresponds to the open ocean upwelling region (Xie et al., 2002; Schott et al., 2009). Similar to the SST distribution, all models show a warm bias over this region as well as the western equatorial Indian Ocean, with ICTP and BERGEN showing the largest bias (>3 °C) and CMCC and GFDL-GOLD showing the smallest in these regions. The basin averaged bias is largest in BERGEN (2.4 °C) followed by ICTP (2.1 °C), whereas GFDL-GOLD shows a negligible bias of 0.1 °C. The refined resolution reduces the bias especially in GFDL-MOM025. Among the

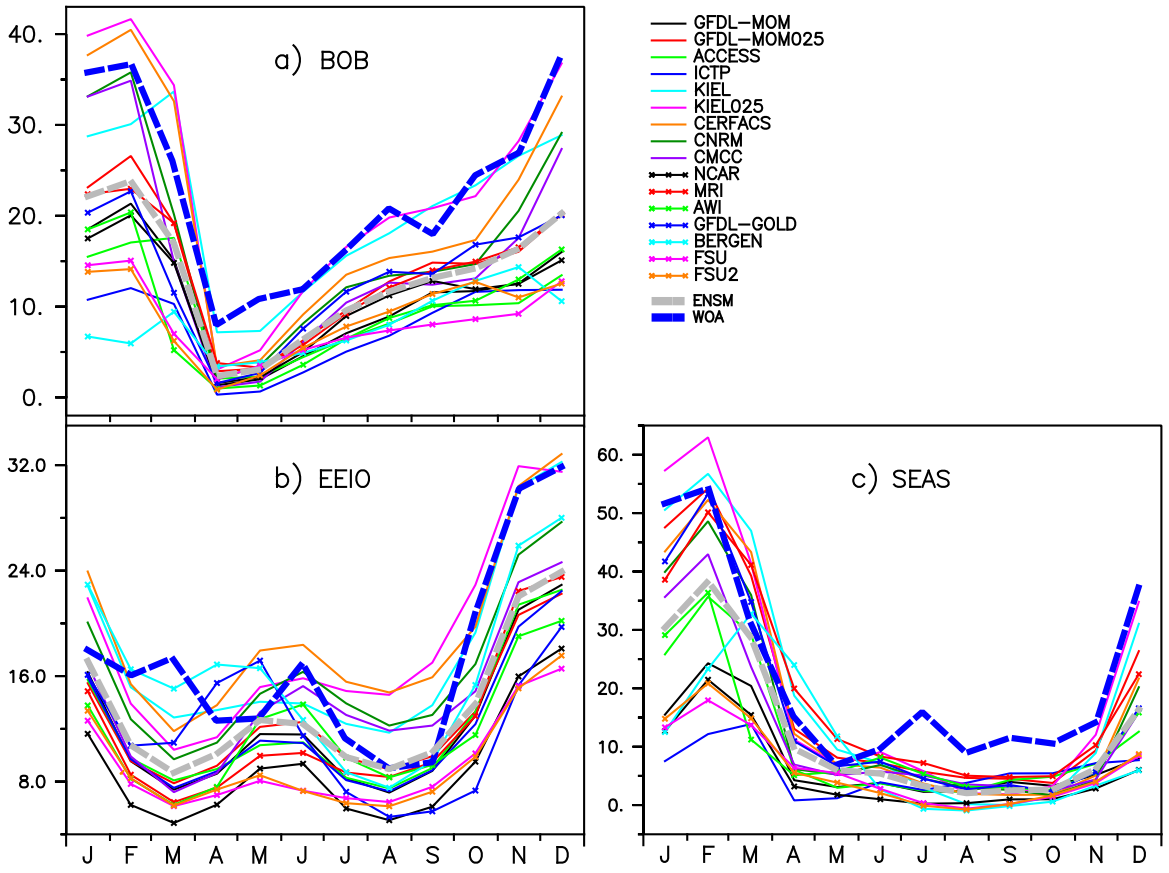


**Fig. 18.** Seasonal cycle of Barrier Layer Thickness over (a) Bay of Bengal, (b) Eastern Equatorial Indian Ocean, and (c) South Eastern Arabian Sea from all CORE-II model simulations and WOA observation.

NEMO group of models, CMCC performed best with a basin averaged bias of 0.49 °C. Interestingly, both the isopycal (BERGEN) and hybrid class of models (FSU, FSU2) show larger biases than the z-coordinate models. This result indicates a common weakness of these models in the representation and/or parameterization of near surface physical processes.

To see how the models capture the seasonal cycle of subsurface temperature, we plot the depth versus time mean temperature and the corresponding bias over different regions. The vertical levels of all models are regrided to MOM depth levels. Fig. 20a shows the upper ocean seasonal evolution of temperature from WOA observation, 16 CORE-II model simulations and its ensemble mean in the AS. The biases of individual models are also shown in shade with mean values represented in contours. The warm surface temperature seen in April–May (Fig. 20a) penetrates down to 40 m with values similar to the surface (~30 °C) in the WOA observation, which is well represented by the CORE-II ensemble mean. The upper ocean (0–100 m) is warmer throughout the year with maximum of 30 °C right at the surface during April/May, but decreasing to 26 °C near 40 m. Below 100 m, temperature changes sharply and reaching ~11 °C at 500 m depth. The ensemble mean temperature variation is close to observed values. The ensemble mean bias in the thermocline depth and below (100–300 m) shows much lower values (~1 °C) compared to many individual models, thus indicating a non-unidirectional bias of the models. The MOM group of models (GFDL-MOM, GFDL-MOM025, ICTP and ACCESS) shows a large bias in the thermocline with a range between 1–3 °C, with the highest bias in the coarsest model ICTP. Among all models, MRI shows the maximum bias of ~4–5 °C in the thermocline region. In the AS for the NEMO group of models (KIEL, KIEL025, CERFACS, CNRM and CMCC), the bias in the thermocline region (100–200 m) is much less (~1 – 1.5 °C) with almost negligible bias in CNRM. However, these biases are increased in the BoB and the EEIO (Fig. 20b,c). In contrast, the deeper layers (below 250 m) are much cooler (~1.5 °C) in GFDL-GOLD, FSU and FSU2 in the AS (Fig. 20a) and this bias reduces in the BoB and the EEIO (Fig. 20b,c). These biases cancel each other out such that the model ensemble mean resembles the observations. In BERGEN, the thermocline shows a positive bias in the AS, whereas it shows a negative bias in the BoB. But, it is much narrower relative to the MOM group of models (MOM, MOM025, ICTP and ACCESS), which shows a broader and more diffuse thermocline. Increased horizontal grid resolution does not show any significant change in the thermocline bias with slight increases in the thermocline bias for both GFDL-MOM025 and KIEL025 as compared to their coarser resolution counterparts (Fig. 20a,b,c). This behavior suggests that these models are producing enhanced spurious mixing due to numerical truncation errors (Griffies et al., 2000; Ilıcak et al., 2012). All models show a cold and warm bias within 1 °C in the upper ocean (0–100 m), except AWI which shows a cold bias (~1–2 °C) in the BoB Fig. 20b. The thermocline continues to be diffuse and warmer for all models except GFDL-GOLD and BERGEN, which are cooler than WOA.

In the EEIO, observations show a stronger seasonal cycle of temperature down to 500 m depth, which is absent in other regions of the tropical IO (Fig. 20c). All the models show a warm thermocline bias with ICTP and MRI showing the largest bias (~3–4 °C). Also note that the thermocline bias is largest in the EEIO as compared to AS and BoB. GFDL-GOLD is an exception among all models in all regions, with this model showing a cold thermocline bias with magnitude range of 0.5–1 °C. The positive subsurface bias is largest over the EEIO as compared to the AS and the BoB. The isotherms show a semi-annual signal with peaks in May and November that penetrate down to 500 m depth, which is in general present in all the models shown here. This deep penetration of seasonal variation in the isotherms is due

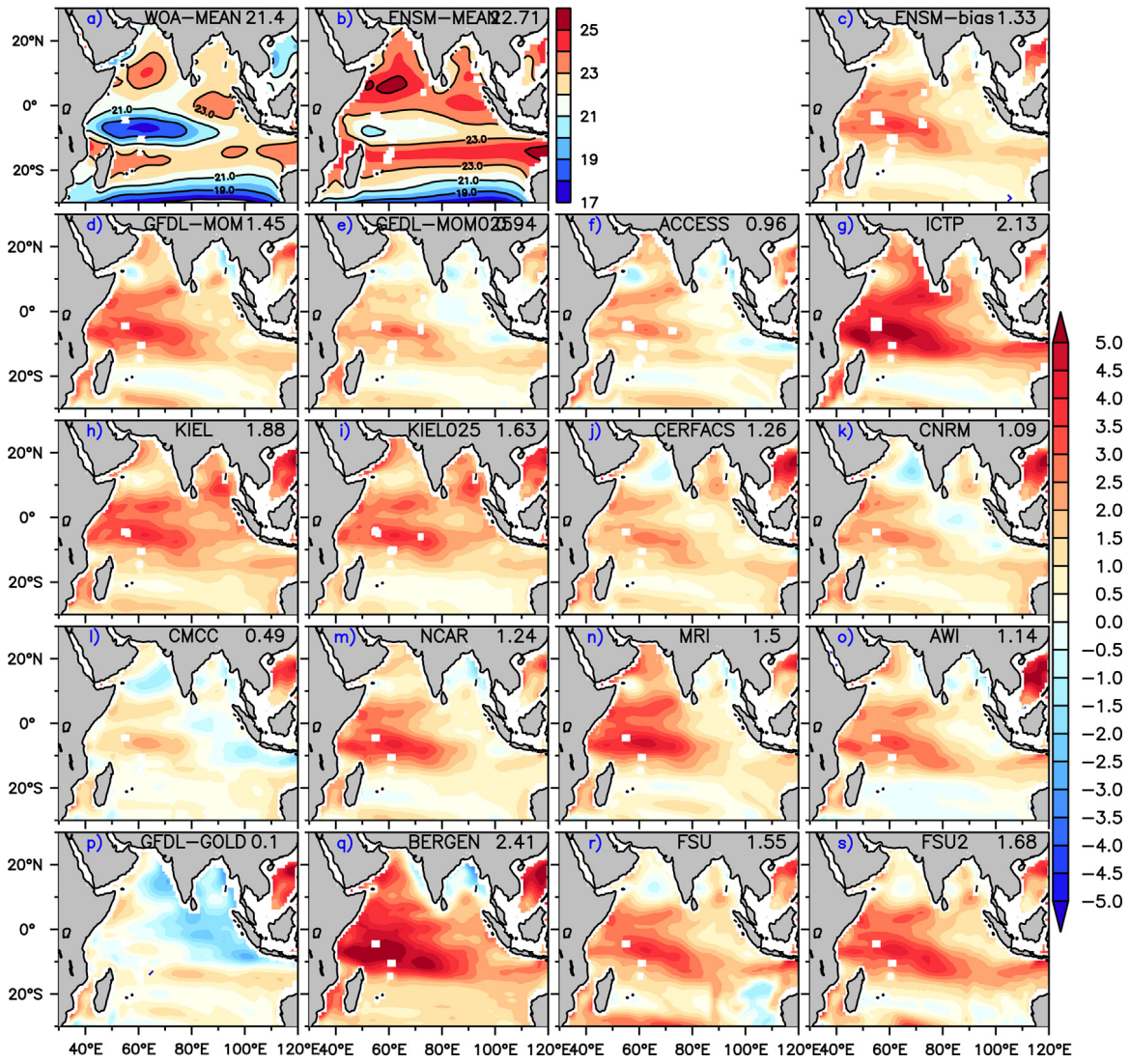


**Fig. 19.** The upper left panel shows the temperature (degrees Celsius) at 100 m depth from WOA (a); the upper middle panel shows the same from the CORE-II ensemble (b) and the upper right panel shows the ensemble bias at 100 m depth with respect to WOA (c). The remaining panels show the temperature bias (model minus observation) at 100 m depth from all CORE-II individual models (d-s). The basin averaged values are given in upper right corner of each panel.

to the convergence of warm water from the western Indian Ocean to the eastern Indian Ocean associated with the spring and autumn WJ (Webster et al., 1999; Rao and Sivakumar, 2000). The equatorial downwelling Kelvin waves generated in May–June and November propagate eastward and deepen the thermocline in the region off Sumatra (Du et al., 2005). The warm layer of 30 °C appears in February and gradually reaches a deeper layer in May and then again cooling down to 29 °C in June. This near surface observed structure is well captured by the ensemble simulation. The observed vertical temperature gradients are well captured in GFDL-GOLD. The EEIO shows a mixed response to refinement in grid resolution, with a slight bias reduction over the thermocline region but degradation below the seasonal thermocline. The ensemble mean variation closely followed the WOA but with a warm bias almost throughout the upper ocean with highest values in the thermocline region (Fig. 20c).

### 4.4.2. *Subsurface salinity*

Salinity stratification is mainly driven by the precipitation, evaporation and freshwater through river runoff and by the horizontal advection which also play an important role (Sprintall and Tomczak, 1992). In the NIO, near-surface haline stratification indirectly influences the evolution of the mixed-layer temperature by inhibiting the entrainment of subsurface cooler water (Moshonkin and Harenduprakash, 1991; Rao and Sanil Kumar, 1991; Rao et al., 1991; Rao and Sivakumar, 2003; Howden and Murtugudde, 2001; Shenoi et al., 2002, 2004; Miller, 1976). Many modeling studies have also shown that salinity plays an important role in the evolution of SST through MLD variations in the tropical Indian Ocean (Cooper, 1988; Masson et al., 2002, 2005; Sharma et al., 2007, 2010; Durand et al., 2011; Fathrio et al., 2017b). These results motivate us to examine the vertical salinity gradients in the tropical Indian Ocean, with the vertical difference of salinity between surface and 100 m shown in Fig. 21.

The WOA shows three regions with strong haline stratification (>1.4 psu), namely: BoB, EEIO and SEAS. The strong vertical salinity differences are noticed primarily in the northern BoB. The observed difference is more than 3 psu over the northern BoB. The MOM group of models (GFDL-MOM, GFDL-MOM025, ACCESS and ICTP) and the NEMO class (KIEL, KIEL025, CERFACS, CNRM and CMCC) show their strongest stratification there as compared to WOA. The stratification is rather weak over the BoB in AWI, BERGEN, FSU and FSU2 as compared to WOA.

Rao (2015) has shown that within the Indian Ocean warm pool, near surface haline stratification exist over the SEAS, the southwestern BoB and the EEIO. They also reported that a strong coupling between

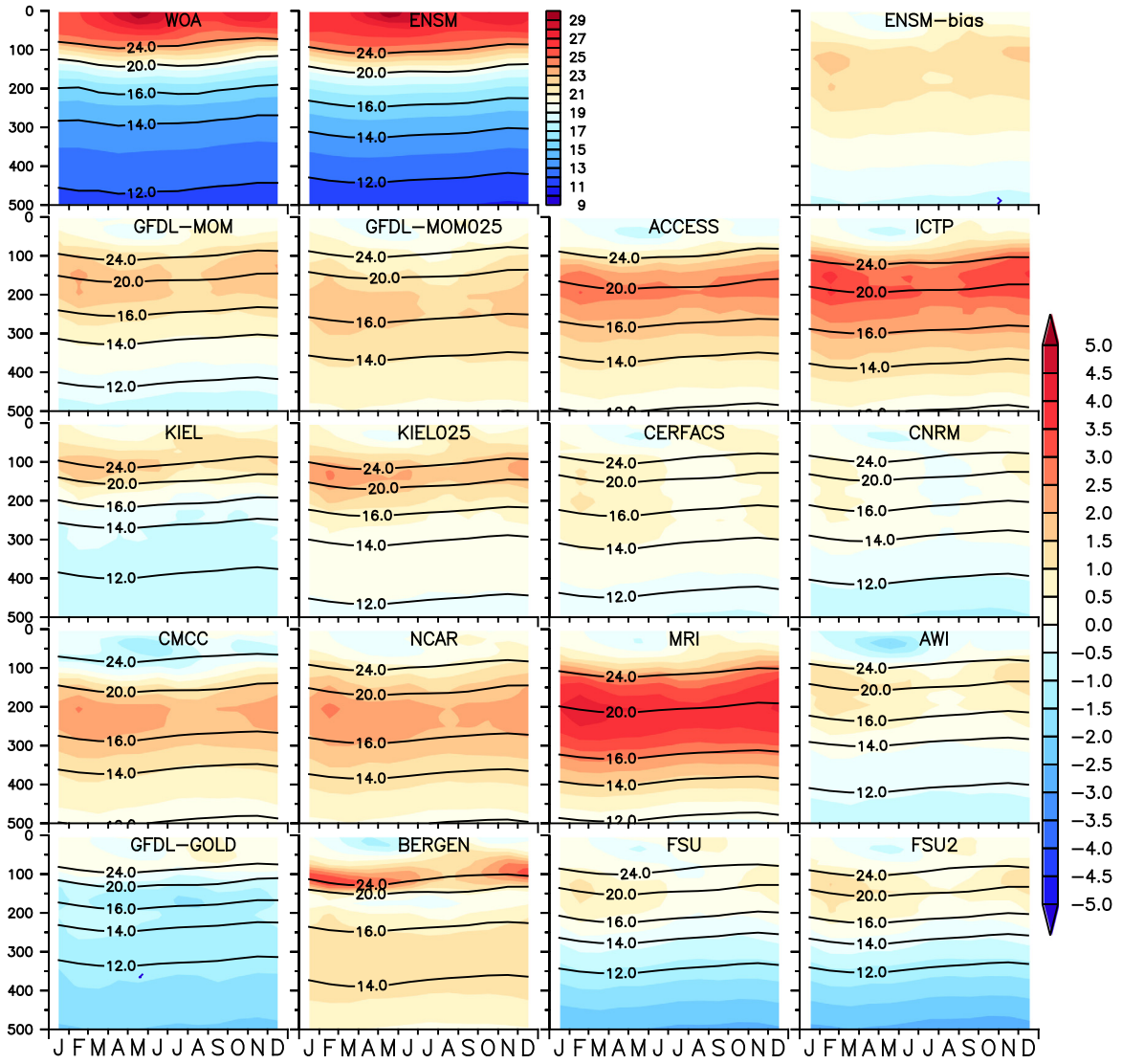


**Fig. 20a.** Seasonal variation of mean temperature (degrees Celsius) as a function of depth averaged over the Arabian Sea (contour) and its bias (model minus observation) in color. The upper left panel shows the mean seasonal variation of temperature from WOA observation and the upper middle panel shows the mean seasonal variation of temperature from the ensemble mean and the upper right panel shows the ensemble mean bias with respect to WOA. Contour levels for WOA observation, all individual models and its ensemble mean are same.

near surface salinity stratification and the subsequent evolution of warm pool core is most prominently seen over the SEAS. The near-surface vertical salinity stratification over the SEAS is instrumental for the mini-warm pool in the AS (Durand et al., 2004), which is influenced by the advection of low salinity waters from the BoB during November–February (Rao et al., 2015). Hence, it is of particular interest to determine how the CORE-II models capture this stratification.

Since salinity stratification mostly modulates the upper ocean temperature, we show the seasonal evolutions of salinity with depth over the SEAS, the BOB and the EEIO. The vertical levels of all models are regrided to MOM depth levels. Fig. 22a shows the seasonal evolution of salinity with depth over the SEAS. The freshening in the upper ocean (0–50 m) during December–February is very prominent in the WOA observation. This freshening is reasonably reproduced by all models, but most prominently by KIEL, KIEL025 and MOM025. Below this fresh water, there is an intrusion of saltier water present throughout the year with peak values in October–November at about 50 m depth. This intrusion of saltier water is from AS high salinity water (ASHSW), as well as salty waters from the Red Sea and Persian Gulf (Shenoi et al., 1999, 1993, 2005; Levitus, 1983; Shetye et al., 1994; Durgadoo et al., 2017).

Below this saltier layer there is fresher water seen in WOA, with a minimum at 200 m depth, which can also be seen in Fig. 23c. Note that individual profiles based observations also show this structure (Shankar et al., 2005; Shenoi et al., 2005). The upper ocean is saltier during December–February in all simulations, with salinity larger than 1.2 psu in GFDL-MOM, ACCESS, ICTP, NCAR, BERGEN, FSU and FSU2. Aside from BERGEN, these models also show a saltier thermocline region compared to observations, as well as an increased salinity down to 300 m depth. Within the MOM models, ICTP and GFDL-MOM are unable to capture the winter time upper ocean freshening. A refinement of the horizontal resolution (MOM025) improves the simulation and allows the model to capture these low salinity values. Among all the models, BERGEN shows the freshest thermocline in contrast to a positive salinity bias for the thermocline in other models (Fig. 22a). The CORE-II ensemble mean variation captures the overall observed vertical structure, but with a positive salinity bias with largest value in the thermocline. The ensemble mean is also unable to resolve the local minimum in salinity below.

Fig. 22b shows the seasonal cycle of vertical salinity over the BoB. The upper ocean (0–100 m) is much fresher ~33–34 psu in observations than in the SEAS due to the proximity of large freshwater input by

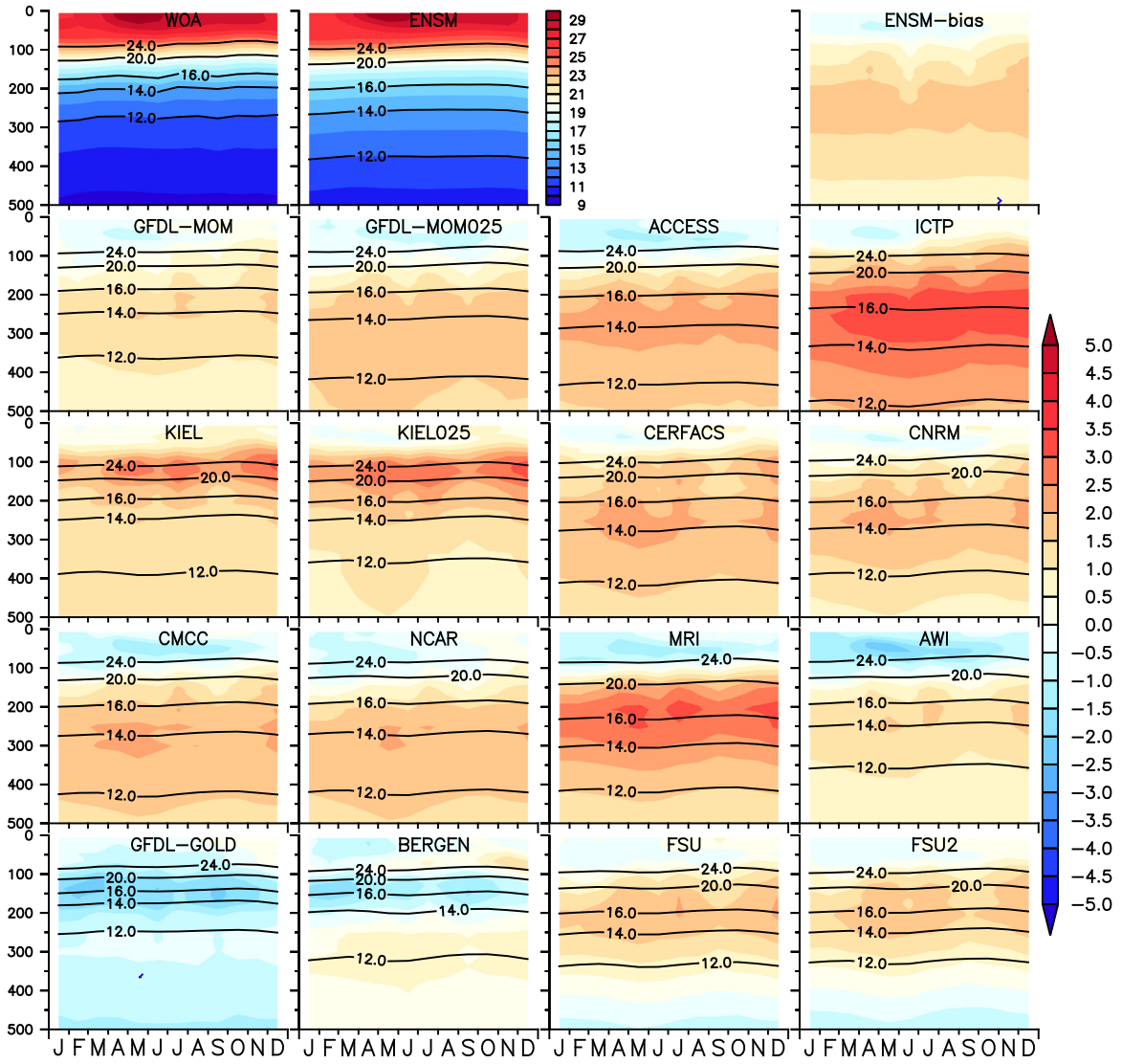


**Fig. 20b.** Same as Fig. 20a but for the Bay of Bengal.

river runoff. MRI shows the smallest biases over depth and the seasonal cycle. Most models show an upper ocean (0–100 m) fresh bias, except FSU and FSU2 which show a much saltier upper ocean. There is a rather large positive salinity biased thermocline in KIEL, KIEL025, CERFACS, CNRM, CMCC, FSU and FSU2, whereas BERGEN shows a much fresher thermocline as compared to WOA (Fig. 22b). The remaining models show a slightly saltier (~0.3 psu) thermocline. In the EEIO region (Fig. 22c) we see a fresh surface layer (0–100 m), which is mostly captured by all models except FSU and FSU2. Below 100 m, salinity shows only weak variation in observations, remaining nearly constant at 35 psu. However, the simulations show a spread with a positive salinity bias in the upper thermocline and fresh bias in the deeper ocean (also see Fig. 23d).

Fig. 23 shows the annual mean vertical salinity variations from WOA and CORE-II simulations averaged over different regions. The vertical salinity distribution shows distinct variations in the western Indian Ocean (AS, SEAS, TR) as compared to the eastern Indian Ocean (BoB and EEIO). Over the BoB and the EEIO, higher precipitation reduces surface salinity compared to the western basin, where evaporation dominates precipitation (Pokhrel et al., 2012b) thus leading to a saltier surface layer there. The observations show that in the AS the high surface salinity decreases rapidly with depth to 200 m then the observed salinity decrease is small, almost stable up to 800 m depth, while deeper a stronger freshening occurs again. All simulations show saltier upper ocean, except for BERGEN and AWI, which show a fresh bias. Below 200 m all models reproduce a fresh subsurface layer. Salinities in FSU and FSU2 are the freshest of all simulations.

This low salinity could be due to the unrealistic exchange of salty water from the Red Sea and Persian Gulf in these models (Legg et al., 2009; Durgadoo et al., 2017). In the BoB, the halocline is represented by a strong gradient over the upper 100 m, which is captured by almost all models, except for BERGEN, which shows a negative salinity bias. Observations also show a local maximum in salinity around 200–400 m depth, which is connected to the intrusion of high saline ASHSW, Red Sea Water (RSW) and Persian Gulf Water (PGW) (Rochford, 1964; Varadachari et al., 1968; Sastry et al., 1985; Vipin et al., 2015). All models capture this subsurface salinity maximum except for BERGEN. Below 400 m, FSU and FSU2 show a much fresher layer as compared to WOA observation.

Vertical salinity variations in the SEAS show a saltier layer at 50 m depth with a fresh layer above and below. As already seen in the AS, in the SEAS models overestimate the surface and subsurface salinity, with only BERGEN showing a clear local minimum between 100 m and 200 m depth. Below 600 m, all models are fresher than the observations. In the TR region, the presence of ASHSW increases subsurface salinity at 100–200 m depth. Although all models overestimate salinity in the upper 400 m, they capture this increased salinity signature from

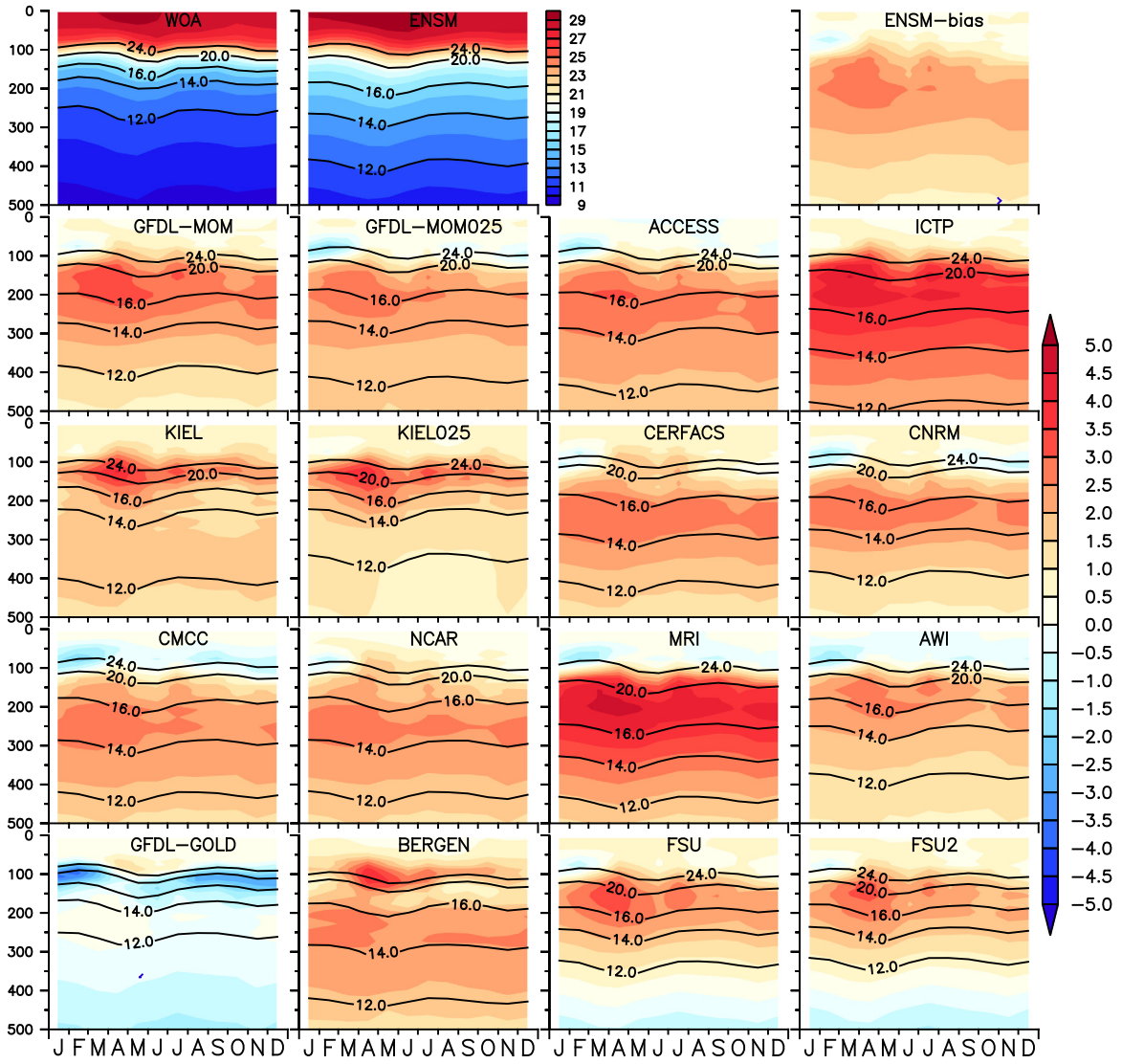


**Fig. 20c.** Same as Fig. 20a but for the Eastern Equatorial Indian Ocean.

ASHSW and finally end with a rather constant salinity over depth below 1000 m, as seen in observations already further up in the water column.

In the SIO, a high saline subsurface layer exists at 200–400 m depth. This salty layer is formed due to the presence of Indian Ocean Central Water. The excess evaporation over precipitation forms high salinity surface water (>35 psu) between 35 °S and 25 °S, winter convection and downward fluxes of salt and heat causes the subtropical water to extend with salinity above 35 psu to a depth of about 500 m (Wyrtki, 1973). The subsurface salinity maximum in the south Indian Ocean spreads towards the north and is carried by the South Equatorial Current and reduces the thickness of the central water mass to 300 m at 20 °S and 100 m at 10 °S. The subsurface salinity maximum is at ~250 m depth, in which salinity can exceed 35.6 psu as reported by Warren (1981). This feature is most strongly developed in the central Indian Ocean, between 70 and 100 °E along 18 °S. Slight freshening at 1000 m depth is seen in the observation, which is captured by most models except ICTP and ACCESS. This freshening is due to the intrusion of Antarctic Intermediate Water in this layer (Wyrtki, 1973). This low salinity layer has a thickness of 500 m or more and can be identified by a salinity minimum of 34.3–34.4 psu at the Subtropical Convergence Zone. Warren (1981) has reported that the salinity minimum of Antarctic Intermediate Water (AAIW) is at depth of 600–900 m along 18°S with depth generally increasing towards the west.

In summary, the vertical salinity structure is more realistically captured by z-level models (MOM and NEMO group of models) except for ACCESS and ICTP. The vertical salinity structure is less well represented by the isopycnal/hybrid models (BERGEN, FSU and FSU2). An increased horizontal resolution in the model marginally improves the salinity simulation.

### 4.5. *Variations in the equatorial currents*

#### 4.5.1. *Surface current*

As seen in Fig. 24a, the CORE-II simulations capture the major current systems shown in Fig. 1. During the northeast monsoon the SC flows southward and is limited to the region south of 10°N. The surface flow reverses in April and November, during the inter-monsoon period (not shown). Observations show that during the southwest Monsoon, the SC develops into an intense jet with extreme velocities of about 2 m/s during mid-May and reaching to 3.5 m/s during June (INDEX, 1976–1979). This jet is very well reproduced in all the models; however, models are unable to capture the observed magnitudes (not shown). The SEC, the westward current south of 10°S, does not undergo any seasonal variation in direction throughout the year. The model simulated SEC shows good fidelity in reproducing the spatial variability seen in the observations (Fig. 24a). Compared to the observation all models show a narrower SEC and an underrepresented SECC pattern.

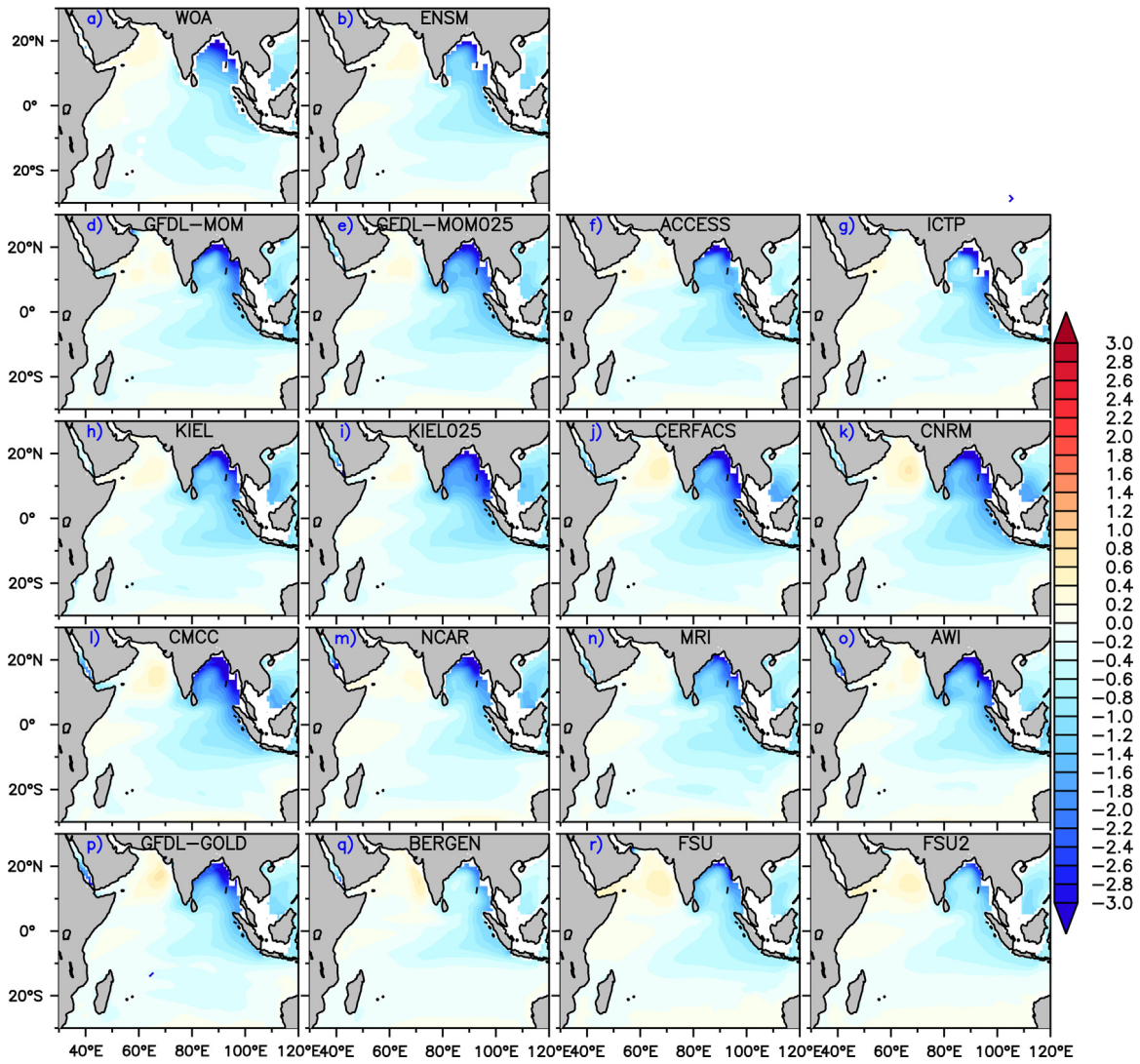


**Fig. 21.** The upper left panel shows the annual mean salinity stratification (surface minus 100 m depth) from the WOA observation, and the upper middle panel shows the same for CORE-II model ensemble mean. Remaining panels show the same for the individual CORE-II models.

Fig. 24b shows the comparison of the seasonal cycle of the WJ between different observations (OSCAR, CUTLER and LUMPKIN) and the CORE-II model simulations. All observations show the spring (autumn) jets peak in May (November) but differing in magnitude by ~ 20 cm/s. Interestingly, all the models show a quite coherent but underrepresented autumn jets; however, there exists a large model spread (25–45 cm/s) in the representation of the spring jet.

### 4.5.2. *Subsurface currents*

Fig. 25 shows the seasonal cycle of sub-surface currents from Acoustic Doppler current profiler (*ADCP*) observations and the CORE-II simulations at 90 °E and the equator. CORE-II simulations are able to capture the semi-annual cycle of the EUC magnitude. Refining the horizontal resolution from GFDL-MOM to GFDL-MOM025 indicates an improvement in the EUC representation. The NEMO groups of models accurately simulate the EUC magnitude. However, all models are unable to capture the timing of the peak values of EUC (Fig. 26b), where the peak magnitude is reached about a month earlier (February) relative to ADCP observations. The pronounced upward phase propagation (Iskandar et al., 2009) is weaker or near absent in the CORE-II models.

The presence of WJ during inter-monsoon period extends down to 100 m (Fig. 25). The ADCP observations are not available in the upper 40 m but the extent of spring WJ can be seen between 40 and 100 m (Fig. 25). To compare the lower part of WJ, the seasonal cycle of upper ocean current averaged over 40–100 m depth from observations and simulations are shown in Fig. 26a. None of the models capture the observed peak spring jet values of ~45 cm/s whereas the models overestimate the autumn jet values. The observed eastward current associated with summer monsoon in July is also not found in any of the models whereas the rest of the season they are more coherent and close to observations.

EUC is present below WJ and it is most prominent at 90–170 m (Iskandar et al., 2009). To examine the simulated EUC seasonal cycle, we show the depth averaged (100–200 m) zonal current from ADCP observation and CORE-II simulations in Fig. 26b. The peak observed EUC value occurs in March–April, but all the models show an early peak in February–March. Iskandar et al. (2009) showed that development of an eastward pressure gradient during winter is responsible for the formation of the EUC with a delay of one month. Equatorial wave dynamics also play a role in the development of EUC. A downwelling Kelvin wave is excited in the western basin in March–April (see their Fig. 8b), which raises the sea level in the western part, whereas an upwelling Rossby wave lowers the eastern basin during same time. These waves are responsible for generating the pressure gradient. In the CORE-II simulations, all models show the appearance of these waves about a month early and hence the pressure gradient force gives rise to an early EUC peak (not shown). The subsurface-surface interactions

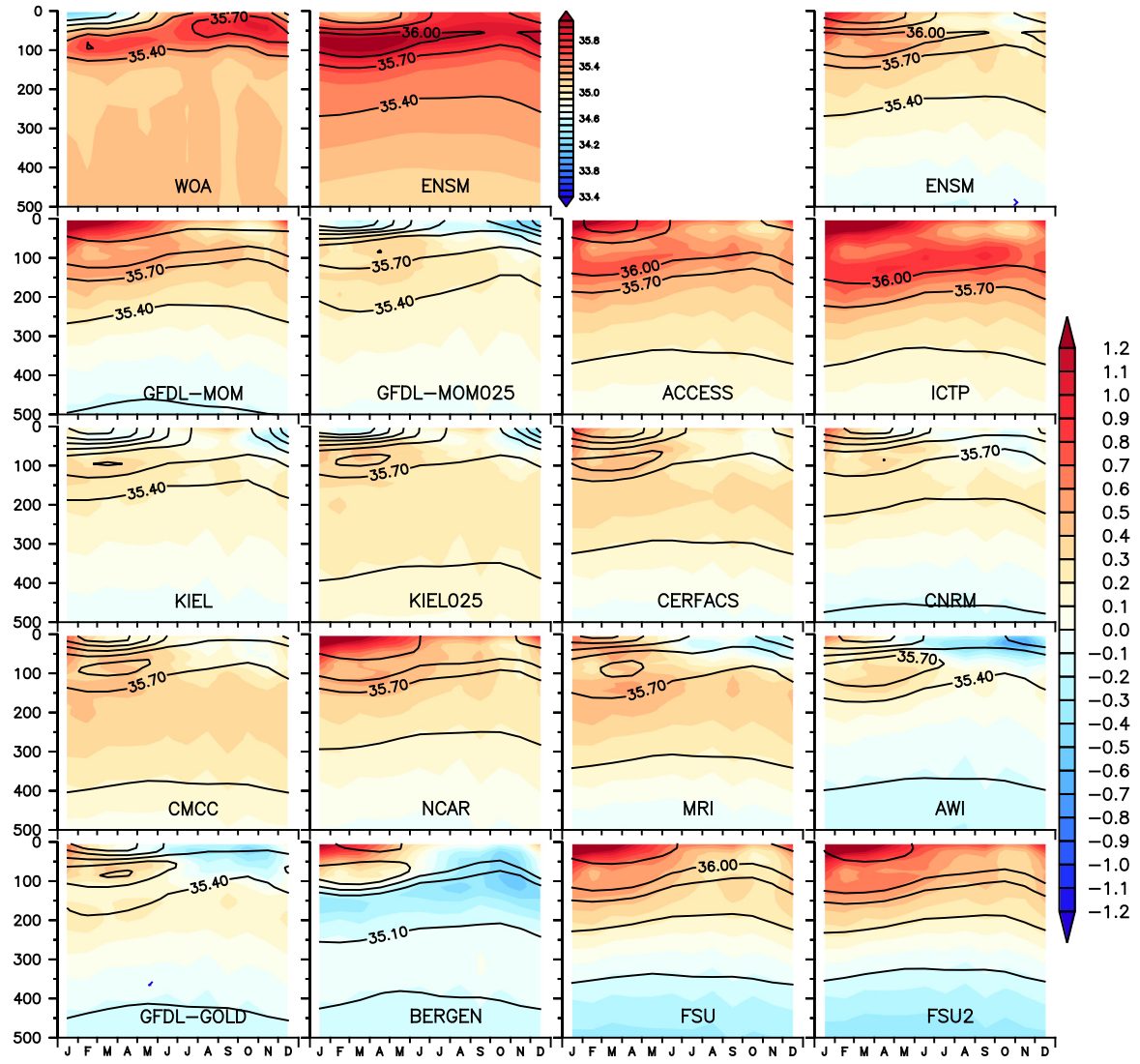


**Fig. 22a.** The upper left panel shows the seasonal variation of WOA salinity with depth over the south eastern Arabian Sea (SEAS). The top middle panel shows the same for CORE-II ensemble mean, and the top upper right panel shows the ensemble mean bias. The remaining panels show the individual CORE-II model bias (model minus WOA) in colors and its mean in contours. Contour levels for WOA observation, all individual models and its ensemble mean are same.

in the ocean are governed chiefly by baroclinic dynamics and wave propagations. If baroclinic dynamics are affected via biases in the resolved vertical structure of density, the associated planetary/Rossby and Kelvin waves will be affected too. These waves are the key controlling factors for thermocline displacements and are at the core of tropical climate variability such as El Nino-Southern Oscillation and Indian Ocean dipole/zonal mode (IODZM). Recently Shikha and Valsala (2018) have shown the subsurface temperature and salinity bias in CMIP-5 models over the Indian Ocean tend to have a positive bias in the speed of first baroclinic mode wave propagation since the first and second baroclinic modes are highly sensitive to density and its biases.

Fig. 27a shows the comparison of annual mean vertical variation of the zonal current at 90 °E and at the equator. The ADCP observations show that the annual mean subsurface zonal current peaks at 80 m depth with a magnitude of 15 cm/s. FSU2 remarkably reproduces this feature. As explained earlier, the NEMO (MOM) class of models over-(under)estimate this observed EUC value. Due to these counter-acting biases, the ensemble mean is relatively close to ADCP observations both in magnitude and depth. The subsurface zonal current in April is shown in Fig. 27b. Most of the models are unable to capture the peak values at the observed depth. Only KIEL simulations are able to capture the observed depth of the EUC, but with an overestimation of up to 10 cm/s. BERGEN and NCAR simulate the peak EUC value, but it peaks at a shallower depth of 90 m. The EUC in the coarse model from ICTP is almost absent, while all other models show a comparable velocity structure as the observations.

The autumn EUC appears at a slightly shallower depth (90 m) compared to spring (~110 m) (Fig. 27c), with the models showing biases in the peak depth and its amplitude. During autumn, most models show stronger EUC with varying peak depths ranging between 45 and 90 m, whereas the observed value is ~35 cm/s at 90 m. The spread of peak EUC values in the autumn is much less than its spring values. But in the autumn, the models are unable to capture the westward current at the depth range 300–400 m seen in observations.

To assess the robustness of the above results, we repeated the analysis at 80 °E, where only 3 years (2005–2007) continuous observational ADCP data is available till 340 m depth (Nagura and Masumoto, 2015). We thus computed a monthly climatology for both ADCP and CORE-II simulated data over that period. At 80 °E location the ADCP and CORE-II model comparisons show coherent results with that at 90°E. The WJ and the EUC are stronger at 80 °E compared to at 90 °E (not shown). Furthermore, the inter-model spread for both currents is reduced at 80 °E. Another notable difference at 80 °E is that the timing of the EUC peak in spring is reproduced by all models. At 90 °E all models exhibit an early peak.

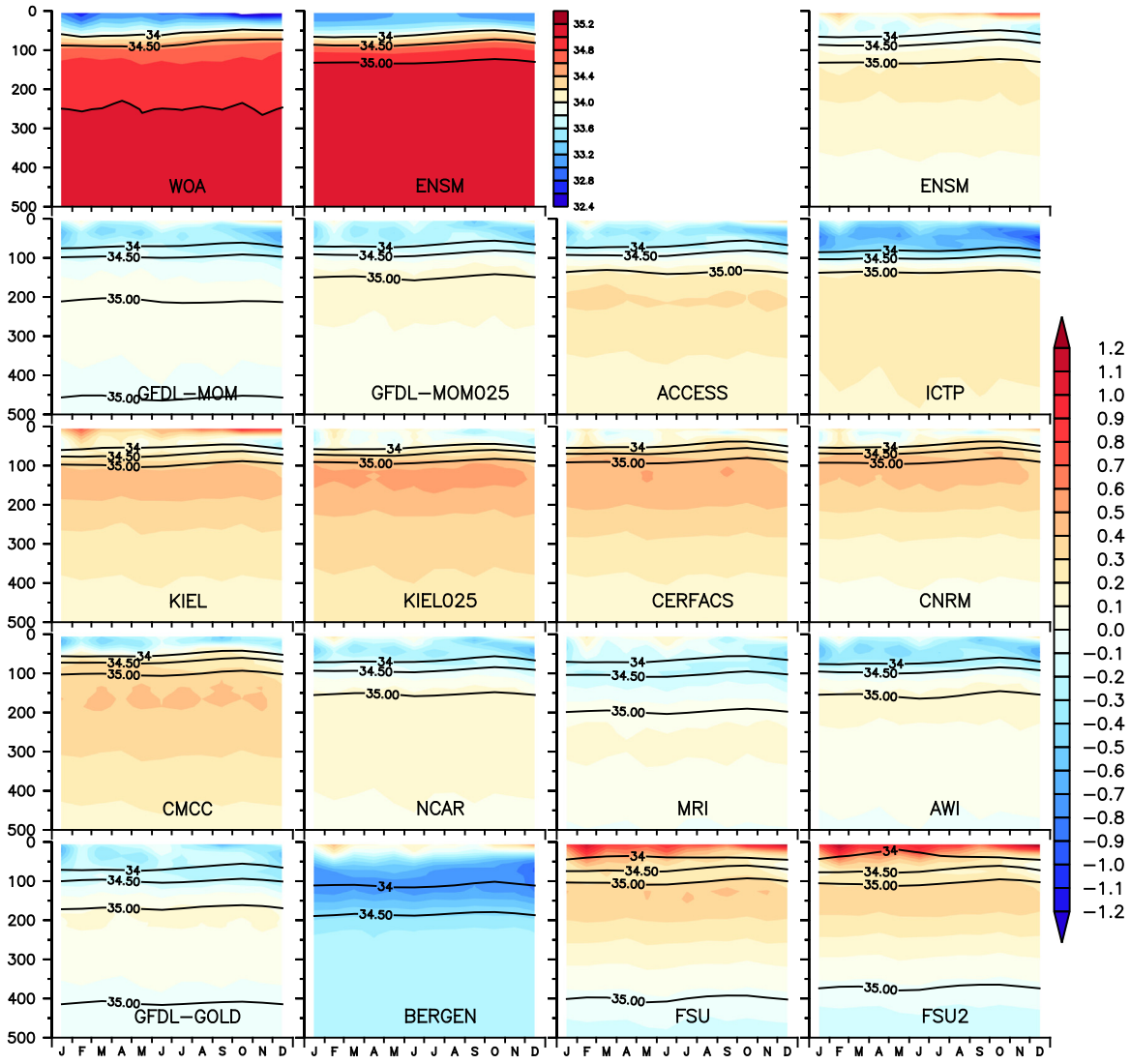


**Fig. 22b.** Same as Fig. 22a but for the Bay of Bengal.

Recently, McPhaden et al. (2015) showed that the volume transport associated with the WJ peaks in May (November) with a transport of 14.9 +/− 2.9 Sv (19.7 +/− 2.4 Sv). The coupled models analyzed by McPhaden et al. (2015) were unable to capture these observed values. We examine here the performance of the CORE-II models by computing the transport following McPhaden et al. (2015). The CORE-II models capture the observed seasonal variation of upper ocean volume transport (not shown). The ensemble mean of zonal transport shows a transport of 18.74 Sv in May and 16.83 Sv in November which is similar to Wrytki jet volume transport reported by McPhaden et al. (2015).

### *4.6. Indian Ocean meridional overturning circulation*

The surface circulation of the northern and the equatorial Indian Ocean shows large seasonal changes due to seasonal reversals of the monsoon winds. The seasonal variability of surface circulation is well known, such as the Somali Current (Schott et al., 1990) and the semiannual equatorial jet (Wyrtki, 1973). However, characteristics of CEC and its underlying mechanisms are not very well known (Lee, 2004). Apart from CEC, the presence of an "equatorial roll" in the mixed layer of the Indian Ocean was also identified in model simulations of Wacongne and Pacanowski (1996), and its presence has been confirmed thereafter by observations (Wang and McPhaden, 2017; Horii et al., 2013; Perez-Hernandez et al., 2012; Schott et al., 2002a,b). This shallow equatorial roll consists of a northward wind-driven surface current in the upper 25 m near the equator overlaying the southward directed subsurface Sverdrup transport. This circulation is narrowly confined to within ±1° of the equator and is most strongly developed seasonally during July–October. However, it has little impact on cross-equatorial heat transport (e.g., Schott et al., 2002a,b; Miyama et al., 2003).

In the north Indian Ocean (north of 10 °S) the annual mean net surface heat flux is directed into the ocean (Oberhuber, 1988; Godfrey et al., 2007). It is the wind-driven meridional overturning circulation in the upper several hundred meters that exports the annual-mean net heat gain towards the subtropical SIO, south of the equator (Wacongne and Pacanowski, 1996; Lee and Marotzke, 1997, 1998; Garternicht and Schott, 1997; Miyama et al., 2003). Godfrey et al. (2007), evaluating a variety of different models over the Indian Ocean, found a mean heat transport more than double the mean obtained when averaging the observed climatology. The CEC is very important for the NIO warming and sea level variability (Srinivasu et al., 2017; Swapna et al., 2017).

Fig. 28 shows the Indian Ocean Meridional Overturning circulation (IOMOC) computed from all the models and the ORAS4 reanalysis. Most of the models are able to simulate the CEC, while there is almost no thermocline northward flow in the coarse model from ICTP. The mean strength of CEC varies in different models and is in the range of

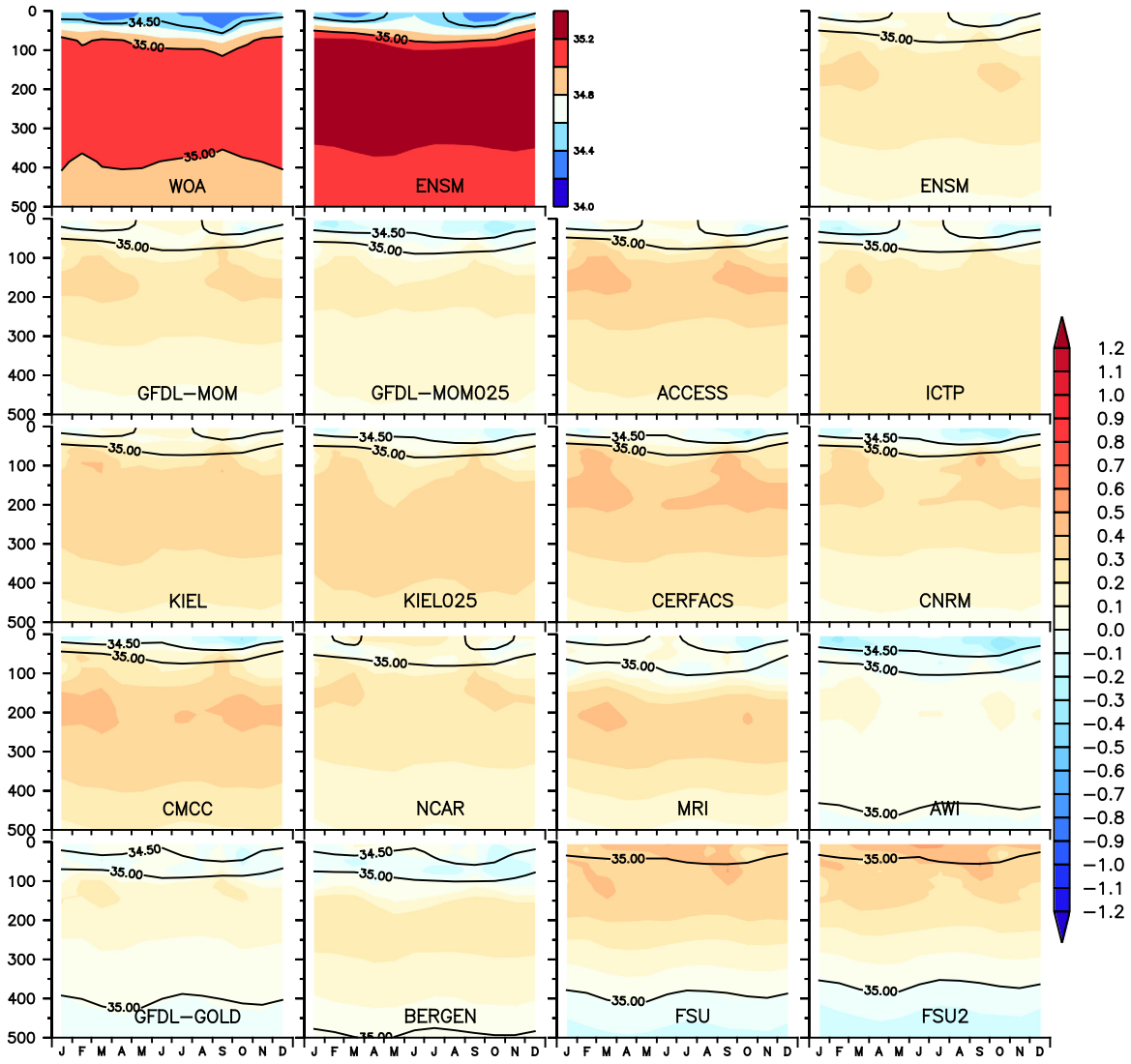


**Fig. 22c.** Same as Fig. 22a but for the Eastern Equatorial Indian Ocean.

2–8 Sv. This value is within the earlier reported value of 6 Sv (Lee and Marotzke, 1997; Schott et al., 2002a,b). The CEC structures as demonstrated by Miyama et al. (2003) is well reproduced by a majority of the models (Fig. 28). The ensemble mean from the entire model suite is shown in upper middle panel of Fig. 28. The CEC structure is prominent and it corroborates the finding of Miyama et al. (2003).

Although Miyama et al. (2003) have shown the pathways of CEC, the vertical extent and the exact location of equatorial crossing have not been reported in earlier studies. To quantify the vertical extent and exact location, we plot the cross equatorial transport across the equator. The cross equatorial transports from all the individual models show the vertical extent of the northward cross equatorial flow extends over the full water column near the African Coast (Fig. 29). The magnitude of this flow varies and is strongest in CERFACS, CNRM, AWI, FSU and FSU2. The ensemble mean cross equatorial transport with depth is shown in the upper middle panel of Fig. 29. A narrow band of CEC near the Somali coast can be seen from Fig. 29, with vertical extent of the transport that extends to 1500 m. All the models show another secondary pathway of northward transport of cross equatorial flow along 75 °E with a value ranging 5–10 $m^2/s$. These values are more prominent and higher in the fine resolution MOM and KIEL simulations with a maximum value of ~20–25 $m^2/s$. With islands and seamounts along 75 °E (the Maldives and Chagos Archipelago), topography plays a major role for the northward transport along that longitude. Nagura and Masumoto (2015) used in-situ observations and OGCM output to find a northward current at about 75 °E. They discussed its dynamics using 1.5-layer model experiments and found that the WJ hits the Maldives Islands near 73 °E and meanders, leading to a northward current near the islands. The KIEL and MOM topography do not show the presence of Maldives Island along the 73 °E in the upper 1000 m. However, the MOM025 and KIEL025 models show the presence of bathymetry at 45 m depth onwards (not shown). The annual mean currents in the models at 200 m and below are mostly zonal along the equator. As reported by Nagura and Masumoto (2015) the presence of Maldives Island around 73 °E meanders this zonal current and leads to northward current at the southern flank of the Island, which mainly drives the northward transport seen in Fig. 29 for the 1/4 degree MOM and KIEL simulations.

The strong southward flow apparent in the KIEL models near to the Somali coast is due to the stronger meridional currents seen in these models. This strong southward current is absent in other models (not shown). The transport along the African coast across 5 °S is stronger than across the Equator (not shown). This band is also a slightly wider across 10 °S. Observations show a strong northward transport (25–30 $m^2/s$) along 50 °E across the 10 °S latitude (not shown). Only GFDL-MOM and ICTP are able to capture this band.

We conclude that most CORE-II models simulate the structure of the CEC in the Indian Ocean. Additionally, the CORE-II analysis uncovers a

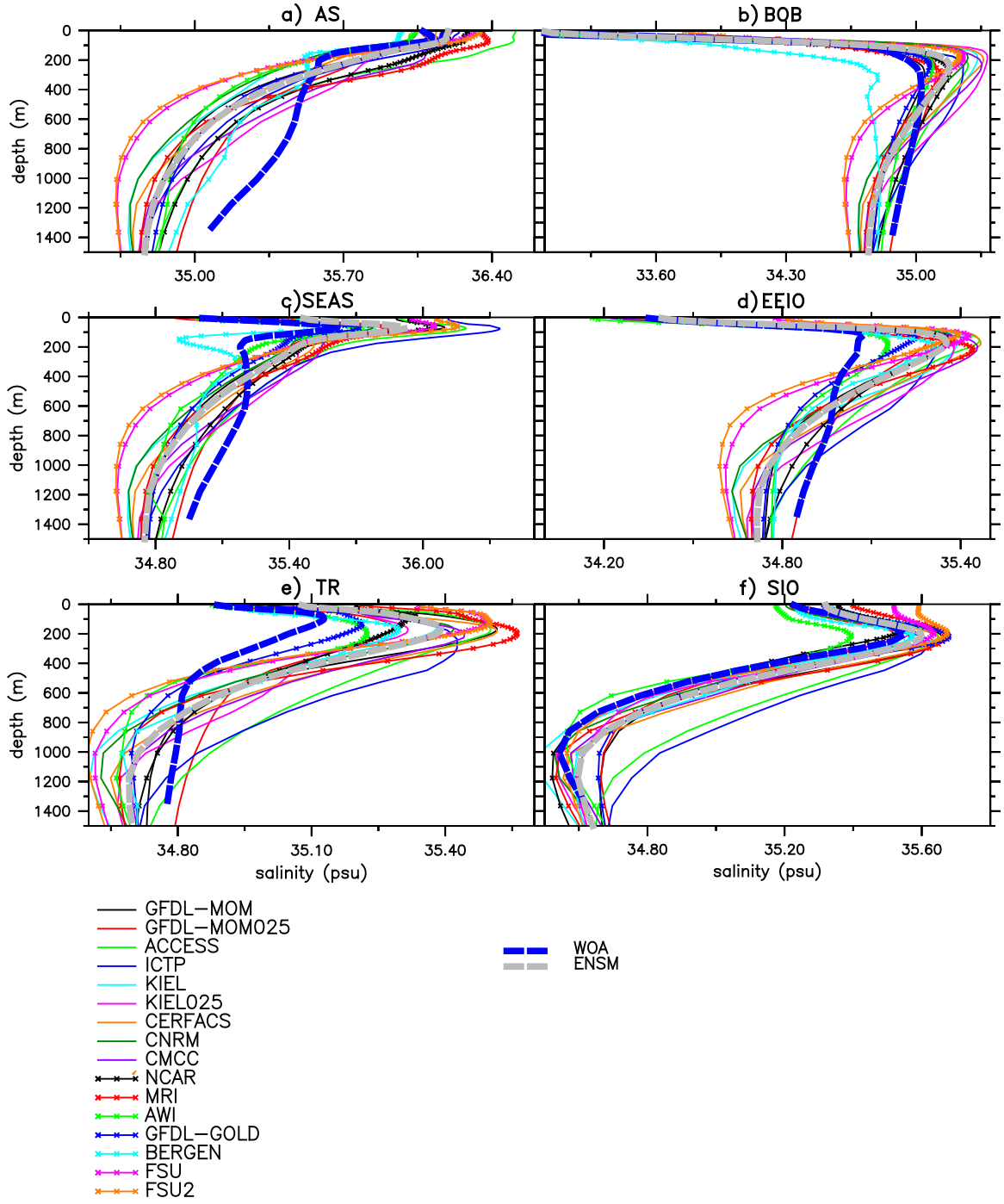


**Fig. 23.** Annual mean vertical salinity variations from the CORE-II simulations as compared to WOA observation averaged over different sub-regions in the Indian Ocean: (a) Arabian Sea(AS), (b) Bay of Bengal (BoB), (c) South Eastern Arabian Sea (SEAS), (d) Eastern Equatorial Indian Ocean (EEIO), (e) Thermocline Ridge (TR) and (f) Southern Indian Ocean (SIO). (see Section 3.4 for sub-region specifications).

previously unidentified secondary pathway of CEC. Namely, there is a northward cross-equatorial transport along 75 °E, which is also present feebly in ORAS4, complements the pathway near the Somali coast.

## 5. Summary of impacts from model resolution

Momin et al. (2014) is the only study that reported on the impact of model resolution for Indian Ocean simulations. They showed an overall marginal improvement in D20, SST and SSS, though with a degradation in SST seasonal cycle over the equatorial Indian Ocean. In earlier sections, we identified a variety of features that differ across the ICTP, GFDL-MOM/GFDL-MOM025 and KIEL/KIEL025 resolution suite. In this section, we discuss these two resolution suites with a focus on the Bay of Bengal.

Fig. 30a shows the comparison of SST simulation derived from KIEL and MOM. Both coarse and fine resolution models capture the observed seasonal cycle. Increased resolution does not improve the biases in spring (MOM) and summer for neither KIEL nor MOM. The KIEL and KIEL025 simulations reproduce the observed SST variation during winter and spring, associated with a good representation of the BL thickness (Fig. 30b).

The observed thermocline seasonal cycle is well captured in MOM with some improvement in MOM025. However, the KIEL and KIEL025

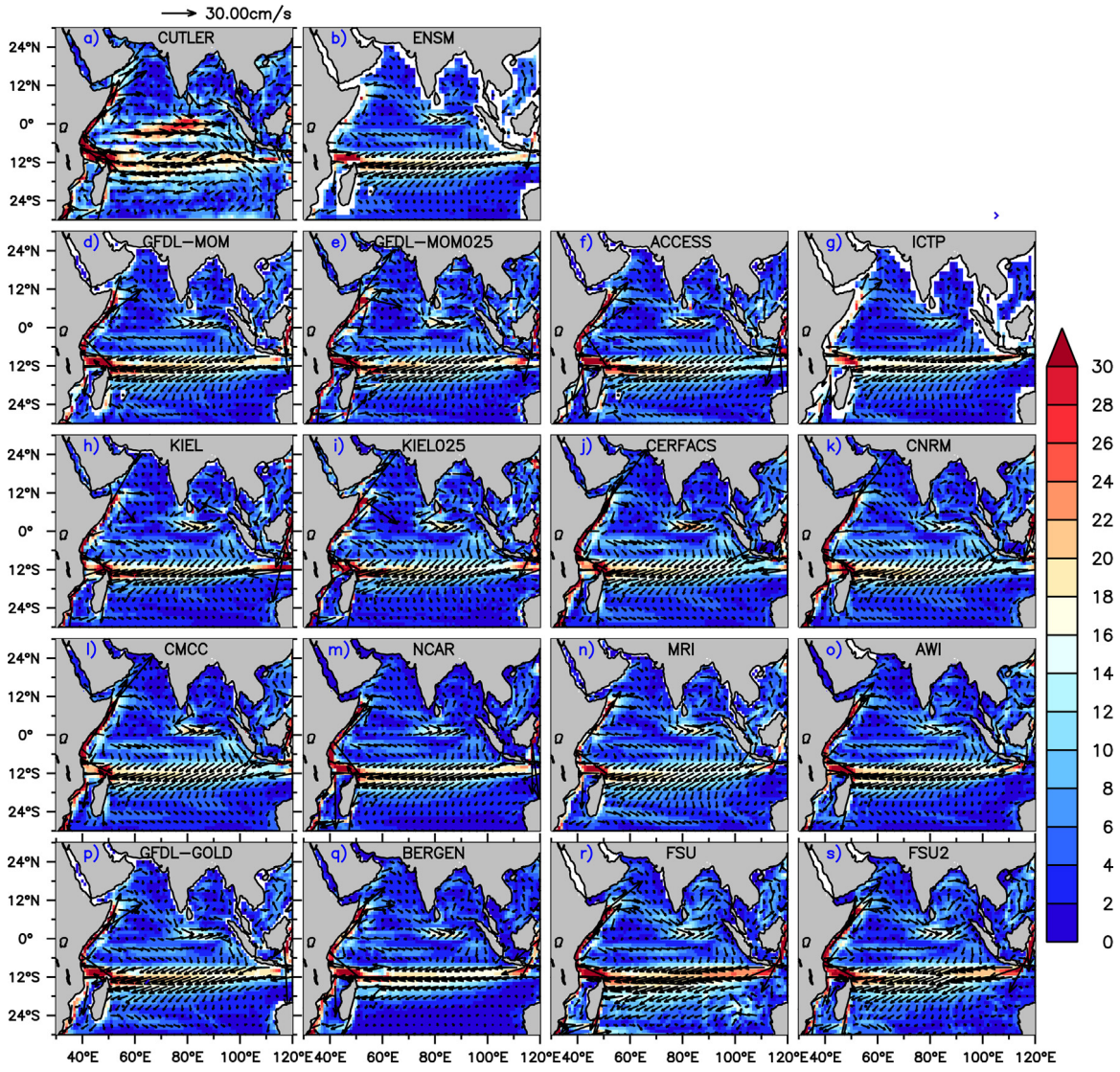


**Fig. 24a.** Annual mean surface current comparison (current speed is given in color) with ship drift observation. The upper left panel shows observations (CUTLER) and the upper middle panel shows CORE-II ensemble mean. The remaining panels show the individual CORE-II models. Units are in cm/s.

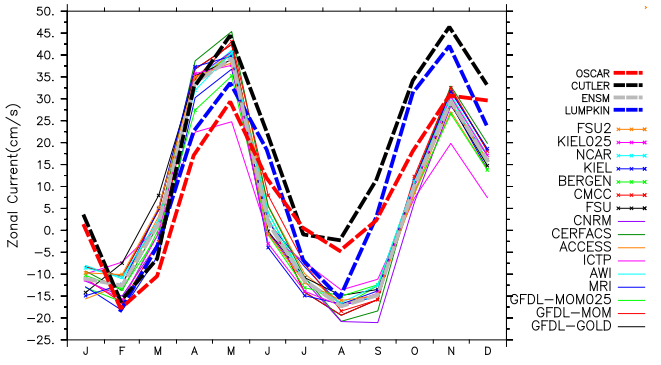


**Fig. 24b.** Seasonal cycle of zonal currents at the WJ location [55–80°E, 2.5°S – 2.5°N] averaged over 0 −15 m depth from CORE-II simulations and observations (CUTLER, OSCAR, LUMPKIN).

simulations show a systematic bias of ~20 m in 20 °C isotherm (D20) throughout the season (Fig. 30c), possibly as a result of differences in parameterizations between KIEL and MOM. Enhanced horizontal resolution shows a significant improvement in the MLD simulations both in MOM025 and KIEL025 as compared to their coarse resolution counterparts (Fig. 30d). The mixed layer depth in MOM025 and KIEL025 shows similar value to WOA during spring and summer, but deeper by ~10 m during autumn and winter. Their coarse resolution counterparts show ~20 m deeper MLD as compared to WOA observations. The vertical temperature difference with respect to WOA observations is shown in Fig. 30e. KIEL does not show any significant improvement in vertical temperature simulations as resolution increases, but MOM shows a slight warming in the deeper layer when refining the resolution, which can also be seen in the seasonal bias plot in Fig. 20b. For salinity, MOM shows improved simulations below the thermocline as resolution increases, but in KIEL bias slightly increases with increase in resolution (Fig. 30f).

Fig. 31 shows the annual mean cross equatorial transport with depth along the equator for MOM, MOM025, KIEL, KIEL025, ensemble mean of all models and ORAS4. As explained in the previous section, the coarse resolution models do not show much transport across 72–76 °E, but with enhanced resolution this transport is very prominent with magnitude of 25–30 $m^2/s$. Earlier modeling studies show that the cross equatorial volume transport is maximum near the Somali coast in a narrow band between 43 and 46 °E (Jensen, 2003, 2007; Miyama et al., 2003). The coarse resolution MOM and KIEL simulations also show the similar band in the surface layer, with the high resolution (MOM025

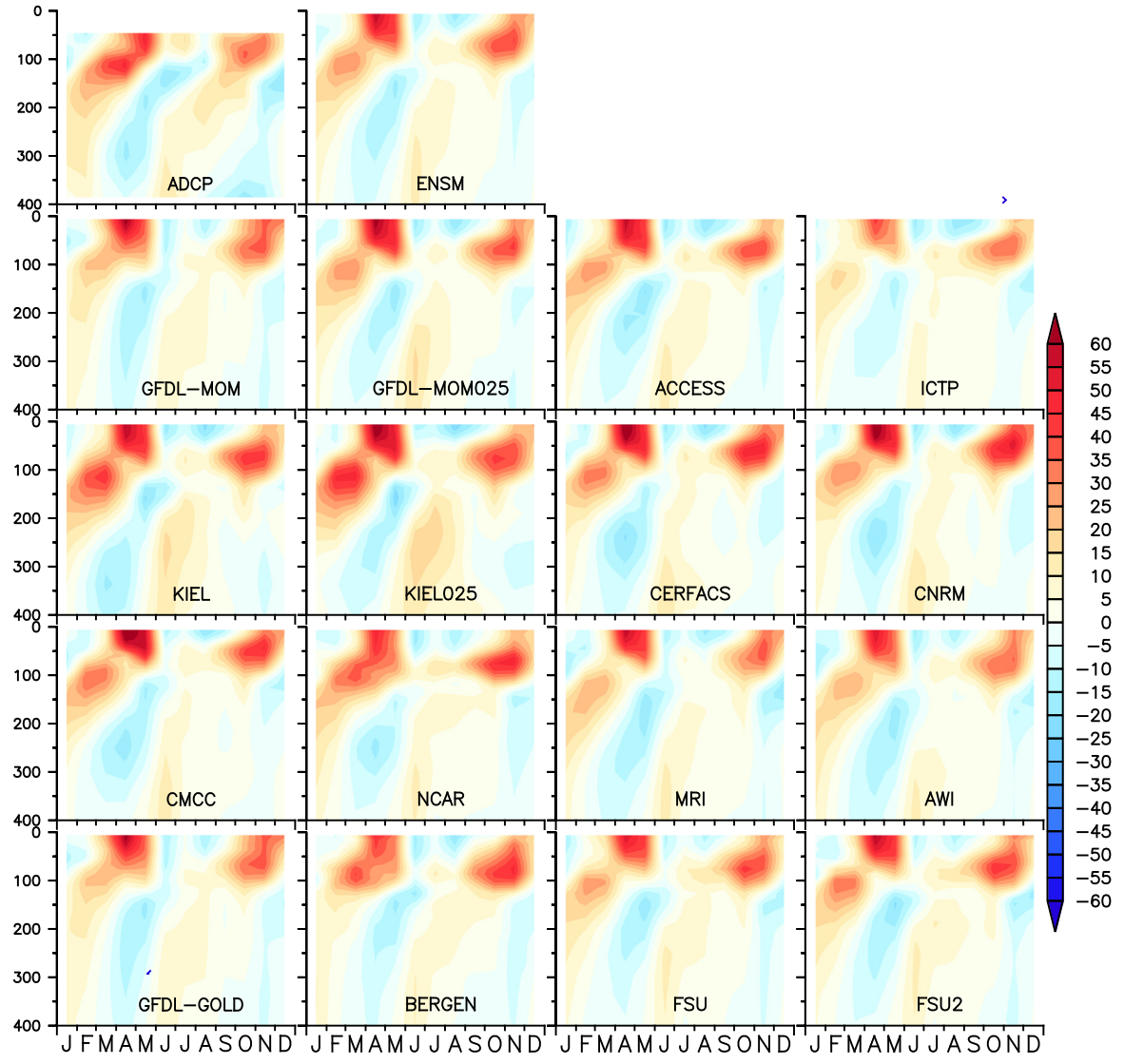


**Fig. 25.** Upper ocean mean zonal current (cm/s) comparison of CORE-II simulations with ADCP observation at 90°E and equator. The mean is computed for 2001–2007 for both models and ADCP observation.

and KIEL025) showing even narrower band of cross equatorial flow near the Somalia coast (Fig. 31) with much stronger value (~50 $m^2/s$) and a strong secondary pathway along 72–76 °E. As previously reported at around 50 °E a weak cross equatorial transport can be found in the simulations except for the MOM025 configuration. The cross equatorial transport near Somalia coast is mainly contributed from July (Fig. 32b), whereas there is a negligible cross equatorial volume transport during January (Fig. 32a) over the Somali coast.

There is stronger cross equatorial transport in the subsurface with enhanced resolution in KIEL025 as well as MOM025. The secondary cross equatorial pathways of volume transport along 72–76 °E in the subsurface appear in the high resolution models both during winter and summer (Figs. 32a, 32b). This feature is absent or near absent in the coarse resolution models in the ensemble mean and ORAS4 reanalysis products as well.

We conclude that increasing the horizontal resolution does not necessarily improve the temperature and salinity properties noticeably. However, increased resolution with a realistic topography representation does improve fidelity in the cross-equatorial pathways in the Indian Ocean.

## 6. Summary of the assessment

We presented an analysis of 16 ocean/sea-ice models forced according to the Coordinated Ocean-ice Reference Experiments (CORE) interannual protocol, focusing here on the annual mean and seasonal features of the Indian Ocean. This assessment is the first of its kind, and thus it offers an important benchmark for further studies with global ocean/sea-ice models or fully coupled climate models. In particular, we documented the mean state by analyzing surface properties (SST, SSS and surface currents), subsurface properties (temperature, salinity and currents), and the MOC. The SST from CMIP5 simulations was also utilized to compare the coupled and CORE-II simulations.

Our study provides an assessment across a suite of high-end global ocean climate models, many of which were part of CMIP5 climate models. We identified many biases with the simulations, and offered suggestions for where these biases might be related to limitations in the CORE-II forcing or the ocean model physical parameterizations. As in other CORE-II assessments, we do not perform sensitivity studies to support hypotheses for what mechanisms lead to the diagnosed model biases. Nevertheless, our study provides a critical baseline from which future targeted studies can address these limitations. This perspective forms the basis for the nine other published CORE-II assessments.

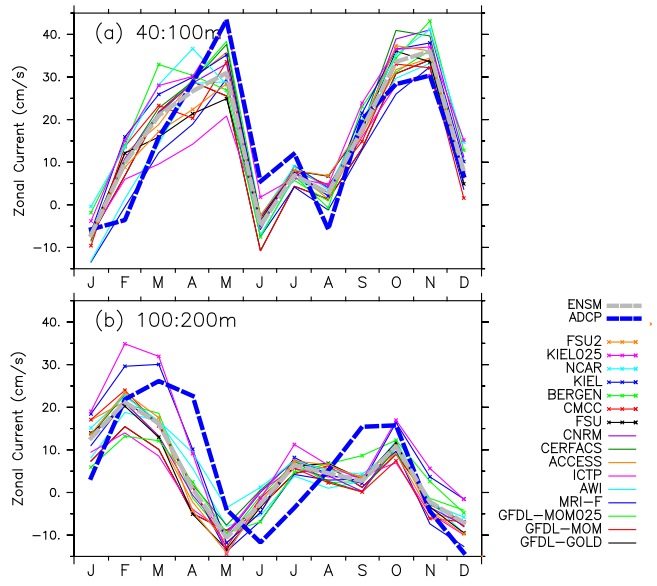


**Fig. 26.** Seasonal cycle of zonal current at 90 °E and the equator from CORE-II simulations and ADCP observation (a) averaged over 40–100 m depth and (b) averaged over 100–200 m depth. Model ensemble mean is also plotted in gray.

In the following we offer a summary of the main results from our assessment.

### 6.1. Sea surface temperature

CORE-II models show improvement in capturing the observed seasonal variability with less bias compared to the coupled models, and their SST biases are ~2 times smaller than coupled simulations. The SST simulations from coupled CMIP5 models that we analyzed are dominated by a negative (cold) bias in the Indian Ocean of about 1–2 °C, with large inter-model spread particularly over the EEIO. Additionally, CMIP5 models are generally unable to simulate the timing and magnitude of peak SST values, thus affecting the seasonal cycle over the AS, the BoB and the EEIO. This result emphasizes the need to improve the atmosphere and ocean components of coupled climate models and their coupling to improve their representation of regional Indian Ocean features.

We comment in particular on the northern AS, where the CORE-II simulations show a negative (cold) SST bias (1–2 °C) during February to April, which is increased to (2–3 °C) in the CMIP5 models. Previous studies showed that the advection of cold air from the Asian land mass causes this large cooling in coupled models (Marathayil et al., 2013; Sandeep and Ajayamohan, 2014). We also find that this large bias arises from a deeper MLD over this region in the CORE-II simulations.

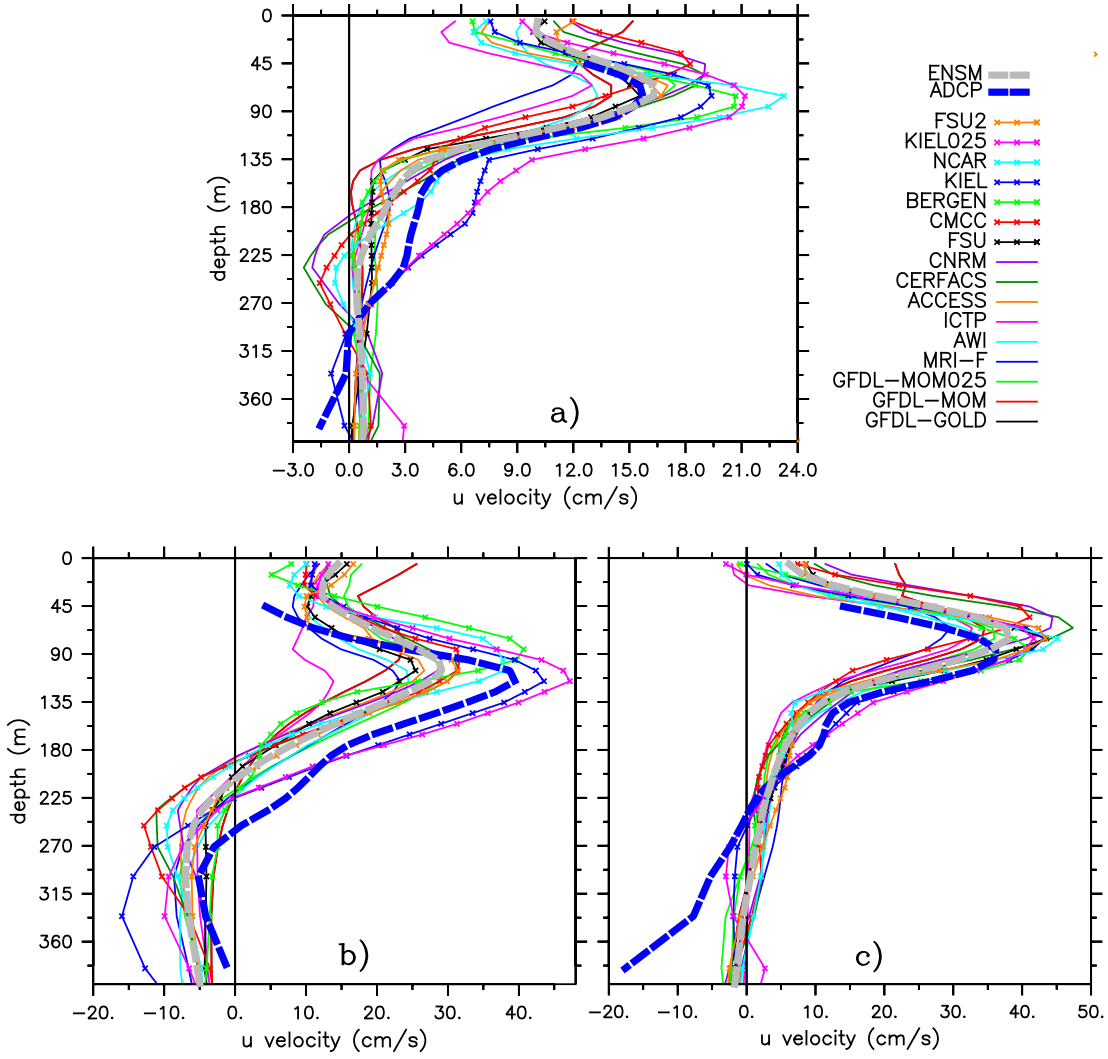


**Fig. 27.** The upper ocean zonal current with depth at 90 °E and the equator from CORE-II models and ADCP observation (a) Annual mean, (b) April mean and (c) October mean. The mean is computed for 2001–2007 for both models and ADCP observation.

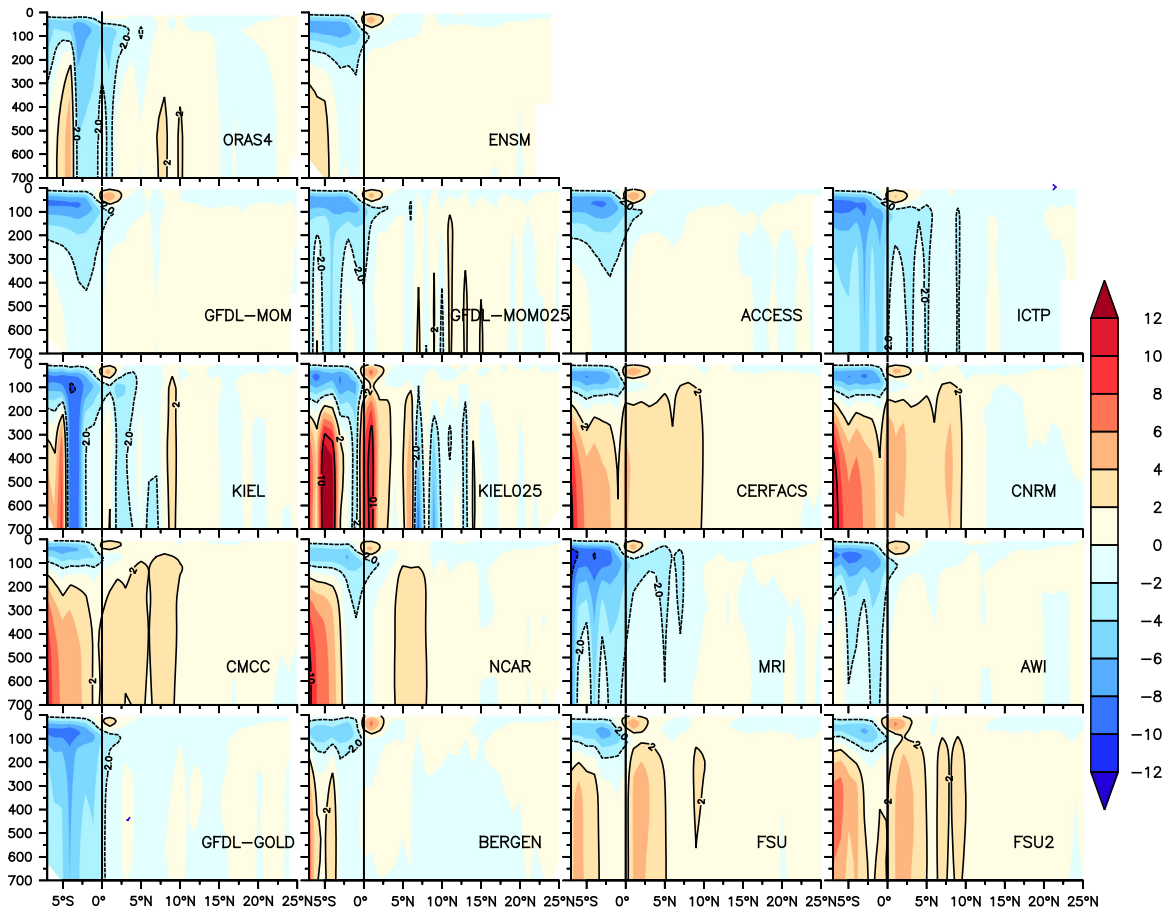


**Fig. 28.** Indian Ocean meridional volume transport (IOMOC) from CORE-II simulations and ORAS4 analysis. Units are in Sv.

### *6.2. Sea surface salinity (SSS) and barrier layer*

The CORE-II models show a positive salinity bias in the BoB, the AS and the SEAS. The simulations from FSU and FSU2 consistently overestimate the SSS throughout the basin, particularly over the BoB, the EEIO and the SIO, with these two models exhibiting the largest bias among the CORE-II models. The seasonal cycle of SSS shows that inter-model spread is larger in the AS and the SIO. The unrealistic seasonal cycle in CORE-II models in the AS might be due to the unrealistic representation of the overflow of high salinity waters from the Red Sea and Persian Gulf into the AS. The intrusion of high-salinity water from the AS to the BoB during the summer monsoon (Murty et al., 1992; Vinayachandran et al., 1999) is not realistic in most of the models, particularly in FSU and FSU2. Peak river runoff and the integrated summer rainfall lead to a SSS minimum in October over the BoB. Only CMCC captures the seasonal cycle with low salinity in October reflecting those found in observations. Whereas SST simulations do not notably improve with enhanced resolution, the SSS simulation improves significantly when moving to the eddy permitting models KIEL025 and GFDL-MOM025 compared to their respective coarser counterparts.

The seasonal variation in the BL becomes most prominent during December–January when it reaches 40 m thickness and is mainly driven by substantial river runoff into the northern BoB. None of the models capture this thick BL over the northern BoB. The NEMO models (KIEL, CERFACS, CNRM and CMCC) reasonably capture the BL and the east–west gradients. The MOM based models and the hybrid-coordinate models are unable to represent the observed BL variation. We conjecture that the inability of MOM class of models to simulate the BL, in contrast to the NEMO models, might be due to the use of distinct vertical turbulence mixing schemes.

### *6.3. Indian Ocean circulation features*

The CORE-II models are able to simulate the Indian Ocean circulation features with reasonable accuracy. The WJs are weakest in the ICTP simulations (coarsest resolution model in the suite) and are more faithfully represented in the other MOM and NEMO class of models. All the models capture the observed seasonal cycle of WJs except ICTP, which underestimates both the spring and autumn jets. Interestingly, all the models show converging values in the autumn jets, however there is a larger spread among the models for the spring jet.

Three different observations (OSCAR, CUTLER and LUMPKIN) show the spring (autumn) jets peak in May (November) but they differ in magnitude. The SMC is almost absent in some models and the NMC is weaker in ICTP (again we hypothesize that this weakness is due to the coarse resolution of 2° used in the ICTP model). AWI, BERGEN, NCAR and FSU2 also show a near absence of observed peak values of SMC. We found a splitting of the zonal currents at ~10°N off the Somali coast in the AS during peak summer monsoon in the observation which is absent in all simulations. This splitting has not been noted in previous studies and is worthy of further investigation in the future using model and observational data.

All models underestimate the spring WJ peak values of ~45 cm/s found in ADCP observations, whereas all models overestimate the autumn jet values. The observed eastward current associated with the summer monsoon in July is also poorly simulated by the CORE-II models. The NEMO group of models most accurately simulates the EUC magnitude. However, all models show an inaccurate timing of the peak values of the EUC, with models showing their peak magnitudes about a month earlier (February) than the ADCP observations (March).

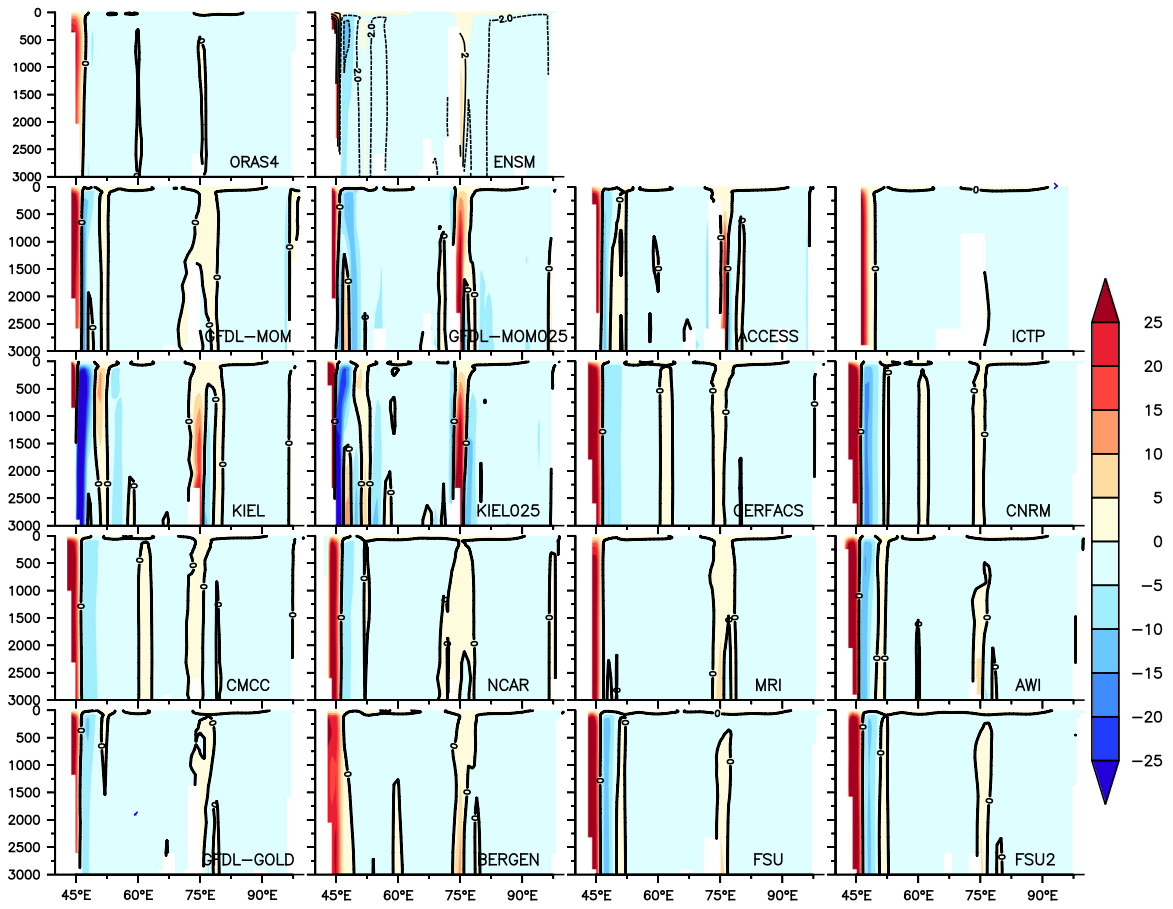


**Fig. 29.** Transport across the equator from all the models. The upper left panel shows transport from ORAS4 reanalysis product. The upper middle panel shows transport from CORE-II ensemble. The remaining panels show transport from all CORE-II individual models. The maximum transport occurs through a narrow passage near to Somali Coast. Note that the 1/4 degree simulations from MOM025 and KIEL025 show large transport at ~75°E. Units are in $m^2/s$.

### 6.4. Subsurface temperature and salinity

All models show a basin wide warm bias at 100 m depth (typically the mean thermocline depth) except GFDL-GOLD, which shows a slightly cold bias over the EEIO and eastern AS. ICTP and BERGEN show the largest bias (>3 °C) over the western equatorial Indian Ocean. Many models (ICTP, MRI, and BERGEN) show a warmer subsurface layer over central AS. CMCC and GFDL-GOLD well reproduce the observed spatial distribution of subsurface temperatures. The MOM group of models (GFDL-MOM, GFDL-MOM025, ICTP and ACCESS) is unable to reproduce the spatial extent and magnitude of the TR region. These models show a higher temperature at 100 m depth as compared to WOA. Although CMCC and GFDL-GOLD capture the TR cooler water, they show a cold bias in the EEIO. The observed spatial distributions are most accurately reproduced by CMCC whereas the BERGEN and ICTP simulations perform the worst.

The seasonal evolution of subsurface temperature shows distinct differences. All the models show a positive (warm) thermocline bias over the AS, BoB and EEIO with a magnitude ranging from ~1 to 4 °C. MRI and ICTP show the warmest thermocline bias (3–4 °C) among all the models in all the regions, whereas GFDL-GOLD shows a slightly cold thermocline bias. The NEMO group of models shows a reduced bias (~0.5–1 °C) in the AS. AWI, FSU and FSU2 also show a similar low thermocline bias over the AS. Over the EEIO, isotherms below 100 m show a clear semiannual signal reaching to 500 m depth. The thermocline bias shows seasonality in all the models. Over the AS and the EEIO there are maximum biases during winter and spring, but over the BoB the models show maximum biases during the summer time. Increased spatial resolution in the model increases the thermocline bias over AS and BoB, possibly as a result of increases in spurious mixing (Griffies et al., 2000; Ilıcak et al., 2012).

The MOM (GFDL-MOM, GFDL-MOM025, ACCESS and ICTP) and NEMO (KIEL, KIEL025, CERFACS, CNRM and CMCC) group of models show stronger upper ocean salinity stratification near the north BoB as compared to WOA, but over the south BoB they show weaker salinity stratification. AWI, BERGEN, FSU and FSU2 are unable to capture either north or south BoB salinity stratification.

### 6.5. Meridional overturning circulation and cross equatorial transport

The MOC in the Indian Ocean consists of a CEC and a Subtropical Cell (STC) also called southern cell (see Fig. 1b). The CEC is a shallow (~500 m) meridional overturning circulation consisting of the northward flow of southern-hemisphere thermocline water, upwelling in the northern hemisphere, and a return flow of surface water (Miyama et al., 2003). Most of the CORE-II models simulate the structure of the CEC. The mean strength of the simulated CEC is in the range of 2–8 Sv, which is within the earlier reported value of 6 Sv (Lee and Marotzke, 1997; Schott et al., 2002a,b). The CEC structures reported by Miyama et al. (2003) are well reproduced by a majority of the CORE-II models.

Maximum transport occurs through a narrow passage near the Somali Coast as reported by Miyama et al. (2003). All simulations show a single narrow band of cross equatorial flow near the Somali Coast, but its vertical structure is yet unknown (see Figs. 3 and 4 of Miyama et al., 2003). This study shows that the vertical extent of the transport extends to 1500 m.

All models show a secondary pathway of northward transport of cross equatorial flow along 75 °E with a value ranging between 5 and

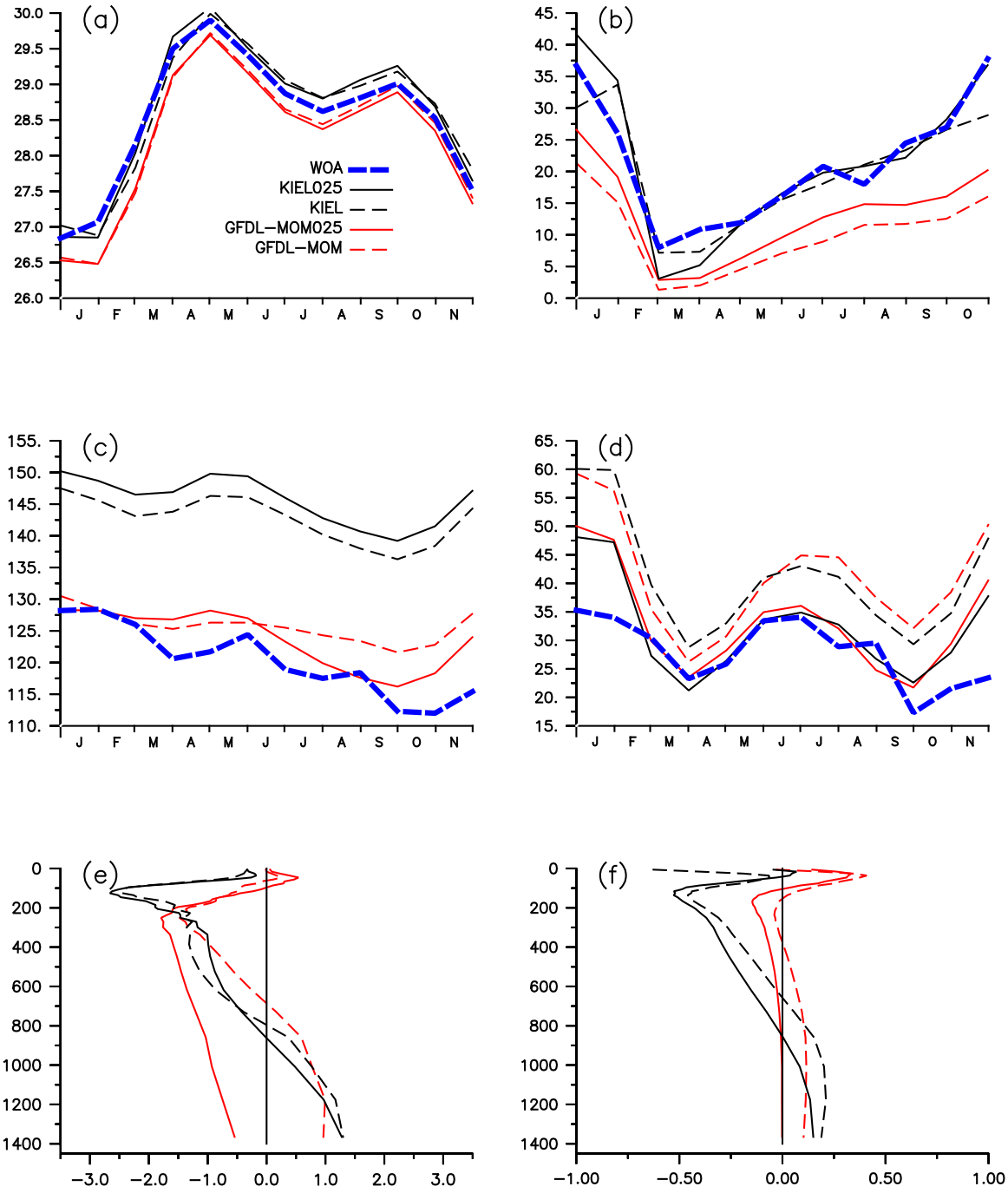


**Fig. 30.** Seasonal cycle of (a) SST, (b) Barrier Layer Thickness, (c) Thermocline Depth, (d) mixed layer depth for 1 degree and 1/4 degree MOM and 0.5 degree and 1/4 degree KIEL models. Vertical temperature (e) and salinity (f) bias (model minus observation) with respect to WOA observation. The averages are taken over the Bay of Bengal.

10 $m^2/s$. These values are more prominent and higher in the high resolution MOM025 and KIEL025 models with a maximum value of ~20–25 $m^2/s$.

Thus, most CORE-II models simulate the structure of the CEC in the Indian Ocean. Importantly, the CORE-II analysis uncovers a previously unidentified secondary pathway of CEC, northward cross-equatorial transport along 75 °E, thus complementing the pathway near the Somali coast. We plan to study this secondary pathway in future studies targeted on the dynamics of this flow.

### 6.6. Comments on model resolution

ICTP is the coarsest model considered in this study, which has a nominal 2 degree horizontal grid spacing with 30 vertical levels. For many of the metrics assessed in this study, this coarse model performed the worse. We therefore suggest that Indian Ocean simulations should be conducted with grid spacing no coarser than the 1 degree used by the bulk of the models considered here.

When comparing the one degree and one-quarter degree simulations, we find that moving to a fine horizontal resolution plays a large role in improving mesoscale eddy dominated processes and strong confined boundary current regions. In particular, for the eddy active BoB region the simulations are better represented using 1/4 degree models (MOM025 and KIEL025) than their coarser resolution (1° MOM or 0.5° KIEL) counterparts. Furthermore, an improvement is seen in the representation of mixed layer depth, and SSS with simulations of 1/4° as compared to their coarse resolution counterpart. However,

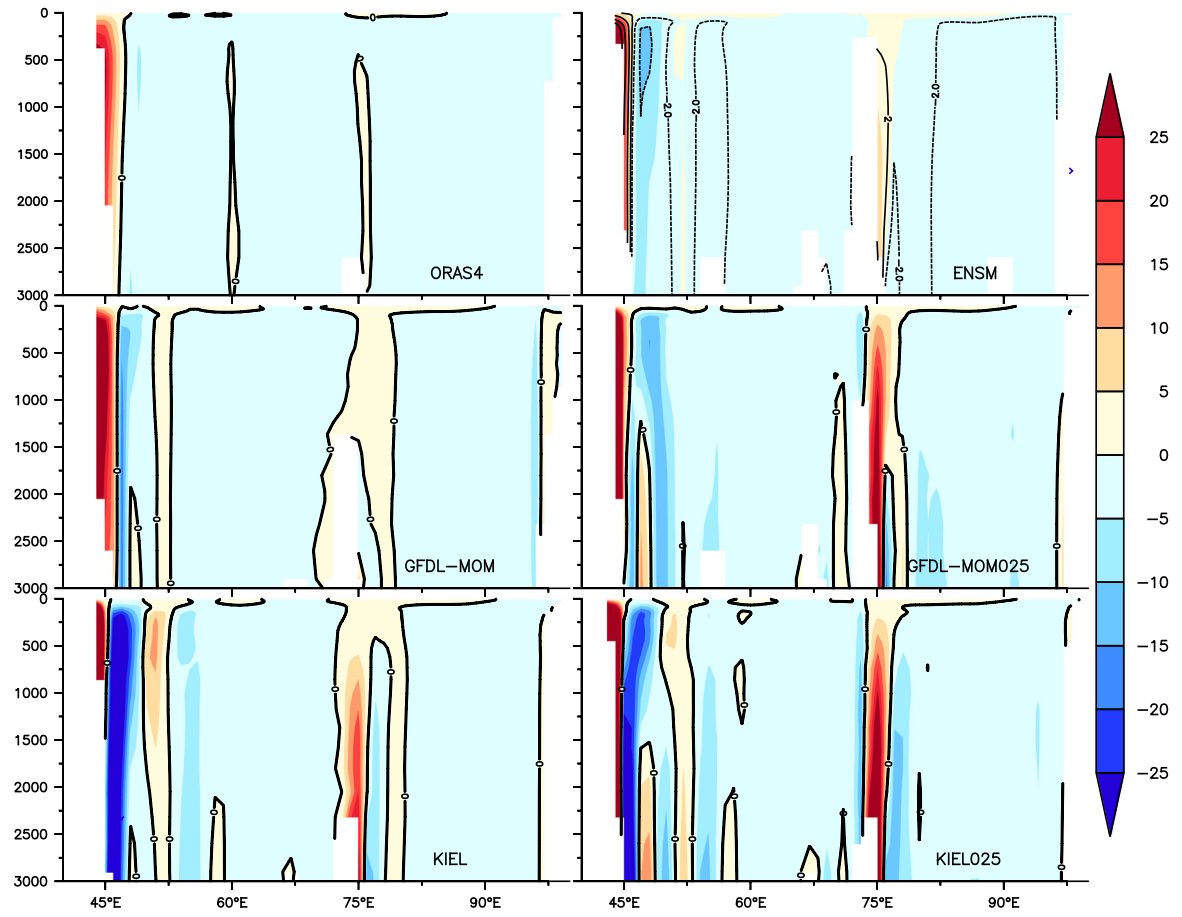


**Fig. 31.** Annual mean transport across the equator from MOM, MOM025, KIEL, KIEL025, all model ensemble and ORAS4. Units are in $m^2/s$.

the thermocline becomes deeper as well as the vertical temperature and salinity representation degrades in 1/4° models compared to their coarser resolution counterparts. This is reflected in the SST features which are not improved, thus suggesting that many biases result from limitations due to physical parameterization (e.g., vertical mixing in the boundary layers) rather than limitations due to horizontal grid resolution.

Our current understanding of the meridional overturning circulation in the Indian Ocean is based largely on non-eddy-resolving models. The CORE-II simulations provide new insight on the cross-equatorial cell, which is an important component of MOC in the Indian Ocean. A future analysis will target how these new pathways improve the inter-annual variability of the Indian Ocean.

### 6.7. Closing comments about the present study and its future implications

The Indian subcontinent and surrounding south Asian region are home to billions of people whose livelihood depends on the ISMR. Hence, a timely and accurate prediction of the monsoon rains is crucial throughout this region. Presently, many global prediction centers predict ISMR on a seasonal time scale. The seasonal prediction skill for tropical SST anomalies provides the major predictability source of monsoon precipitation, and is closely linked to the models' ability to accurately simulate the mean SST (Sperber and Palmer, 1996; Lee et al., 2010; Pokhrel et al., 2012a, 2016; Saha et al., 2019). Current coupled models generally show cold biases over the Indian Ocean. Our study of CORE-II simulations shows that these biases are reduced in CORE-II forced simulations, thus suggesting that the origin for the coupled biases is mostly related to coupled feedbacks that amplify ocean and atmospheric biases. However, apart from this coupled feedback the coupled mode SST bias also arises due to the tuning effect to make coupled model's global mean temperature comparable to observations.

The present study also shows that despite using the same atmospheric state and experimental protocol, the oceanic response from different models can be quite different as revealed by the sizable intermodal spread in many of the prognostic variables. Enhanced model horizontal resolution (to 1/4°) fails to improve the mean state and the seasonal evolutions. This result emphasizes the need to improve the model physics as well as providing a realistic representation of bathymetry. The phase and strength of the IOD play an important role in modulating regional as well as global climate (Saji et al., 1999; Webster et al., 1999), with the seasonal evolution of the IOD sensitive to the representation of the model mean state. A recent study also shows a model's ability to capture the teleconnection to the positive IOD is closely related to its representation of the mean state (Hirons et al., 2018). Hence this study will give significant insight into the IOD climate mode and its prediction.

Recent studies by Li et al. (2016, 2017) noted that CMIP climate model projections of increased frequency of IOD events (Cai et al., 2014), increased ISMR, or a change in the mean state of the oceans are mostly artifacts of model errors that can significantly distort regional climate projections. Shikha and Valsala (2018) showed that over the Indian Ocean, CMIP5 models develop internal warm and saline biases approximately between a depth range of 100 m and 800 m in long term simulations, and these internal biases have implications in large scale ocean dynamics via their linkage through ocean baroclinicity. These studies suggest that the mean state and subsurface biases in the state-of-the-art coupled climate models can largely limit the model's skill for regional climate prediction. The present study showed that even in forced ocean/sea-ice climate models, the subsurface temperature and salinity biases are persistent, with particular examples being the

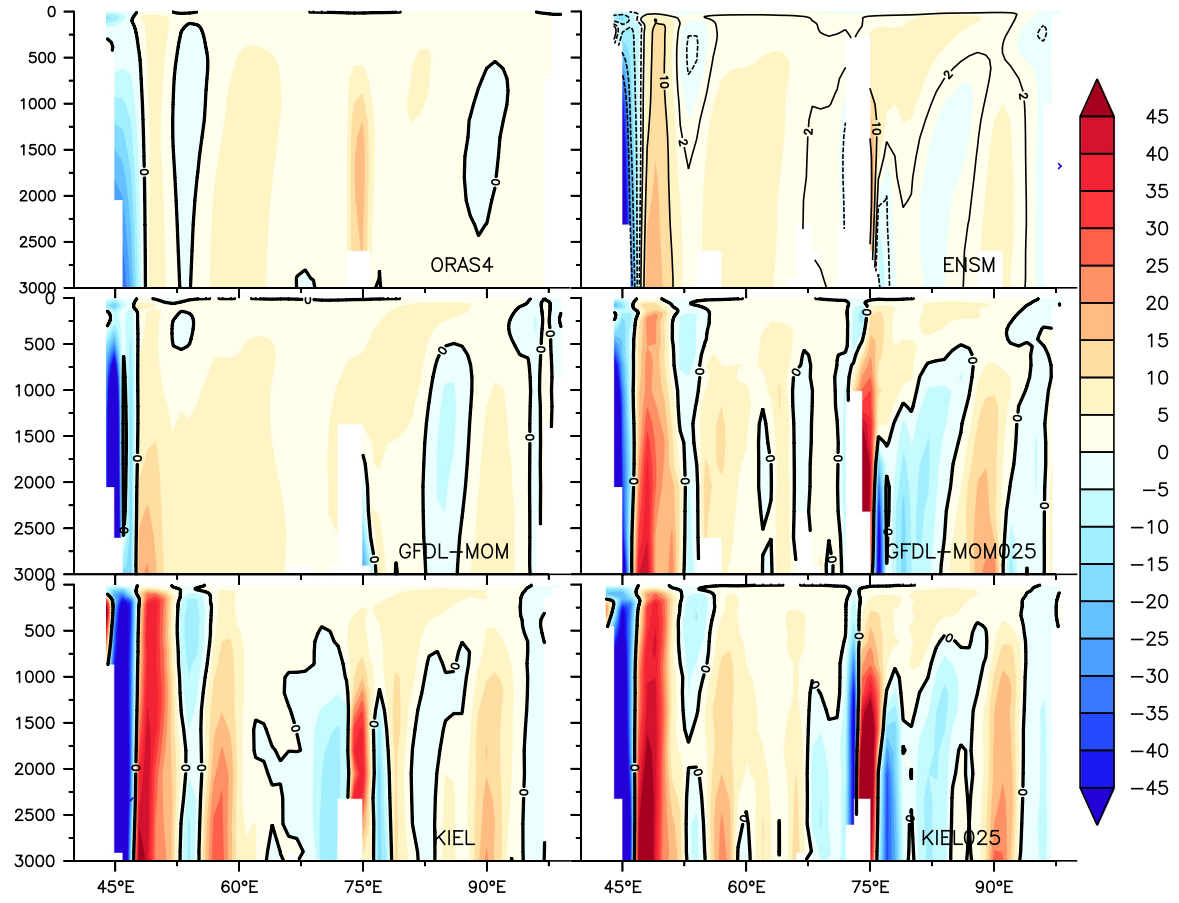


**Fig. 32a.** Transport across the equator from MOM, MOM025, KIEL, KIEL025, all model ensemble and ORAS4 in January. Units are in $m^2/s$.

thermocline temperature biases that result in the inability of these modes to realistically represent the subsurface mean state. Therefore, more focused research is needed to improve the model physics and the realistic representation of bathymetry in the development of future climate models.

## Declaration of competing interest

The authors declare that they have no known competing financial interests or personal relationships that could have appeared to influence the work reported in this paper.

## Acknowledgments

The encouragement and facilities provided by Dr. S S C Shenoi, Director, Indian National Centre for Ocean Information Services (INCOIS), are gratefully acknowledged. Graphics were generated using the NOAA product Ferret. We thank Prof. Raghu Murthugude for useful suggestions that greatly improved the manuscript. We thank N Kiran Kumar for his help to generate the schematic diagram in Fig. 1. The fourth author (J.V.D) acknowledges funding from the Helmholtz-Gemeinschaft and the GEOMAR Helmholtz Centre for Ocean Research Kiel (grant IV014/GH018). NCAR is a major facility sponsored by the U.S. National Science Foundation under Cooperative Agreement 1852977. Q. Wang and D. Sidorenko are supported by the German Helmholtz Climate Initiative REKLIM (Regional Climate Change). We thank Matthew Harrison and P S Swathi for their comments and discussions that have helped this paper. This is INCOIS contribution no. 358 and NCPOR contribution no. J-38/2019-20. We thank all five anonymous reviewers for their constructive comments by which we have improved the manuscript immensely.

## Appendix. Acronyms

ACCESS: Australian Community Climate and Earth System Simulator
AS: Arabian Sea
AWI: Alfred Wegener Institute
BoB: Bay of Bengal
BL: Barrier Layer
CEC: Cross-Equatorial Cell
CERFACS: Centre Européen de Recherche et de Formation AvancéeenCalculScientifique
CESM: Community Earth System Model
CGCM: Coupled general circulation model
CLIVAR: ClimateVariability and Predictability
CMCC: CentroEuro-MediterraneosuiCambiamentiClimatici
CMIP3: Coupled Model Intercomparison Project Phase 3
CMIP5: Coupled Model Intercomparison Project Phase 5
CNRM: Centre National de RecherchesMétéorologiques
CORE-II: Coordinated Ocean-ice Reference Experiments phase II
DRAKKAR: Coordination of high resolution global ocean simulations and developments of the NEMO modeling framework
EACC: East African Coastal Current
EEIO: Eastern Equatorial Indian Ocean
EICC: East India Coastal current
ENSO: *El Niño* Southern Oscillation
EUC: Equatorial Undercurrent
FSU: Florida State University
FSU2: Version2 of the FSU contribution
GFDL: Geophysical Fluid Dynamics Laboratory

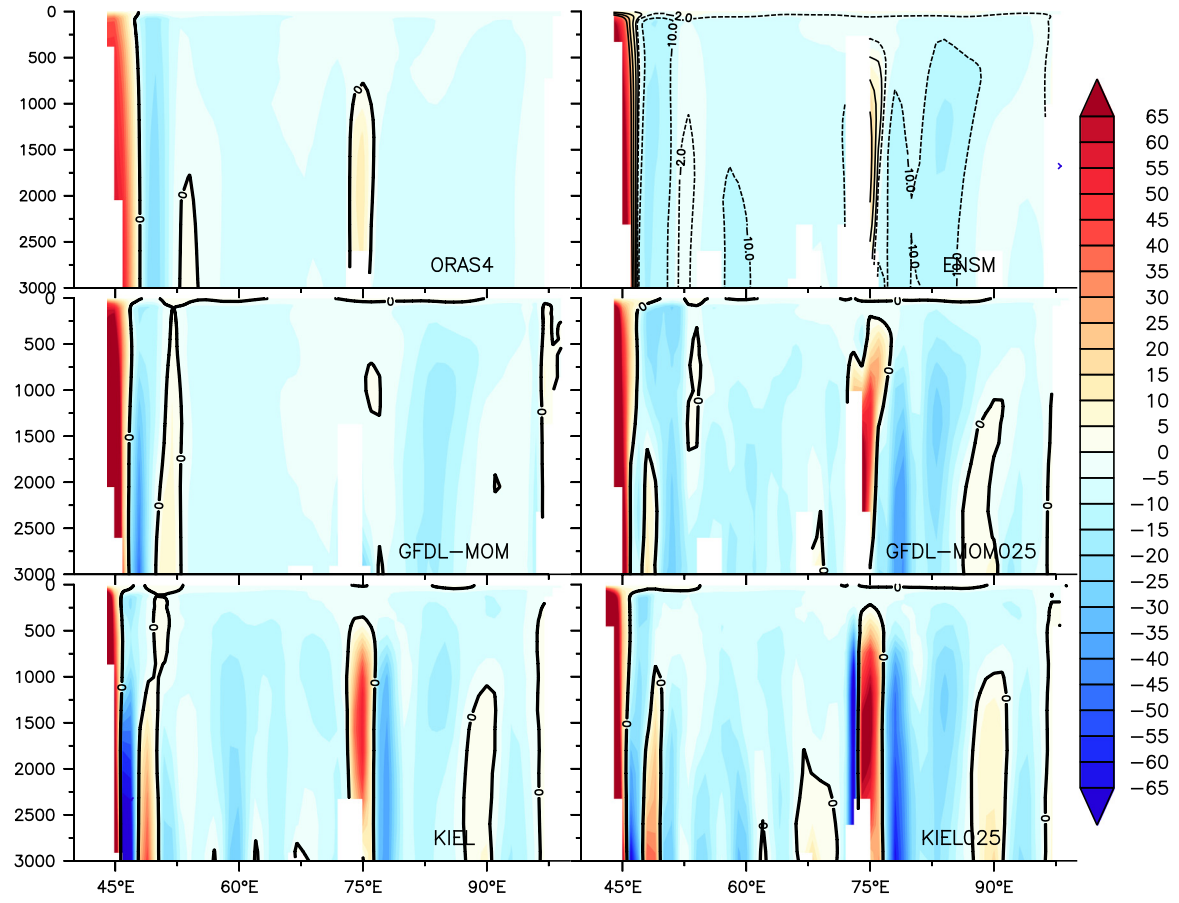


**Fig. 32b.** Transport across the equator from MOM, MOM025, KIEL, KIEL025, all model ensemble and ORAS4 in July. Units are in $m^2/s$.

GOLD: Generalized Ocean Layer Dynamics
GOOS: Global Ocean Observing System
HYCOM: Hybrid Coordinate Ocean Model
ICTP: International Centre for Theoretical Physics
IOC:Intergovernmental Oceanographic Commission
IOD: Indian Ocean Dipole
IODZM: Indian Ocean Dipole/Zonal mode
IOMOC: Indian Ocean Meridional overturning circulation
ISMR: Indian Summer Monsoon Rainfall
ITF: Indonesian through flow
ITCZ: Inter Tropical Convergence Zone
JRA55-do: Japanese 55-year atmospheric reanalysis (JRA-55) based surface dataset for driving ocean–sea-ice models (JRA55-do) (Tsujino et al., 2018)
KIEL: Contribution from the Helmholtz Center for Ocean Research, Kiel, Germany
KPP: K-Profile Parameterization (Large et al., 1994)
LHF: Latent heat flux
MLD: Mixed layer depth
MOC: Meridional overturning circulation
NMC: Northeast Monsoon Current
NHF: Net Heat Flux
NOAA: National Oceanic and Atmospheric Administration
NOCS: National Oceanography Centre Southampton
OSCAR: Ocean Surface Current Analysis
Qa: specific humidity
RAMA: Research Moored Array for African–Asian–Australian Monsoon Analysis & Prediction
RMSD: Root-mean-square deviation
SC: Somali current
SD: Standard deviation
SE: Socotra Eddy
SEAS: South Eastern Arabian Sea
SEC: South Equatorial Current
SG: Southern Gyre
SIO: Southern Indian Ocean
SICC: South Indian Ocean Counter Current
SMC: Southwest Monsoon Current
SSS: Sea surface salinity
SST: Sea surface temperature
SSTC: Southern Subtropical Cell
STC: Subtropical Cell
SWIO: Southwest Indian Ocean
Ta: Air temperature
TIO: Tropical Indian Ocean
TR: Thermocline Ridge
WICC: West India Coastal current
WJ: Wyrtki Jet
WOA: World Ocean Atlas

## References

Adcroft, A., Campin, J.-M., 2004. Rescaled height coordinates for accurate representation offree-surface flows in ocean circulation models. Ocean Model. 7, 269–284. http://dx.doi.org/10.1016/j.ocemod.2003.09.003.

Annamalai, H., Liu, P., Xie, S.-P., 2005. Southwest Indian Ocean SST variability: Its local effect and remote influence on Asian monsoons. J. Clim. 18, 4150–4167. http://dx.doi.org/10.1175/JCLI3533.1.

Annamalai, H., Murtugudde, R., 2004. Role of the Indian ocean in regional climate variability. In: Wang, C., Xie, S.P., Carton, J.A. (Eds.), Geophysical Monograph Series. American Geophysical Union, Washington, D. C., pp. 213–246. http://dx.doi.org/10.1029/147GM13.

Annamalai, H., Murtugudde, R., Potemra, J., Xie, S., Liu, P., Wang, B., 2003. Coupled dynamics over the Indian Ocean: spring initiation of the Zonal Mode. Deep Sea Res. Part II: Top. Stud. Oceanogr. 50, 2305–2330. http://dx.doi.org/10.1016/S0967-0645(03)00058-4.

Antonov, J.I., Seidov, D., Boyer, T.P., Locarnini, R.A., Mishonov, A.V., Garcia, H.E., 2010. World Ocean Atlas 2009 Volume 2: Salinity. S. Levitus, Ed. NOAA Atlas NESDIS 69. U.S. Government Printing Office, Washington, D.C, p. 184.

Atlas, R., Hoffman, R.N., Ardizzone, J., Leidner, S.M., Jusem, J.C., 2009. Development of a new cross-calibrated, multi-platform (CCMP) ocean surface wind product. In: Paper Presented at AMS 13th Conference on Integrated Observing and Assimilation Systems for Atmosphere, Oceans, and Land Surface (IOAS-AOLS). Phoenix, Ariz.

Balmaseda, M.A., Mogensen, K., Weaver, A.T., 2013. Evaluation of the ECMWF ocean reanalysis system ORAS4. Q.J.R. Meteorol. Soc. 139, 1132–1161. http://dx.doi.org/10.1002/qj.2063.

Beal, L.M., Donohue, K.A., 2013. The Great Whirl: Observations of its seasonal development and interannual variability: GREAT WHIRL. J. Geophys. Res. Oceans 118, 1–13. http://dx.doi.org/10.1029/2012JC008198.

Beal, L.M., Hormann, V., Lumpkin, R., Foltz, G.R., 2013. The response of the surface circulation of the Arabian Sea to monsoonal forcing. J. Phys. Oceanogr. 43, 2008–2022. http://dx.doi.org/10.1175/JPO-D-13-033.1.

Benshila, R., Durand, F., Masson, S., Bourdallé-Badie, R., de Boyer Montégut, C., Papa, F., Madec, G., 2014. The upper Bay of Bengal salinity structure in a high-resolution model. Ocean Model. 74, 36–52.

Berry, D.I., Kent, E.C., 2009. A new air–sea interaction gridded dataset from ICOADS with uncertainty estimates. Bull. Am. Meteorol. Soc. 90, 645–656. http://dx.doi.org/10.1175/2008BAMS2639.1.

Bhat, G.S., Vecchi, G.A., Gadgil, S., 2004. Sea surface temperature of the Bay of Bengal derived from TRMM microwave imager. J. Atmos. Ocean. Technol. 21, 1283–1290. http://dx.doi.org/10.1175/1520-0426(2004)021<1283:SSTOTB>2.0.CO;2.

Bonjean, F., Lagerloef, G.S.E., 2002. Diagnostic model and analysis of the surface currents in the tropical Pacific Ocean. J. Phys. Oceanogr. 32, 2938–2954. http://dx.doi.org/10.1175/1520-0485(2002)032<2938:DMAAOT>2.0.CO;2.

Boyer, T.P., Antonov, J.I., Baranova, O.K., Garcia, H.E., Johnson, D.R., Locarnini, R.A., Mishonov, A.V., O'Brien, T.D., Seidov, D., Smolyar, I.V., Zweng, M.M., 2009. World ocean database—2009. In: Levitus, S. (Ed.), NOAA Atlas, NESDIS 66. US Govt. Printing Office, Washington, DC.

Bray, N.A., Wijffels, S.E., Chong, J.C., Fieux, M., Hautala, S., Meyers, G., Morawitz, W.M.L., 1997. Characteristics of the Indo-Pacific throughflow in the eastern Indian Ocean. Geophys. Res. Lett. 24, 2569–2572. http://dx.doi.org/10.1029/97GL51793.

Brodeau, L., Barnier, B., Treguier, A.-M., Penduff, T., Gulev, S., 2010. An era40-based atmospheric forcing for global ocean circulation models. Ocean Model. 31, 88–104. http://dx.doi.org/10.1016/j.ocemod.2009.10.005.

Cai, W., Cowan, T., 2013. Why is the amplitude of the Indian Ocean Dipole overly large in CMIP3 and CMIP5 climate models? Geophys. Res. Lett. 40, 1200–1205.

Cai, W., Santoso, A., Wang, G., Weller, E., Wu, L., Ashok, K., Masumoto, Y., Yamagata, T., 2014. Increased frequency of extreme Indian Ocean Dipole events due to greenhouse warming. Nature 510, 254–258. http://dx.doi.org/10.1038/nature13327.

Cane, M.A., 1980. On the dynamics of equatorial currents, with application to the Indian Ocean. Deep Sea Res. Part A. Oceanogr. Res. Pap. 27, 525–544. http://dx.doi.org/10.1016/0198-0149(80)90038-2.

Chaudhari, H.S., Pokhrel, S., Saha, S.K., Dhakate, A., Yadav, R.K., Salunke, K., Mahapatra, S., Sabeerali, C.T., Rao, S.A., 2013. Model biases in long coupled runs of NCEP CFS in the context of Indian summer monsoon. Int. J. Clim. 33, 1057–1069. http://dx.doi.org/10.1002/joc.3489.

Chen, D., Busalacchi, A.J., Rothstein, L.M., 1994. The roles of vertical mixing, solar radiation, and wind stress in a model simulation of the sea surface temperature seasonal cycle in the tropical Pacific Ocean. J. Geophys. Res. 99 (20345), http://dx.doi.org/10.1029/94JC01621.

Chen, G., Han, W., Li, Y., Wang, D., McPhaden, M.J., 2015. Seasonal-to-interannual time-scale dynamics of the equatorial undercurrent in the Indian Ocean. J. Phys. Oceanogr. 45, 1532–1553. http://dx.doi.org/10.1175/JPO-D-14-0225.1.

Chen, Z., Wu, L., Qiu, B., Sun, S., Jia, F., 2014. Seasonal variation of the south equatorial current bifurcation off Madagascar. J. Phys. Oceanogr. 44, 618–631. http://dx.doi.org/10.1175/JPO-D-13-0147.1.

Chirokova, G., Webster, P.J., 2006. Interannual variability of Indian Ocean heat transport. J. Clim. 19, 1013–1031. http://dx.doi.org/10.1175/JCLI3676.1.

Chowdary, J.S., Parekh, A., Ojha, S., Gnanaseelan, C., 2015. Role of upper ocean processes in the seasonal SST evolution over tropical Indian Ocean in climate forecasting system. Clim. Dyn. 45, 2387–2405. http://dx.doi.org/10.1007/s00382-015-2478-4.

Chowdary, J.S., Parekh, A., Ojha, S., Gnanaseelan, C., Kakatkar, R., 2016. Impact of upper ocean processes and air-sea fluxes on seasonal SST biases over the tropical Indian Ocean in the NCEP Climate Forecasting System: Seasonal SST biases in the tropical Indian Ocean. Int. J. Clim. 36, 188–207. http://dx.doi.org/10.1002/joc.4336.

Colborn, J., 1975. The Thermal Structure of the Indian Ocean. The University Press, Hawaii, p. 173.

Cooper, N.S., 1988. The effect of salinity on tropical ocean models. J. Phys. Oceanogr. 18, 697–707.

Cutler, A.N., Swallow, J.C., 1984. Surface currents of the Indian Ocean, (to 25øS, 100øE), Vol. 187. Tech. Rep., Inst. of Oceanogr. Sci., Wormley, Godaiming, Surrey, England, p. 8, 36 charts.

Dai, A., Qian, T., Trenberth, K.E., Milliman, J.D., 2009. Changes in continental freshwater discharge from 1948 to 2004. J. Clim. 22, 2773–2792.

Danabasoglu, G., Yeager, S.G., Bailey, D., Behrens, E., Bentsen, M., Bi, D., Biastoch, A., Böning, C., Bozec, A., Canuto, V.M., Cassou, C., Chassignet, E., Coward, A.C., Danilov, S., Diansky, N., Drange, H., Farneti, R., Fernandez, E., Fogli, P.G., Forget, G., Fujii, Y., Griffies, S.M., Gusev, A., Heimbach, P., Howard, A., Jung, T., Kelley, M., Large, W.G., Leboissetier, A., Lu, J., Madec, G., Marsland, .S.J., Masina, S., Navarra, A., George Nurser, A.J., Pirani, A., y Mélia, D.S., Samuels, B.L., Scheinert, M., Sidorenko, D., Treguier, A.-M., Tsujino, H., Uotila, P., Valcke, S., Voldoire, A., Wang, Q., 2014. North Atlantic simulations in coordinated ocean-ice reference experiments phase II (CORE-II). Part I: Mean states. Ocean Model. 73, 76–107. http://dx.doi.org/10.1016/j.ocemod.2013.10.005.

Danabasoglu, G., Yeager, S.G., Kim, W.M., Behrens, E., Bentsen, M., Bi, D., Biastoch, A., Bleck, R., Böning, C., Bozec, A., Canuto, V.M., Cassou, C., Chassignet, E., Coward, A.C., Danilov, S., Diansky, N., Drange, H., Farneti, R., Fernandez, E., Fogli, P.G., Forget, G., Fujii, Y., Griffies, S.M., Gusev, A., Heimbach, P., Howard, A., Ilicak, M., Jung, T., Karspeck, A.R., Kelley, M., Large, W.G., Leboissetier, A., Lu, J., Madec, G., Marsland, .S.J., Masina, S., Navarra, A., Nurser, A.J.G., Pirani, A., Romanou, A., Salas y Mélia, D., Samuels, B.L., Scheinert, M., Sidorenko, D., Sun, S., Treguier, A.-M., Tsujino, H., Uotila, P., Valcke, S., Voldoire, A., Wang, Q., Yashayaev, I., 2016. North Atlantic simulations in Coordinated Ocean-ice Reference Experiments phase II (CORE-II). Part II: Inter-annual to decadal variability. Ocean Model. 97, 65–90. http://dx.doi.org/10.1016/j.ocemod.2015.11.007.

Dee, D.P., Uppala, S.M., Simmons, A.J., Berrisford, P., Poli, P., Kobayashi, S., Andrae, U., Balmaseda, M.A., Balsamo, G., Bauer, P., Bechtold, P., Beljaars, A.C.M., van de Berg, L., Bidlot, J., Bormann, N., Delsol, C., Dragani, R., Fuentes, M., Geer, A.J., Haimberger, L., Healy, S.B., Hersbach, H., Hólm, E.V., Isaksen, L., Kållberg, P., Köhler, M., Matricardi, M., McNally, A.P., Monge-Sanz, B.M., Morcrette, J.-J., Park, B.-K., Peubey, C., de Rosnay, P., Tavolato, C., Thépaut, J.-N., Vitart, F., 2011. The ERA-interim reanalysis: configuration and performance of the data assimilation system. Quart. J. R. Meteorol. Soc 137, 553–597. http://dx.doi.org/10.1002/qj.828.

Du, Y., Qu, T., Meyers, G., Masumoto, Y., Sasaki, H., 2005. Seasonal heat budget in the mixed layer of the southeastern tropical Indian ocean in a high-resolution ocean general circulation model. J. Geophys. Res. 110 (C04012), http://dx.doi.org/10.1029/2004JC002845.

Durand, F., Papa, F., Rahman, A., Bala, S.K., 2011. Impact of Ganges–Brahmaputra interannual discharge variations on Bay of Bengal salinity and temperature during 1992–1999 period. J. Earth Syst. Sci 120, 859–872. http://dx.doi.org/10.1007/s12040-011-0118-x.

Durand, F., Shetye, S.R., Vialard, J., Shankar, D., Shenoi, S.S.C., Ethe, C., Madec, G., 2004. Impact of temperature inversions on SST evolution in the South-Eastern Arabian Sea during the pre-summer monsoon season. Geophys. Res. Lett. 31 (L01305), http://dx.doi.org/10.1029/2003GL018906.

Durgadoo, J.V., Ruhs, S., Biastoch, A., Boning, C.W.B., 2017. Indian ocean sources of Agulhas leakage. J. Geophys. Res. Oceans 122, 3481–3499. http://dx.doi.org/10.1002/2016JC012676.

Eyring, V., Bony, S., Meehl, G.A., Senior, C.A., Stevens, B., Stouffer, R.J., Taylor, K.E., 2016. Overview of the Coupled Model Intercomparison Project Phase 6 (CMIP6) experimental design and organization. Geosci. Model Dev. 9, 1937–1958. http://dx.doi.org/10.5194/gmd-9-1937-2016.

Farneti, R., Downes, S.M., Griffies, S.M., Marsland, .S.J., Bailey, D., Behrens, E., Bentsen, M., Bi, D., Biastoch, A., Boning, C., Bozec, A., Chassignet, E., Danabasoglu, G., Danilov, S., Diansky, N., Drange, H., Fogli, P.G., Gusev, A., Hallberg, R.W., Howard, A., Kelley, M., Illicak, M., Large, W.G., Leboissetier, A., Long, M., Lu, J., Masina, S., Mishra, A., Navarra, A., Nurser, A.J.G., Patara, L., Samuels, B.L., Sidorenko, D., Tsujino, H., Uotila, P., Yeager, S.G., Wang, Q., 2015. An assessment of antarctic circumpolar current and southern ocean meridional overturning circulation during 1958–2007 in a suite of interannual CORE-II simulations. Ocean Model. http://dx.doi.org/10.1016/j.ocemod.2015.07.009.

Fasullo, J., Webster, P.J., 1999. Warm pool SST variability in relation to the surface energy balance. J. Clim. 12, 1292–1305. http://dx.doi.org/10.1175/1520-0442(1999)012<1292:WPSVIR>2.0.CO;2.

Fathrio, I., Iizuka, S., Manda, A., Kodama, Y.-M., Ishida, S., Moteki, Q., Yamada, H., Tachibana, Y., 2017a. Assessment of western Indian ocean SST bias of cmip5 models: Western Indian ocean SST bias of CMIP5. J. Geophys. Res. Oceans 122, 3123–3140. http://dx.doi.org/10.1002/2016JC012443.

Fathrio, I., Manda, A., Iizuka, S., Kodama, Y.-M., Ishida, S., 2017b. Evaluation of CMIP5 models on sea surface salinity in the Indian Ocean. IOP Conf. Ser.: Earth Environ. Sci. 54, 012039. http://dx.doi.org/10.1088/1755-1315/54/1/012039.

Flato, G., Marotzke, J., Abiodun, B., Braconnot, P., Chou, S.C., Collins, W., Cox, P., Driouech, F., Emori, S., Eyring, V., Forest, C., Gleckler, P., Guilyardi, E., Jakob, C., Kattsov, V., Reason, C., Rummukainen, M., 2013. Evaluation of climate models. In: Stocker, T.F., Qin, D., Plattner, G.-K., Tignor, M., Allen, S.K., Boschung, J., Nauels, A., Xia, Y., Bex, V., Midgley, P.M. (Eds.), Limate Change 2013: The Physical Science Basis. Contribution of Working Group I To the Fifth Assessment Report of the Intergovernmental Panel on Climate Change. Cambridge University Press, Cambridge, United Kingdom and New York, NY, USA.

Gadgil, S., 2003. The Indian monsson and its variability. Annu. Rev. Earth Planet. Sci 31, 429–467. http://dx.doi.org/10.1146/annurev.earth.31.100901.141251.

Gadgil, S., Joseph, P.V., Joshi, N.V., 1984. Ocean–atmosphere coupling over monsoon regions. Nature 312, 141–143. http://dx.doi.org/10.1038/312141a0.

Gadgil, S., Rajeevan, M., Nanjundiah, R., 2005. Monsoon prediction – why yet another failure? Current Sci. 88 (12).

Garternicht, U., Schott, F., 1997. Heat fluxes of the Indian ocean from a global eddy-resolving model. J. Geophys. Res. Oceans 102, 21147–21159. http://dx.doi.org/10.1029/97JC01585.

Girishkumar, M.S., Ravichandran, M., McPhaden, M.J., Rao, R.R., 2011. Intraseasonal variability in barrier layer thickness in the south central Bay of Bengal. J. Geophys. Res 116, http://dx.doi.org/10.1029/2010JC006657.

Godfrey, J.S., 1996. The effect of the Indonesian throughflow on ocean circulation and heat exchange with the atmosphere: A review. J. Geophys. Res. Oceans 101, 12217–12237. http://dx.doi.org/10.1029/95JC03860.

Godfrey, J.S., Hu, R.-J., Schiller, A., Fiedler, R., 2007. Explorations of the annual mean heat budget of the tropical Indian Ocean. Part I: Studies with an idealized model. J. Clim. 20, 3210–3228. http://dx.doi.org/10.1175/JCLI4157.1.

Gordon, A.L., Fine, R.A., 1996. Pathways of water between the Pacific and Indian oceans in the Indonesian seas. Nature 379, 146–149. http://dx.doi.org/10.1038/379146a0.

Gordon, A.L., Sprintall, J., Van Aken, H.M., Susanto, D., Wijffels, S., Molcard, R., Ffield, A., Pranowo, W., Wirasantosa, S., 2010. The Indonesian throughflow during 2004–2006 as observed by the INSTANT program. Dyn. Atmos. Oceans 50, 115–128. http://dx.doi.org/10.1016/j.dynatmoce.2009.12.002.

Graham, N.E., Barnett, T.P., 1987. Sea surface temperature surface wind divergence and convection over tropical oceans. Science 238, 657–659.

Griffies, S.M., 2009. Elements of MOM4p1, Vol. 6. GFDL Ocean Group Tech. Rep., p. 377, [Available online at http://data1.gfdl.noaa.gov/~arl/pubrel/o/old/doc/mom4p1_guide.pdf].

Griffies, S.M., Biastoch, A., Böning, C., Bryan, F., Danabasoglu, G., Chassignet, E.P., England, .M.H., Gerdes, R., Haak, H., Hallberg, R.W., Hazeleger, W., Jungclaus, J., Large, W.G., Madec, G., Pirani, A., Samuels, B.L., Scheinert, M., Gupta, A.S., Severijns, C.A., Simmons, H.L., Treguier, A.M., Winton, M., Yeager, S., Yin, J., 2009. Coordinated ocean-ice reference experiments (COREs). Ocean Model. 26, 1–46. http://dx.doi.org/10.1016/j.ocemod.2008.08.007.

Griffies, S.M., Danabasoglu, G., Durack, P.J., Adcroft, A.J., Balaji, V., Böning, C.W., Chassignet, E.P., Curchitser, E., Deshayes, J., Drange, H., Fox-Kemper, B., Gleckler, P.J., Gregory, J.M., Haak, H., Hallberg, R.W., Hewitt, H.T., Holland, D.M., Ilyina, T., Jungclaus, J.H., Komuro, Y., Krasting, J.P., Large, W.G., Marsland, S.J., Masina, S., McDougall, T.J., Nurser, A.J.G., Orr, J.C., Pirani, A., Qiao, F., Stouffer, R.J., Taylor, K.E., Treguier, A.M., Tsujino, H., Uotila, P., Valdivieso, M., Winton, M., Yeager, S.G., 2016. Experimental and diagnostic protocol for the physical component of the CMIP6 Ocean Model Intercomparison Project (OMIP). Geosci. Model Dev. Discuss. 1–108. http://dx.doi.org/10.5194/gmd-2016-77.

Griffies, S.M., Pacanowski, R.C., Hallberg, R.W., 2000. Spurious diapycnal mixing associated with advection in a z -coordinate ocean model. Mon. Weather Rev. 128, 538–564. http://dx.doi.org/10.1175/1520-0493(2000)128<0538:SDMAWA>2.0.CO;2.

Griffies, S.M., Yin, J., Durack, P.J., Goddard, P., Bates, S.C., Behrens, E., Bentsen, M., Bi, D., Biastoch, A., Böning, C.W., Bozec, A., Chassignet, E., Danabasoglu, G., Danilov, S., Domingues, C.M., Drange, H., Farneti, R., Fernandez, E., Greatbatch, R.J., Holland, D.M., Ilicak, M., Large, W.G., Lorbacher, K., Lu, J., Marsland, .S.J., Mishra, A., George Nurser, A.J., Salas y Mélia, D., Palter, J.B., Samuels, B.L., Schröter, J., Schwarzkopf, F.U., Sidorenko, D., Treguier, A.M., Tseng, Y., Tsujino, H., Uotila, P., Valcke, S., Voldoire, A., Wang, Q., Winton, M., Zhang, X., 2014. An assessment of global and regional sea level for years 1993–2007 in a suite of interannual CORE-II simulations. Ocean Model. 78, 35–89. http://dx.doi.org/10.1016/j.ocemod.2014.03.004.

Halkides, D.J., Lee, T., 2009. Mechanisms controlling seasonal-to-interannual mixed layer temperature variability in the southeastern tropical Indian Ocean. J. Geophys. Res. Oceans 114 (C02012), http://dx.doi.org/10.1029/2008JC004949.

Han, W., McCreary, J.P., 2001. Modeling salinity distributions in the Indian Ocean. J. Geophys. Res. Oceans 106, 859–877. http://dx.doi.org/10.1029/2000JC000316.

Han, W., McCreary, J.P., Kohler, K.E., 2001. Influence of precipitation minus evaporation and Bay of Bengal rivers on dynamics, thermodynamics, and mixed layer physics in the upper Indian Ocean. J. Geophys. Res. Oceans 106, 6895–6916. http://dx.doi.org/10.1029/2000JC000403.

Han, W., Vialard, J., McPhaden, M.J., Lee, T., Masumoto, Y., Feng, M., de Ruijter, W.P.M., 2014. Indian ocean decadal variability: A review. Bull. Am. Meteorol. Soc. 95, 1679–1703. http://dx.doi.org/10.1175/BAMS-D-13-00028.1.

Haney, R.L., 1971. Surface thermal boundary conditions for ocean circulation models. J. Phys. Oceanogr. 1, 241–248.

Hirons, L., Turner, A, 2018. The impact of Indian Ocean mean-state biases in climate models on the representation of the East African short rains. J. Clim. 31 (16), 6611–6631. http://dx.doi.org/10.1175/JCLI-D-17-0804.1.

Horii, T., Mizuno, K., Nagura, M., Miyama, T., Ando, K., 2013. Seasonal and interannual variation in the cross- equatorial meridional currents observed in the eastern Indian Ocean. J. Geophys. Res. Oceans 118, http://dx.doi.org/10.1002/2013JC009291.

Howden, S.D., Murtugudde, R., 2001. Effects of river inputs into the Bay of Bengal. J. Geophys. Res. Oceans 106, 19825–19843. http://dx.doi.org/10.1029/2000JC000656.

Huang, B., Kinter III, J.L., 2002. Interannual variability in the tropical Indian Ocean. J. Geophys. Res. 107 (C11), 3199. http://dx.doi.org/10.1029/2001JC001278.

Ilıcak, M., Adcroft, A.J., Griffies, S.M., Hallberg, R.W., 2012. Spurious dianeutral mixing and the role of momentum closure. Ocean Model. 45–46, 37–58. http://dx.doi.org/10.1016/j.ocemod.2011.10.003.

Ilicak, M., Drange, H., Q., Wang., Gerdes, R., Aksenov, Y., Bailey, D., Bentsen, M., Biastoch, A., Bozec, A., Böning, C., Cassou, C., Chassignet, E., Coward, A.C., Curry, B., Danabasoglu, G., Danilov, S., Fernandez, E., Fogli, P.G., Fujii, Y., Griffies, S.M., Iovino, D., Jahn, A., Jung, T., Large, W.G., Lee, C., Lique, C., Jianhua, L., Simona, M.A.J., Nurser, G., Roth, C., David, S.Y., Mlia, B.L., Samuels, P.S., Tsujino, H., Valcke, S., Voldoire, A., Wang, X., Yeager, S.G., 2016. An assessment of the arctic ocean in a suite of interannual core-II simulations. Part III: Hydrography and fluxes. Ocean Model. 100, 141–161. http://dx.doi.org/10.1016/j.ocemod.2016.02.004.

Iskandar, I., Masumoto, Y., Mizuno, K., 2009. Subsurface equatorial zonal current in the eastern Indian Ocean. J. Geophys. Res. 114, http://dx.doi.org/10.1029/2008JC005188.

Jensen, T.G., 2001. Arabian Sea and Bay of Bengal exchange of salt and tracers in an ocean model. Geophys. Res. Lett. 28, 3967–3970. http://dx.doi.org/10.1029/2001GL013422.

Jensen, T.G., 2003. Cross-equatorial pathways of salt and tracers from the northern Indian Ocean: Modelling results. Deep Sea Res. Part II: Top. Stud. Oceanogr. 50, 2111–2127. http://dx.doi.org/10.1016/S0967-0645(03)00048-1.

Jensen, T.G., 2007. Wind-driven response of the northern Indian Ocean to climate extremes. J. Clim. 20, 2978–2993. http://dx.doi.org/10.1175/JCLI4150.1.

Joseph, P.V., 1990. Warm pool in the Indian Ocean and monsoon onset. Trop. Ocean Atmos. News Lett. 53, 1–5.

Joseph, P.V., Sooraj, K.P., Rajan, C.K., 2006. The summer monsoon onset process over South Asia and an objective method for the date of monsoon onset over Kerala. Int. J. Climatol. 26, 1871–1893. http://dx.doi.org/10.1002/joc.1340.

Kara, A.B., Rochford, P.A., Hurlburt, H.E., 2000. An optimal definition for ocean mixed layer depth. J. Geophys. Res. Oceans 105, 16803–16821. http://dx.doi.org/10.1029/2000JC900072.

Karmakar, A., Parekh, A., Chowdary, J.S., Gnanaseelan, C., 2017. Inter comparison of Tropical Indian Ocean features in different ocean reanalysis products. Clim. Dyn. 1–23. http://dx.doi.org/10.1007/s00382-017-3910-8.

Klein, S.A., Soden, B.J., Lau, N.-C., 1999. Remote sea surface temperature variations during ENSO: Evidence for a tropical atmospheric bridge. J. Clim. 12, 917–932. http://dx.doi.org/10.1175/1520-0442(1999)012<0917:RSSTVD>2.0.CO;2.

Knox, R.A., 1976. On a long series of measurements of Indian Ocean equatorial currents near Addu Atoll. Deep Sea Res. Oceanogr. Abstr. 23, 211–IN1. http://dx.doi.org/10.1016/0011-7471(76)91325-5.

Knox, R.A., 1981. Time variability of Indian ocean equatorial currents. Deep Sea Res. Part A. Oceanogr. Res. Pap. 28, 291–295. http://dx.doi.org/10.1016/0198-0149(81)90068-6.

Kobayashi, S., Ota, Y., Harada, Y., Ebita, A., Moriya, M., Onoda, H., Onogi, K., Kamahori, H., Kobayashi, C., Endo, H., Miyaoka, K., Takahashi, K., 2015. The JRA-55 reanalysis: General specifications and basic characteristics. J. Meteor. Soc. Japan 93, 5–48. http://dx.doi.org/10.2151/jmsj.2015-001.

Kurian, J., Vinayachandran, P.N., 2007. Mechanisms of formation of the Arabian Sea mini warm pool in a high-resolution Ocean General Circulation Model. J. Geophys. Res. 112, http://dx.doi.org/10.1029/2006JC003631.

Large, W.G., McWilliams, J.C., Doney, S.C., 1994. Oceanic vertical mixing: a review and a model with a nonlocal boundary layer parameterization. Rev. Geophys. 32 (4), 363–403.

Large, W., Yeager, S., 2004. Diurnal to Decadal Global Forcing for Ocean and Sea Ice Models: The Data Sets and Climatologies. Technical Report TN-460+STR, NCAR, p. 105.

Large, W.G., Yeager, S.G., 2009. The global climatology of an interannually varying air–sea flux data set. Clim. Dyn. 33, 341–364. http://dx.doi.org/10.1007/s00382-008-0441-3.

Lau, N.-C., Nath, M.J., 2004. Coupled GCM simulation of atmosphere-ocean variability associated with zonally asymmetric SST changes in the tropical Indian Ocean. J. Clim. 17, 245–265.

Lee, T., 2004. Decadal weakening of the shallow overturning circulation in the South Indian Ocean. Geophys. Res. Lett. 31, http://dx.doi.org/10.1029/2004GL020884.

Lee, T., Marotzke, J., 1997. Inferring meridional mass and heat transports of the Indian Ocean by fitting a general circulation model to climatological data. J. Geophys. Res. Oceans 102, 10585–10602. http://dx.doi.org/10.1029/97JC00464.

Lee, T., Marotzke, J., 1998. Seasonal cycles of meridional overturning and heat transport of the Indian Ocean. J. Phys. Oceanogr. 28, 923–943. http://dx.doi.org/10.1175/1520-0485(1998)028<0923:SCOMOA>2.0.CO;2.

Lee, J.-Y., Wang, B., Kang, I.-S., Shukla, J., Kumar, A., Kug, J.-S., Schemm, J.K.E., Luo, J.-J., Yamagata, T., Fu, X., Alves, O., Stern, B., Rosati, T., Park, C.-K., 2010. How are seasonal prediction skills related to models' performance on mean state and annual cycle? Clim. Dyn 35, 267–283. http://dx.doi.org/10.1007/s00382-010-0857-4.

Legg, S., Briegleb, B., Chang, Y., Chassignet, E.P., Danabasoglu, G., Ezer, T., Gordon, A.L., Griffies, S., Hallberg, R., Jackson, L., Large, W., Özgökmen, T.M., Peters, H., Price, J., Riemenschneider, U., Wu, W., Xu, X., Yang, J., 2009. Improving Oceanic Overflow Representation in Climate Models. the Gravity Current Entrainment Climate Process Team. American Meteorological Society, Washington, DC, pp. 657–670.

Levine, R.C., Turner, A.G., 2012. Dependence of Indian monsoon rainfall on moisture fluxes across the Arabian Sea and the impact of coupled model sea surface temperature biases. Clim. Dyn. 38, 2167–2190. http://dx.doi.org/10.1007/s00382-011-1096-z.

Levine, R.C., Turner, A.G., Marathayil, D., Martin, G.M., 2013. The role of northern Arabian Sea surface temperature biases in cmip5 model simulations and future projections of Indian summer monsoon rainfall. Clim. Dyn. 41, 155–172. http://dx.doi.org/10.1007/s00382-012-1656-x.

Levitus, S., 1983. Climatological atlas of the world ocean. EOS Trans. Am. Geophys. Union 64, 962. http://dx.doi.org/10.1029/EO064i049p00962-02.

Levitus, S., 1987. A comparison of the annual cycle of two sea surface temperature climatology of the world ocean.

Li, G., Xie, S.-P., Du, Y., 2015. Monsoon-induced biases of climate models over the Tropical Indian Ocean. J. Clim. 28, 3058–3072. http://dx.doi.org/10.1175/JCLI-D-14-00740.1.

Li, G., Xie, S.-P., Du, Y., 2016. A robust but spurious pattern of climate change in model projections over the Tropical Indian Ocean. J. Clim. 29, 5589–5608. http://dx.doi.org/10.1175/JCLI-D-15-0565.1.

Li, G., Xie, S.P., He, C., Chen, Z., 2017. Western Pacific emergent constraint lowers projected increase in Indian summer monsoon rainfall. Nature Clim. Change 7, 708–712. http://dx.doi.org/10.1038/nclimate3387.

Li, T., Zhang, Y., Chang, C.-P., Wang, Bin, 2001. On the relationship between Indian Ocean SST and Asian summer monsoon. Geophys. Res. Lett. 28, 2843–2846. http://dx.doi.org/10.1029/2000GL011847.

Locarnini, R.A., Mishonov, A.V., Antonov, J.I., Boyer, T.P., Garcia, H.E., 2010. In: Levitus, S. (Ed.), World Ocean Atlas 2009, Volume 1: Temperature. NOAA Atlas NESDIS 68, U.S. Government Printing Office, Washington, D.C., p. 184.

Lumpkin, R., Johnson, G.C., 2013. Global ocean surface velocities from drifters: Mean, variance, El Niño-Southern Oscillation response, and seasonal cycle: Global Ocean Surface Velocities. J. Geophys. Res. Oceans 118, 2992–3006. http://dx.doi.org/10.1002/jgrc.20210.

Lutjeharms, J.R.E., 2006. The Agulhas Current. Springer-Verlag, Berlin Heidelberg, p. 329.

Marathayil, D., Turner, A.G., Shaffrey, L.C., Levine, R.C., 2013. Systematic winter sea-surface temperature biases in the northern Arabian Sea in HiGEM and the CMIP3 models. Environ. Res. Lett. 8, 014028. http://dx.doi.org/10.1088/1748-9326/8/1/014028.

Masson, S., Delecluse, P., Boulanger, J.-P., Menkes, C., 2002. A model study of the seasonal variability and formation mechanisms of the barrier layer in the eastern equatorial Indian Ocean: barrier layer in the eastern Indian Ocean. J. Geophys. Res. Oceans 107, SRF 18–1–SRF 18–20. http://dx.doi.org/10.1029/2001JC000832.

Masson, S., Luo, J.-J., Madec, G., Vialard, J., Durand, F., Gualdi, S., Guilyardi, E., Behera, S., Delecluse, P., Navarra, A., Yamagata, T., 2005. Impact of barrier layer on winter-spring variability of the southeastern Arabian Sea: barrier layer impact on the southeastern Arabian Sea. Geophys. Res. Lett. 32, n/a–n/a. http://dx.doi.org/10.1029/2004GL021980.

McCreary, J.P., Kohler, K.E., Hood, R.R., Smith, S., Kindle, J., Fischer, A.S., Weller, R.A., 2001. Influences of diurnal and intraseasonal forcing on mixed-layer and biological variability in the central Arabian Sea. J. Geophys. Res. Oceans 106, 7139–7155. http://dx.doi.org/10.1029/2000JC900156.

McCreary, J.P., Kundu, P.K., Molinari, R.L., 1993. A numerical investigation of dynamics, thermodynamics and mixed-layer processes in the Indian Ocean. Prog. Oceanogr. 31, 181–244. http://dx.doi.org/10.1016/0079-6611(93)90002-U.

McPhaden, M.J., 1986. The equatorial undercurrent: 100 years of discovery. Eos. Trans. Amer. Geophys. Union 67, 762. http://dx.doi.org/10.1029/EO067i040p00762.

McPhaden, M.J., Wang, Y., Ravichandran, M., 2015. Volume transports of the Wyrtki jets and their relationship to the Indian Ocean Dipole: WYRTKI JET TRANSPORTS. J. Geophys. Res. Oceans 120, 5302–5317. http://dx.doi.org/10.1002/2015JC010901.

McWilliams, J.C., 1996. Modeling the Oceanic general circulation. Annu. Rev. Fluid Mech. 28 (1), 215–248.

Mignot, J., de Boyer Montégut, C., Lazar, A., Cravatte, S., 2007. Control of salinity on the mixed layer depth in the world ocean: 2. Tropical areas. J. Geophys. Res. 112, http://dx.doi.org/10.1029/2006JC003954.

Miller, J.R., 1976. The salinity effect in a mixed layer ocean model. J. Phys. Oceanogr. 6, 29–35.

Miyama, T., McCreary, Jr., J.P., Jensen, T.G., Loschnigg, J., Godfrey, J.S., Ishida, A., 2003. Structure and dynamics of the Indian-Ocean cross equatorial cell. Deep. Sea Res. 50, 2023–2047.

Momin, I.M., Mitra, A.K., Mahapatra, D.K., Gera, A., Rajagopal, E.N., 2014. Impact of model resolutions on Indian ocean simulations from Global NEMO Ocean Model. Ind. J. Geo-Mar. Sc. 43 (09), 1667–1674.

deBoyer Montégutet, C., Vialard, J., Shenoi, S.S.C., Shankar, D., Durand, F., Ethé, C., Madec, G., 2007. Simulated seasonal and interannual variability of mixed layer heat budget in the northern Indian Ocean. J. Clim. 20, 3249–3268.

Moshonkin, S.M., Harenduprakash, L., 1991. Effect of salinity and transparency on the mixed layer thermal structure in the Bay of Bengal. Oceanology 31, 384–394.

Murtugudde, R., Busalacchi, A.J., 1999. Interannual variability of the dynamics and thermodynamics of the tropical Indian ocean. J. Clim. 12, 2300–2326. http://dx.doi.org/10.1175/1520-0442(1999)012<2300:IVOTDA>2.0.CO;2.

Murtugudde, R., Busalacchi, A.J., Beauchamp, J., 1998. Seasonal-to-interannual effects of the Indonesian throughflow on the tropical Indo-Pacific Basin. J. Geophys. Res. Oceans 103, 21425–21441. http://dx.doi.org/10.1029/98JC02063.

Murtugudde, R., Seager, R., Busalacchi, A., 1996. Simulation of the Tropical Oceans with an ocean GCM coupled to an atmospheric mixed layer model. J. Clim. 9, 1795–1815.

Murty, V.S., Sarma, Y.V., Babu, M.T., Rao, D.P., 1992. Hydrography and circulation in the northwestern Bay of Bengal during the retreat of southwest monsoon. J. Earth Syst. Sci. 101, 67–75.

Nagura, M., Masumoto, Y., 2015. A wake due to the Maldives in the eastward Wyrtki jet. J. Phys. Oceanogr. 45, 1858–1876.

Nagura, M., Sasaki, W., Tozuka, T., Luo, J.-J., Behera, S.K., Yamagata, T., 2013. Longitudinal biases in the Seychelles Dome simulated by 35 ocean-atmosphere coupled general circulation models. J. Geophys. Res. Oceans 118, http://dx.doi.org/10.1029/2012JC008352.

Narapusetty, B., Murtugudde, R., Wang, H., Kumar, A., 2015. Ocean–atmosphere processes driving Indian summer monsoon biases in CFSv2 hindcasts. Clim. Dyn. http://dx.doi.org/10.1007/s00382-015-2910-9.

Nauw, J.J., van Aken, H.M., Webb, A., Lutjeharms, J.R.E., de Ruijter, W.P.M., 2008. Observations of the southern East Madagascar Current and undercurrent and countercurrent system. J. Geophys. Res. 113 (C08006), http://dx.doi.org/10.1029/2007JC004639.

Oberhuber, J.M., 1988. An atlas based on the COADS data set: The budgets of heat buoyancy and turbulent kinetic energy at the surface of the global ocean. Max-Planck-Institut Fur Meteorologie Tech. Rep, 15, Bundesstrasse 55, 20146 Hamburg, Germany, p. 20, Available from Max-Planck-Institutfu r Meteorologie.

Palastanga, V., van Leeuwen, P., de Ruijter, W., 2006. A link between low-frequency mesoscale eddy variability around Madagascar and the large-scale Indian Ocean variability. J. Geophys. Res. 111, C09. http://dx.doi.org/10.1029/2005JC003081, 029.

Palastanga, V., van Leeuwen, P.J., Schouten, M.W., de Ruijter, W.P.M., 2007. Flow structure and variability in the subtropical Indian Ocean: Instability of the South Indian Ocean Countercurrent. J. Geophys. Res. 112, C01001. http://dx.doi.org/10.1029/2005JC003395.

Parampil, S., Bharathraj, G.N., Harrison, M., Sengupta, D., 2016. Observed subseasonal variability of heat flux and the SST response of the tropical Indian Ocean. J. Geophys. Res. Oceans 121, 7290–7307. http://dx.doi.org/10.1002/2016JC011948.

Parekh, A., Gnanaseelan, C., Jayakumar, A., 2011. Impact of improved momentum transfer coefficients on the dynamics and thermodynamics of the north Indian Ocean. J. Geophys. Res. 116, C01004. http://dx.doi.org/10.1029/2010JC006346.

Perez-Hernandez, M.D., Hernandez-Guerra, A., Joyce, T.M., Velez-Belchi, P., 2012. Wind-driven cross-equatorial flow in the Indian Ocean. J. Phys. Oceanogr. 42, 2234–2253.

Perigaud, C., McCreary, J.P., Zhang, K.Q., 2003. Impact of interannual rainfall anomalies on Indian Ocean salinity and temperature variability. J. Geophys. Res. Oceans 108 (C10), 3319. http://dx.doi.org/10.1029/2002JC001699.

Philander, S.G.H., 1973. Equatorial undercurrent: Measurements and theories. Rev. Geophys. 11 (3), 513–570. http://dx.doi.org/10.1029/RG011i003p00513.

Philander, S.G.H., Pacanowski, R.C., 1980. The generation of equatorial currents. J. Geophys. Res. 85, 1123–1136.

Pokhrel, S., Chaudhari, H.S., Saha, S.K., Dhakate, A., Yadav, R.K., Salunke, K., Mahapatra, S., Rao, S.A., 2012a. ENSO, IOD and Indian summermonsoon in NCEP climate forecast system. Clim. Dyn. 1–23. http://dx.doi.org/10.1007/s00382-012-1349-5.

Pokhrel, S., Rahaman, H., Parekh, A., Saha, S.K., Dhakate, A., Chaudhari, H.S., Gairola, R.M., 2012b. Evaporation–precipitation variability over Indian Ocean and its assessment in NCEP Climate Forecast System (CFSv2). Clim. Dyn. 39, 2585–2608.

Pokhrel, S., Saha, S.K., Dhakate, A., Chaudhari, H.S., Salunke, K., Rahman, H., Krishna, S., Hazra, A., Sikka, D.R., 2016. Seasonal prediction of Indian summer-monsoon rainfall in NCEP CFSv2: Forecast and predictability error. Clim. Dyn. 46, 2305–2326. http://dx.doi.org/10.1007/s00382-015-2703-1.

Ponsoni, L., Aguiar-Gonzalez, B., Ridderinkhof, H., Maas, L.R.M., 2016. The east madagascar current: Volume transport and variability based on long-term observations. J. Phys. Oceanogr. 46 (4), 1045–1065. http://dx.doi.org/10.1175/JPO-D-15-0154.1.

Prasanna, V., 2015. Regional climate change scenarios over South Asia in the CMIP5 coupled climate model simulations. Meteorog. Atmos. Phys. 127, 561–578. http://dx.doi.org/10.1007/s00703-015-0379-z.

Praveen Kumar, B., Vialard, J., Lengaigne, M., Murty, V.S.N., McPhaden, M.J., Cronin, M.F., Pinsard, F., Gopala Reddy, K., 2013. Tropflux wind stresses over the tropical oceans: evaluation and comparison with other products. Clim. Dyn. 40, 2049–2071. http://dx.doi.org/10.1007/s00382-012-1455-4.

Premkumar, K., Ravichandran, M., Kalsi, S.R., Sengupta, D., Gadgil, S., 2000. First results from a new observational system over the Indian seas. Curr. Sci. 78, 323–331.

Qiu, B., Chen, S., Hacker, P., 2004. Synoptic-scale air–sea flux forcing in the western North Pacific: Observations and their impact on SST and the mixed layer. J. Phys. Oceanogr. 34, 2148–2159.

Qu, T., Meyers, G., Godfrey, J.S., Hu, D.X., 1994. Ocean dynamics in the region between Australia and Indonesia and its influence on the variation of sea surface temperature in a global general circulation model. J. Geophys. Res. 99 (18), 433–18, 445.

Rahaman, H., Ravichandran, M., 2013. Evaluation of near-surface air temperature and specific humidity from hybrid global products and their impact on latent heat flux in the North Indian Ocean. J. Geophys. Res. Oceans 118, 1034–1047. http://dx.doi.org/10.1002/jgrc.20085.

Rahaman, H., Ravichandran, M., Sengupta, D., Harrison, M.J., Griffies, S.M., 2014. Development of a regional model for the north Indian Ocean. Ocean Model. 75, 1–19.

Rajeevan, M., Pai, D.S., Kumar, R.A., Lal, B., 2007. New statistical models for long-range forecasting of southwest monsoon rainfall over India. Clim. Dyn. http://dx.doi.org/10.1007/s00382-006-019706.

Rajeevan, M., Unnikrishnan, C.K., Preethi, B., 2012. Evaluation of the ENSEMBLES multi-model seasonal forecasts of Indian summer monsoon variability. Clim. Dyn. 38 (11–12), 2257–2274.

Rao, R.R., 2015. Observed variability of near-surface salinity field on seasonal and interannual time scales and its impact on the evolution of sea surface temperature of the tropical Indian Ocean. Int. J. Ocean Clim. Syst. 6, 87–111.

Rao, R.R., Jitendra, V., GirishKumar, M.S., Ravichandran, M., Ramakrishna, S.S.V.S., 2015. Interannual variability of the Arabian Sea Warm Pool: observations and governing mechanisms. Clim. Dyn. 44, 2119–2136. http://dx.doi.org/10.1007/s00382-014-2243-0.

Rao, R.R., Molinari, R.L., Festa, J.F., 1991. Surface Meteorologicaland Subsurface Oceanographic Atlas of the Tropical Indian Ocean, NOAA Tech. Memor. ERL-AOML-69, p. 59.

Rao, R.R., Ramakrishna, S.S.V.S., 2017. Observed seasonal and interannual variability of the near-surface thermal structure of the Arabian Sea Warm Pool. Dyn. Atmos. Oceans 78, 121–136. http://dx.doi.org/10.1016/j.dynatmoce.2017.03.001.

Rao, R.R., Sanil Kumar, K.V., 1991. Evolution of salinity field in the upper layers of the east central Arabian Sea and northern Bay of Bengal during summer monsoon experiments. Proc. Indian Acad. Sci. 100 (1991), 69–78.

Rao, R.R., Sivakumar, R., 1999. On the possible mechanisms of the evolution of a mini-warm pool during the pre-summer monsoon season and theonset vortex in the southeastern Arabian Sea. Q. J. R. Meteorol. Soc. 125, 787–809.

Rao, R.R., Sivakumar, R., 2000. Seasonal variability of the heat budget of the mixed layer and the near-surface layer thermal structure of the tropical Indian Oceanfrom a new global ocean temperature climatology. J. Geophys. Res. 105, 995–1015.

Rao, R.R., Sivakumar, R., 2003. Seasonal variability of sea surface salinity and salt budget of the mixed layer of the north Indian Ocean. J. Geophys. Res. 108 (C1), 3009. http://dx.doi.org/10.1029/2001JC000907.

Reppin, J., Schott, F., Fischer, J., 1999. Equatorial currents and transports in the upper central Indian Ocean: Annual cycle and interannual variability. J. Geophys. Res. 104 (7), 15, 495–15, 514.

Reverdin, G., 1985. Convergence in the equatorial surface jets of the Indian Ocean. J. Geophys. Res. (ISSN: 0148-0227) 90, http://dx.doi.org/10.1029/JC080i014p11741.

Reynolds, R.W., Rayner, N.A., Smith, T.M., Stokes, D.C., Wang, W., 2002. An improved in situ and satellite SST analysis for climate. J. Clim. 15, 1609–1625.

Ridderinkhof, W., Le Bars, D., von der Heydt, A.S., de Ruijter, W.P.M., 2013. Dipoles of the south east madagascar current. Geophys. Res. Lett. 40, 558–562. http://dx.doi.org/10.1002/grl.50157.

Rochford, D.J., 1964. Salinity maxima in the upper 1000 metres of the North Indian Ocean. Aust. J. Mar. Freshw. Res. 15, 1–24.

Roxy, M., Tanimoto, Y., Preethi, B., Terray, P., Krishnan, R., 2012. Intraseasonal SST-precipitation relationship and its spatial variability over the tropical summer monsoon region. Clim. Dyn. 41 (1), 45–61.

Saha, S.K., Hazra, A., Pokhrel, S., Chaudhari, H.S., Sujith, K., Rai, A., Rahaman, H., Goswami, B.N., 2019. Unraveling the mystery of Indian summer monsoon prediction: Improved estimate of predictability limit. J. Geophys. Res. Atmos. 124, 1962–1974. http://dx.doi.org/10.1029/2018JD030082.

Sahai, A.K., Mandke, S.K., Shinde, M.A., Chattopadhyay, R., Joseph, S., Goswami, B.N., 2007. Experimental seasonal forecast of Indian summer monsoon 2007: statistical and dynamical models. Res. Rep. RR 120.

Saji, N.H., Goswami, B.N., Vinayachandran, P.N., Yamagata, T., 1999. A dipole mode in the tropical Indian Ocean. Nature 401, 360–363.

Saji, N.H., Xie, S.P., Yamagata, T., 2006. Tropical Indian Ocean variability in the IPCC twentieth-century climate simulations. J. Clim. 19, 4397–4417.

Saji, N.H., Yamagata, T., 2003. Possible impacts of Indian Ocean dipole mode events on global climate. Clim. Res. 25 (2), 151–169.

Sanchez-Franks, A., Kent, E.C., Matthews, A.J., Webber, B.G., Peatman, S.C., Vinayachandran, P.N., 2018. Intraseasonal variability of air–sea fluxes over the Bay of Bengal during the southwest monsoon. J. Clim. 31 (17), 7087–7109.

Sandeep, S., Ajayamohan, R.S., 2014. Origin of cold bias over the Arabian Sea in Climate Models. Sci. Rep. 4, 6403. http://dx.doi.org/10.1038/srep06403.

Sastry, J.S., Rao, D.P., Murty, V.S.N., Sarma, Y.V.B., Suryanarayana, A., Babu, M.T., 1985. Watermass structure in the Bay of Bengal. Mahasagar 18, 153–162.

Sayantani, O., Gnanaseelan, C., Chowdary, J.S., Parekh, A., Rahul, S., 2016. Arabian Sea SST evolution during spring to summer transition period and the associated processes in coupled climate models: Arabian Sea SST biases in coupled climate models. Int. J. Clim. 36, 2541–2554. http://dx.doi.org/10.1002/joc.4511.

Schott, F., Dengler, M., Schoenefeldt, R., 2002a. The shallow overturning circulation of the Indian Ocean. Prog. Oceanogr. 53, 57–103.

Schott, F., Dengler, M., Schoenefeldt, R., 2002b. Erratum to: The shallow overturning circulation of the Indian Ocean. Prog. Oceanogr. 55, 373–384. http://dx.doi.org/10.1016/S0079-6611(02)00117-9.

Schott, F.A., McCreary, J.P., 2001. The monsoon circulation of the Indian Ocean. Prog. Oceanogr. 51, 1–123.

Schott, F.A., McCreary, J.P., Johnson, G.C., 2004. Shallow overturning circulations of the tropical-subtropical oceans. In: Wang, C., Xie, S-.P., Carton, J.A. (Eds.), Earth's Climate: The Ocean-Atmosphere Interaction. In: Geophys. Monogr. Ser., vol. 147, AGU, Washington, D. C, pp. 261–304.

Schott, F., Swallow, J.C., Fieux, M., 1990. The Somali Current at the equator: Annual cycle and transports. Deep Sea Res. 37A, 1825–1848.

Schott, F.A., Xie, S.-P., McCreary, J.P., 2009. Indian Ocean circulation and climate variability. Rev. Geophys. 47, http://dx.doi.org/10.1029/2007RG000245.

Seidel, H.F., Giese, B.S., 1999. Equatorial currents in the Pacific Ocean 1992–1997. J. Geophys. Res. 104 (C4), 7849–7863. http://dx.doi.org/10.1029/1999JC900036.

Senan, R., Anitha, D.S., Sengupta, D., 2001. Validation of SST and WS from TRMM using north Indian Ocean moored buoy observations. In: CAOS Rep. 2001AS1. Cent. for Atmos. Sci. Indian Inst. of Sci., Bangalore, India.

Sengupta, D., Raj, G.N.B., Shenoi, S.S.C., 2006. Surface freshwater from the Bay of Bengal runoff and Indonesian through flow in the tropical Indian Ocean. Geophys. Res. Lett. 33 (L22609), 2006G. http://dx.doi.org/10.1029/L027573.

Shankar, D., Shenoi, S.S.C., Nayak, R.K., Vinayachandran, P.N., Nampoothiri, G.S., Almeida, A.M., Selvan, G., RameshKumar, M.R., Sundar, D., Sreejith, O.P., 2005. Hydrography of the eastern Arabian Sea during summer monsoon 2002. J. Earth. Syst. Sci. 114, 475–491. http://dx.doi.org/10.1007/BF02702024.

Shankar, D., Vinayachandran, P.N., Unnikrishnan, A.S., 2002. The monsoon currents in the north Indian Ocean. Prog. Oceanogr. 52, 63–120.

Sharma, R., Agarwal, N., Basu, S., Agarwal, V.K., 2007. Impact of satellite-derived forcings on numerical ocean model simulations and study of sea surface salinity variations in the Indian Ocean. J. Clim. 20, 871–890.

Sharma, R., Agarwal, N., Momin, I.M., Basu, S., Agarwal, V.K., 2010. Simulated sea surface salinity variability in the tropical Indian Ocean. J. Clim. 23, 6542–6554. http://dx.doi.org/10.1175/2010JCLI3721.

Shenoi, S.S.C., Shankar, D., Michael, G.S., Kurian, J., Varma, K.K., Ramesh Kumar, M.R., Almeida, A.M., Unnikrishnan, A.S., Fernandes, W., Barreto, N., Gnanaseelan, C., Mathew, R., Praju, K.V., Mahale, V., 2005. Hydrography and water masses in the southeastern Arabian Sea during March–2003. J. Earth. Syst. Sci. 114 (5), 475–491.

Shenoi, S.S.C., Shankar, D., Shetye, S., 1999. On the seas surface temperature high in the Lakshadweep Sea before the onset of the summer monsoon. J. Geophys. Res. 104 (C7), 15703–15712.

Shenoi, S.S.C., Shankar, D., Shetye, S.R., 2002. Differences in heat budgets of the near-surface Arabian Sea and Bay of Bengal: implications for the summer monsoon. J. Geophys. Res. 107 (C6), 3052. http://dx.doi.org/10.1029/2000JC000679.

Shenoi, S.S.C., Shankar, D., Shetye, S.R., 2004. Remote forcing annihilates barrier layer in southeastern Arabian Sea. Geophys. Res. Lett. 31.

Shenoi, S.S.C., Shetye, S.R., Gouveia, A.D., Michael, G.S., 1993. Salinity extrema in the Arabian Sea. In: Ittekkot, V., Nair, R.R. (Eds.), Monsoon Biogeochemistry. Mitteilungen des Geologisch-Paläontologischen Instituts der Universität Hamburg, University of Hamburg, Germany, pp. 37–49.

Shetye, S.R., Gouveia, A.D., Shankar, D., Shenoi, S.S.C., Vinayachandran, P.N., Sundar, D., Michael, G.S., Nampoothiri, G., 1996. Hydrography and circulation in the western Bay of Bengal during the northeast monsoon. J. Geophys. Res. 101 (C6), 14, 011–14, 025.

Shetye, S.R., Gouveia, A.D., Shenoi, S.S.C., 1994. Circulation and water masses of the Arabian Sea. Proc. Indian Acad. Sci. (Earth Planet Sci) 103, 107–123. http://dx.doi.org/10.1007/BF02839532.

Shikha, S., Valsala, V., 2018. Role of subsurface ocean bias in coupled models in simulated interannual variability: A case study for Indian Ocean. Dyn. Atmos. Ocean http://dx.doi.org/10.1016/j.dynatmoce.2018.10.001.

Siedler, G., Rouault, M., Biastoch, A., Backeberg, B., Reason, C., Lutjeharms, J., 2009. Modes of the southern extension of the East Madagascar Current. J. Geophys. Res. 114, http://dx.doi.org/10.1029/2008JC004921.

Sitz, L.E., Sante, F., Farneti, R., Fuentes-Franco, R., Coppola, E., Mariotti, L., Reale, M., et al., 2017. Description and evaluation of the earth system regional climate model (RegCM–ES). J. Adv. Modelling Earth Syst. http://dx.doi.org/10.1002/2017MS000933.

Sperber, K.R., Palmer, T.N., 1996. Interannual tropical rainfall variability in general circulation model simulations associated with the atmospheric model intercomparison project. J. Clim. 9, 2727–2750.

Sprintall, J., Tomczak, M., 1992. Evidence of the barrier layer in the surface layer of the tropics. J. Geophys. Res. 97, 7305–7316.

Srinivasu, U., Ravichandran, M., Han, W., Sivareddy, S., Rahaman, H., Nayak, S., 2017. Causes for decadal reversal of North Indian Ocean sea level in recent two decades. Clim. Dyn. http://dx.doi.org/10.1007/s00382-017-3551-y.

Stocker, T.F., Qin, D., Plattner, G.-K., Tignor, M., Allen, S.K., Boschung, J., Nauels, A., Xia, Y., Bex, V., Midgley, P.M. (Eds.), 2013. IPCC, Climate Change 2013: The Physical Science Basis. Contribution of Working Group I to the Fifth Assessment Report of the Intergovernmental Panel on Climate Change. Cambridge University Press, Cambridge, United Kingdom and New York, NY, USA, p. 1535.

Stull, R., 2011. Meteorology for Scientists and Engineers, third ed..

Sujith, K., Saha, S.K., Rai, A., Pokhrel, S., Chaudhari, H.S., Hazra, A., Murtugudde, R., Goswami, B.N., 2019. Effects of a multilayer snow scheme on the global teleconnections of the Indian summer monsoon. Q. J. R. Meteorol. Soc. 145, 1102–1117. http://dx.doi.org/10.1002/qj.3480.

Swain, D., Rahman, S.H., Ravichandran, M., 2009. Comparison of NCEP turbulent heat fluxes with in-situ observations over the south-eastern Arabian Sea. Meteorol. Atmos. Phys 104, 163–175. http://dx.doi.org/10.1007/s00703-009-0023-x.

Swallow, J.C., 1964. Equatorial undercurrent in western Indian Ocean. Nature 20, 436–437.

Swallow, J.C., 1967. The equatorial undercurrent in the western Indian Ocean in 1964. In: Studies in _Tropical Oceanography, (5). Univ. of Miami Press, Coral Gables, Fla. 1967, pp. 15–36.

Swapna, P., Jyoti, J., Krishnan, R., Narayan Setti, S., Griffies, S.M., 2017. Multi-decadal weakening of Indian summer monsoon circulation induces an increasing northern Indian Ocean sea level. Geophys. Res. Lett. http://dx.doi.org/10.1002/2017GL074706.

Swapna, P., Krishnan, R., Wallace, J., 2014. Indian ocean and monsoon coupled interactions in a 2795 warming environment. Clim. Dyn. 42, 2439–2454.

Tao, W., Huang, G., Hu, K., Gong, H., Wen, G., Liu, L., 2015. A study of biases in simulation of the Indian Ocean basin mode and its capacitor effect in CMIP3/CMIP5 models. Clim. Dyn. http://dx.doi.org/10.1007/s00382-015-2579-0.

Taylor, K.E., Stouffer, R.J., Meehl, G.A., 2012. An overview of CMIP5 and the experiment design. Bull. Am. Meteorol. Soc. 93 (4), 485–498. http://dx.doi.org/10.1175/BAMS-D-11-00094.1.

Thadathil, P., Muraleedharan, P.M., Rao, R.R., Somayajulu, Y.K., Reddy, G.V., Revichandran, C., 2007. Observed seasonal variability of barrier layer in the Bay of Bengal. J. Geophy. Res. 112 (C2), C02009.

Thangaprakash, V.P., Girishkumar, M.S., Suprit, K., Sureshkumar, N., Dipanjan, C., Dinesh, K., Ashok, K., Shivaprasad, S., Ravichandran, M., Thomas Farrar, J., Sundar, N., Weller, R.A., 2015. What controls seasonal evolution of SST in the Bay of Bengal? Mixed layer heat budget analysis using moored buoy observations along 90°E. Oceanography 29 (2), 202–213. http://dx.doi.org/10.5670/oceanog.2016.52.

Tozuka, T., Cronin, M.F., Tomita, H., 2017. Surface frontogenesis by surface heat fluxes in the upstream Kuroshio Extension region. Sci. Rep. 7, 10258.

Tseng, Y.-H., Lin, H., Chen, H.-C., Thompson, K., Bentsen, M., Boning, C., Bozec, A., Cassou, C., Chassignet, E., Chow, C.H., Danabasoglu, G., Danilov, S., Farneti, R., Fujii, Y., Griffies, S., Ilicak, M., Jung, T., Masina, S., Navarra, A., Patara, L., Samuels, B., Scheinert, M., Sidorenko, D., Sui, C.-H., Tsujino, H., Valcke, S., Voldoire, A., Wang, Q., 2017. North and equatorial pacific ocean circulation in the CORE-II hindcast simulations. Ocean Model. 104 (2016), 143–170.

Tsujino, H., Shogo, U., Nakano, H., Small, R.J., Kim, W.M., Yeager, S.G., Danabasoglu, G., Suzuki, T., Bamber, J.L., Bentsen, M., Böning, C.W., Bozec, A., Chassignet, E.P., Curchitser, E., Dias, F.B., Durack, P.J., Griffies, S.M., Harada, Y., Ilicak, M., Josey, S.A., Kobayashi, C., Kobayashi, S., Komuro, Y., Large, W.G., Sommer, J.L., Marsland, .S.J., Masina, S., Scheinert, M., Tomita, H., Valdivieso, M., Yamazaki, D., 2018. JRA-55 based surface dataset for driving ocean–sea-ice models (JRA55-do). Ocean Model. 130, 79–139. http://dx.doi.org/10.1016/j.ocemod.2018.07.002.

Varadachari, V.V.R., Murty, C.S., Reddy, C.V.G., 1968. Salinity maxima associated with some sub-surface water masses in the upper layers of the bay of bengal. Bull. Natl. Inst. Sci. India 38, 338–343.

Venugopal, T., Rahaman, Hasibur, 2019. Evaluation of hybrid and satellite derived surface downwelling shortwave and long wave radiation over tropical global oceans. SN Appl. Sci. 1, 1171. http://dx.doi.org/10.1007/s42452-019-1172-2.

Vialard, J., Duvel, J.-P., Mcphaden, M.J., Bouruet-Aubertot, P., Ward, B., Key, E., Bourras, D., Weller, R.A., Minnett, P., Weill, A., et al., 2009. Cirene: air-sea Interactions in the Seychelles-Chagos thermocline ridge region. Bull. Am. Meteorol. Soc. 90, 45–61.

Vialard, J., Jayakumar, A., Gnanaseelan, C., Lengaigne, M., Sengupta, D., Goswami, B.N., 2012. Processes of 30–90 days sea surface temperature variability in the northern Indian Ocean during boreal summer. Clim. Dyn. 38 (9–10), 1901–1916.

Vinayachandran, P.N., Masumoto, Y., Mikawa, T., Yamagata, T., 1999. Intrusion of the southwest monsoon current into the Bay of Bengal. J. Geophys. Res. 104 (C5), 11077–11085. http://dx.doi.org/10.1029/1999JC900035.

Vinayachandran, P.N., Murty, V.S.N., Ramesh Babu, V., 2002. Observations of barrier layer formation in the Bay of Bengal during summer monsoon: barrier layer in the bay of bengal. J. Geophys. Res. Oceans 107, http://dx.doi.org/10.1029/2001JC000831, SRF 19-1-SRF 19-9.

Vinayachandran, P.N., Nanjundiah, R.S., 2009. Indian Ocean sea surface salinity variations in a coupled model. Clim. Dyn. 33, 245–263. http://dx.doi.org/10.1007/s00382-008-0511-6.

Vinayachandran, P.N., Shetye, S.R., 1991. The warm pool in the Indian Ocean. Proc. Indian Acad. Sci. (Earth Planet. Sci.) 100 (2), 165–175.

Vipin, P., Sarkar, K., Aparna, S.G., Shankar, D., Sarma, V.V.S.S., Gracias, D.G., Krishna, M.S., Srikanth, G., Mandal, R., Rama Rao, E.P., Srinivasa Rao, N., 2015. Evolution and sub-surface characteristics of a sea-surface temperature filament and front in the northeastern Arabian Sea during November–2012. J. Mar. Syst. 150, 1–11. http://dx.doi.org/10.1016/j.jmarsys.2015.05.003.

Wacongne, S., Pacanowski, R.C., 1996. Seasonal heat transport in aprimitive equation model of the tropical Indian Ocean. J. Phys. Oceanogr. 26, 2666–2699.

Waite, A.M., Thompson, P.A., Pesant, S., Feng, M., Beckley, L.E., Domingues, C.M., Gaughan, D., Hanson, C.E., Holl, C.M., Koslow, T., Mueleners, M., Montoya, J.P., Moore, T., Muhling, B.A., Paterson, H., Rennie, S., Strzelecki, J., Twomey, L., 2007. The leeuwin current and its eddies: An introductory overview. Deep-Sea Res. II 54, 789–796. http://dx.doi.org/10.1016/j.dsr2.2006.12.008.

Wang, Y., McPhaden, M.J., 2017. Seasonal cycle of cross-equatorial flow in the central Indian Ocean. J. Geophys. Res. Oceans 122, 3817–3827. http://dx.doi.org/10.1002/2016JC012537.

Wang, H., Murtugudde, R., Kumar, A., 2016. Evolution of Indian Ocean dipole and its forcing mechanisms in the absence of ENSO. Clim. Dyn. 47 (7), 2481–2500.

Wang, X., Wang, C., 2014. Different impacts of various El Niño events on the Indian Ocean dipole. Clim. Dyn. 42, 991–1005. http://dx.doi.org/10.1007/s00382-013-1711-2.

Warren, B.A., 1981. Transindian hydrographic section at Lat. 18S: Property distributions and circulation in the South Indian Ocean. Deep Sea Res. Part A 28, 759–788.

Webster, P.J., Magaña, V.O., Palmer, T.N., Shukla, J., Tomas, R.A., Yanai, M., Yasunari, T., 1998. Monsoons: Processes, predictability, and the prospects for prediction. J. Geophys. Res. Oceans 1978–2012 103, 14451–14510. http://dx.doi.org/10.1029/97JC02719.

Webster, P.J., Moore, Andrew M., Johannes, P., Loschnigg, D.N., Robert, R.L., 1999. Coupling strength of charge carriers to spin fluctuations in high-temperature superconductors. Nature 401, 354–356.

Weller, R.A., Anderson, S.P., 1996. Surface meteorology and air-sea fluxes in the western equatorial Pacific warm pool during the TOGA Coupled Ocean-Atmosphere Rsponse Experiment. J. Clim. 9, 1959–1990.

Wyrtki, K., 1973. An equatorial jet in the Indian Ocean. Science 181, 262–264.

Xie, S.-P., Annamalai, H., Schott, F.A., McCreary, J.P., 2002. Structure andmechanisms of South Indian Ocean climate variability. J. Clim. 15, 864–878.

Xie, S.P., Hu, K., Hafner, J., Tokinaga, H., Du, Y., Huang, G., Sampe, T., 2009. Indian Ocean capacitor effect on Indo–western Pacific Climate during the summer following El Niño. J. Clim 22, 730–747.

Yamagami, Y., Tozuka, T., 2015. Interannual variability of South Equatorial Current bifurcation and western boundary currents along the Madagascar coast. J. Geophys. Res. Oceans 120, 8551–8570. http://dx.doi.org/10.1002/2015JC011069.

Yang, J., Liu, Q., Xie, S.-P., Liu, Z., Wu, L., 2007. Impact of the Indian Ocean SST basin mode on the Asian summer monsoon. Geophys. Res. Lett. 34, http://dx.doi.org/10.1029/2006GL028571.

Yokoi, T., Tozuka, T., Yamagata, T., 2008. Seasonal variation of the Seychelles Dome. J. Clim. 21, 3740–3754.

Yokoi, T., Tozuka, T., Yamagata, T., 2009. Seasonal variations of the seychelles dome simulated in the CMIP3 models. J. Phys. Oceanogr. 39, 449–457. http://dx.doi.org/10.1175/2008JPO3914.1.

Yokoi, T., Tozuka, T., Yamagata, T., 2012. Seasonal and interannual variations of the SST above the Seychelles Dome. J. Clim. 25, 800–814.

Yu, L., 2011. A global relationship between the ocean water cycle and near-surface salinity. J. Geophys. Res. 116, http://dx.doi.org/10.1029/2010JC006937.

Yu, L., Jin, X., Weller, R.A., 2007. Annual, seasonal, and interannual variability of air–sea heat fluxes in the Indian Ocean. J. Clim. 20, 3190–3209, Special issue on the Climate Variability and Predictability of the Indian Ocean.

Zhang, K.Q., Marotzke, J., 1999. The importance of open-boundary estimation for an Indian Ocean GCM-data synthesis. J. Mar. Res. 57, 305–334.